Aggregation behaviour of pyrene-based Luminescent materials, from molecular design and optical properties to application

Received 00th January 20xx,
Accepted 00th January 20xx

DOI: 10.1039/x0xx00000x

Xing Feng*[a], Xiaohui Wang[a], Carl Redshaw*[b] and Ben Zhong Tang*[c]

Molecular aggregates are self-assembled from multiple molecules via weak intermolecular interactions, and new chemical and physical properties can emerge compared to their molecular constituents. With the development of aggregate science, much research has focused on the study of the luminescence behaviour of aggregates rather than single molecules. Pyrene as a classical fluorophore has attracted great attention due to its outstanding luminescence properties and wide potential applications. Pyrene prefers to emit monomer emission in dilute solution, but tends to form a dimer via π-π stacking in the aggregation state, resulting in red-shifted emission with quenched fluorescence and quantum yield. Over the past two decades, much effort has been devoted to developing novel pyrene-based fluorescent molecules and determining the luminescence mechanism for potential applications. Since the concept of "aggregation-induced emission (AIE)" was proposed by Tang *et al*. in 2001, the aggregated luminescence behaviour of pyrene-based materials has been extensively investigated. New pyrene-based emitters with AIE characteristics have been designed and synthesized for investigating not only the relationships between molecular structure and properties, and advanced applications, but also to examine the effect of the aggregate morphology on their optical and electronic properties. Indeed, new aggregated pyrene-based molecules have emerged with unique properties, such as circularly polarized luminescence, excellent fluorescence, and phosphorescence and electroluminescence, ultra-high mobility, etc, which are beneficial for the realization of cutting-edge technological applications. Reviews published to-date have mainly concentrated on summarizing the molecular design and multi-functional applications of pyrene-based fluorophores, whereas the aggregation behaviour of pyrene-based luminescence materials has received very little attention. The majority of the multi-functional applications of pyrene molecules are not only closely related to their molecular structures, but also to the packing model they adopt in the aggregated state. In this review, we will summarize the intriguing optoelectronic properties of pyrene-based luminescence materials boosted by aggregation behaviour, and systematically establish the relationship between molecular structure, aggregation states, and optoelectronic properties. This review will provide a new perspective for understanding the luminescence and electronic transition mechanism of pyrene-based materials and will facilitate further development of pyrene chemistry.

Introduction

Luminescence, "a quality in something that produces light", defined by Oxford Advanced Learner's Dictionary, involves photoluminescence, electroluminescence, radioluminescence, chemiluminescence, and bioluminescence. Among them, fluorescence and phosphorescence belong to photoluminescence, which was first investigated by the French physicist Alexandre E. Becquerel in 1857. [1] As the development of fluorescence technologies advanced, a great number of luminescent materials were intensively explored for various potential applications, such as fluorescent probes, boilable, organic light-emitting diodes (OLED), diagnosis and therapy, [2] anti-counterfeiting, [3] and so on. Moreover, luminescence-related research studies have been awarded Nobel prizes in chemistry or physics at least three times for the discovery and development of the green fluorescent protein (2008), super-resolved fluorescence microscopy (2014), and for the invention of efficient blue light-emitting diodes (2014), respectively. Notably, the United Nations (UN) declared 2015 as the "International Year of Light and Light-Based Technologies".

Luminescence is a process of releasing energy. According to the Jablonski diagram shown in Scheme 1, the fluorophore molecules absorb photons (light energy), and the electrons transfer from the ground state (S_0) to the lowest singlet excited state (S_1) or higher excited state (S_n, n≥2), depending on the excited wavelength. Then, the electrons relax to the S_1 state via a vibrational relaxation (VR) or internal conversion (IC) process following Kasha's rule. [4] Generally, the excited electrons in the S_1 state can release energy to S_0 through four deactivation pathways. (1) The electrons undergo an $S_1 \rightarrow S_0$

---

[a] *Guangdong Provincial Key Laboratory of Information Photonics Technology, School of Material and Energy, Guangdong University of Technology, Guangzhou, 510006, P. R. China; Email: hyxhn@sina.com.*
[b] *Chemistry, School of Natural Sciences, University of Hull, Hull, Yorkshire HU6 7RX, UK; Email: c.redshaw@hull.ac.uk*
[c] *School of Science and Engineering, Shenzhen Institute of Aggregate Science and Technology, The Chinese University of Hong Kong, Shenzhen, Guangdong 518172, China.; Email: tangbenz@cuhk.edu.cn*

transition via a radiative decay pathway to produce fluorescence; (2) Through a non-radiative decay pathway to generate heat; (3) If the energy splitting (ΔE_{ST}) between S_1 and T_1 is sufficiently small or the spin orbit coupling (SOC) effect is strong, [5] the electrons also may transfer from S_1 to the lowest triplet excited state (T_1) via an intersystem crossing (ISC) process. Subsequently, the electrons return to the S_0 state through a radiative decay pathway to phosphorescence; or (4) non-radiative decay pathway and produce reactive oxygen species (ROS). [6, 7 8 9]

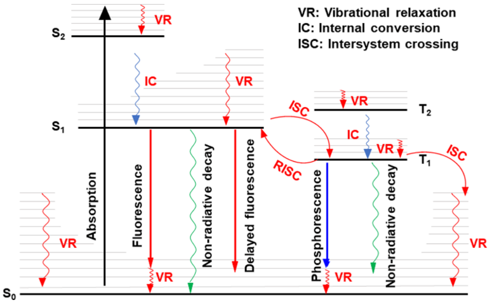

Scheme 1. Jablonski diagram illustrating the fundamental radiative and non-radiative processes of luminescent molecules.

In the electroluminescence process, only 25% of excitons in the singlet state are generated photons, and 75% of excitons in the triplet state are lost, according to the spin-statistics rule. [10] Thus, the maximum internal quantum efficiency (IQE) for traditional fluorescence OLEDs is 25%. To realize theoretical 100% IQE, the 75% excitons in the triplet state could be utilized and up-converted to the S_1 state through reverse intersystem crossing (RISC). [11 12] However, because the transition between T_1 and S_1 is forbidden, RISC is extremely difficult under ambient conditions. Thus, there is a possible strategy to make the RISC process more facile using organic thermally activated delayed fluorescence (TADF) materials[13] via lowering the ΔE_{ST} between the S_1 and T_1 states. Theoretically, the TADF materials can achieve an IQE of up to 100% and undergo a $T_1 \rightarrow S_1 \rightarrow S_0$ process transition. [14] Also, heavy metals can be used for enhancing the RISC rate via increased spin-orbit coupling, to maximize the utilization of excitons in the triplet state. [15] Furthermore, Ma *et al*. proposed the "hot exciton mechanism", [16-18] where unlike the conditional TADF mechanism, the exciton transition occurred via an up-conversion from the higher-lying T_m ($m > 1$) state to the S_n ($n \geq 1$) state via a fast RISC, and then returned to the S_0 state. All strategies provide a possibility for the utilization of the triplet exciton and to improve the 100% IQE.

Aggregation-caused quenching (ACQ) *vs* aggregation-induced emission (AIE)

It is noteworthy that luminescent materials with conjugated units can emit strong emissions in dilute solvent, but tend to form molecular aggregation via strong inter-/intramolecular interactions (such as π-π stacking) at high concentration, resulting in fluorescence quenching with red-shifted emission, namely aggregation-caused quenching (ACQ). Generally speaking, the ACQ effect is the essential property of most luminescent materials, such as perylene,[19] consequently limiting their high-technological application. By contrast, in 2001, Tang with co-workers observed abnormal photophysical properties in some fluorescence dyes, such as tetraphenylethylene (TPE), which exhibited weak emission in pure THF solution, yet exhibited bright emission in the aggregate state. This optical phenomenon has been defined as aggregation-induced emission (AIE) (Figure 1).[20] The restriction of intramolecular motion (RIM) has been proposed for understanding the AIE behaviour and constructing AIE lumingeous (AIEgens) for various applications (Figure 1B).[19 21] Aggregated molecules have emerged with new chemical and optical properties compared to those observed in single molecules, which can be controlled by molecular structure, molecular packing and molecular conformations.[22]

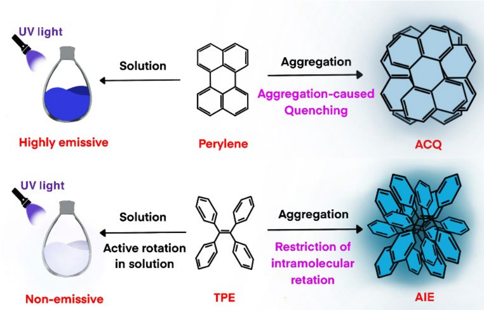

Fig. 1 Schematic illustration of the emission behaviour of perylene and TPE, and the mechanisms of the AIE phenomenon.

The chemical and photophysical properties of pyrene

Pyrene is an important member of the polycyclic aromatic hydrocarbons (PAHs) containing four fused benzene rings (Figure 2A).[23] Since pyrene was first distilled from coal tar in 1837,[24] the unique molecular structure and optical properties of pyrene have attracted intense interest both for fundamental research and in the industrial community. As an excellent fluorophore, pyrene exhibits advantageous photophysical properties, such as deep blue emission ($\lambda_{max\ em} = 372$ nm), long fluorescence lifetime of the pyrene monomer ($\iota = 354$ ns), and high fluorescence quantum yield ($\Phi_f = 0.64$) in non-polar toluene.[25] In fact, the fluorescence spectra of pyrene in the monomer state are sensitive to changes in the microenvironment. The solvent-dependence of vibronic band intensity in pyrene monomer fluorescence has been thoroughly investigated by Nakajima and Thomas some 50 years ago.[26,27, 28] For example, the monomer pyrene exhibits five predominant emission peaks with varying relative peak intensities of the various bands (I-V number) in different solutions (Figure 2B-E). The experimental results indicated that the solvent polarity exerts a more positive influence on the various vibronic bands than on the bulk solvent dielectric constant. [29] Thus, this distinct solvent-dependence of vibronic band intensity for the pyrene monomer fluorescence could be a sensitive fluorescence sensor for probing bio-aggregates, micellar, [29-31] the polarity of the organic matter[32] and dendritic interior,[33] etc.

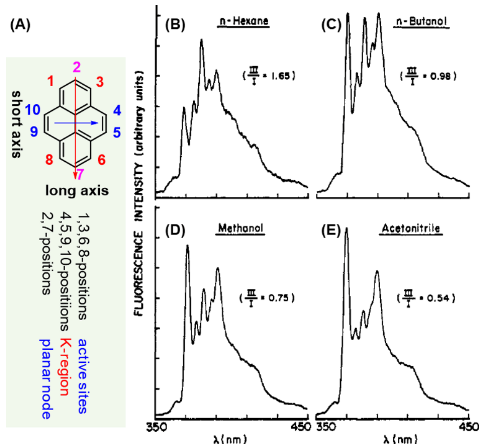

Fig. 2 (A) Molecular structure of pyrene, Solvent-dependence of vibronic band intensity in pyrene monomer fluorescence; (B) in *n*-hexane, (C) in *n*-butanol, (D) methanol, and (E) in acetonitrile. [pyrene]: 2 μ M, λ_{ex} = 310 nm. III/I corresponds to the relative emission intensity of third peak III and first peak I. Reproduced from Copyright (1977) American Chemical Society.[29]

Pyrene has a rhombus-shaped molecular structure with D_{2h} symmetry, and the TD-DFT calculated (B3LYP/6-31G(d, p)) HOMO and LUMO energies of pyrene are -5.62233 eV and -1.82558 eV, respectively, and the thermotical energy gap is 3.79675, which is in agreement with the experimental value (3.721 eV).[34] The unique molecular symmetry endows the pyrene with a highly electronegativity and an abnormal electronic transition unlike traditional PHAs compounds. It is noteworthy that the $S_1 \leftarrow S_0$ transitions of pyrene is forbidden and the $S_2 \leftarrow S_0$ transitions is allowed.[35] For example, Marder *et al.* have described in detail the absorption behaviour of pyrene in solution by experimental and theoretical studies, and four absorption bands were observed in the range from 243-372 nm, which are assigned to $S_4 \leftarrow S_0$ (243 nm), $S_3 \leftarrow S_0$ (272 nm), $S_2 \leftarrow S_0$ (334 nm) and $S_1 \leftarrow S_0$ (372 nm) transitions, respectively (Figure 3A).[25] On the other hand, according to the TD-DFT calculations, the S_1 and S_0 energy levels of pyrene are close with a small energy gap (ΔE_{S2-S1} = 0.271 eV), resulting in complex absorption and emission line shapes. This process is not simply described by the Franck-condon principle.[36]

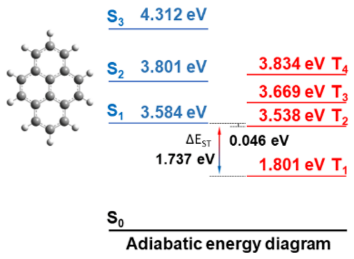

Scheme 2. Schematic representation of the energy level of pyrene at ground state and in the excited state (Gaussian 09 W (B3LYP/6-31G(d,p) basis set)).

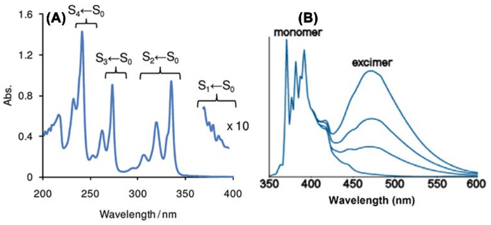

Fig. 3 (A) UV-vis spectra of pyrene in cyclohexane with transitions labelled, Reproduced from Copyright (2011) American Chemical Society.[25] (B) The emission spectra of pyrene as the concentration increasing from 6 mM to 0.09 M; Reproduced from Copyright (2012) Elsevier Ltd.[37]

Upon excitation, the pyrene exhibits typical bands emission in the range from 380 to 420 nm at 10^{-6} M, and when the concentration was increased to 10^{-4} M, the pyrene exhibited dual emission with a new emission peak at *ca*. 475 nm, Moreover, the intensity of the long-wavelength emission of pyrene could be enhanced as the concentration increased to 10^{-3} M. (Figure 3B).[37] The short-wavelength emission is originating from the monomer emission of pyrene, and the long-wavelength emission is contributing to the excimer emission. Thus, the pyrene can form the dimer when the concentration is up to 10^{-4} M.

The molecular packing of pyrene

As a typical planar molecule with an expanded π-conjugated system, the pyrene prefers to form a dimer. Förster *et al.* firstly observed the excimer emission of pyrene in 1955.[38] Generally, pyrene adopts four kinds of molecular pattern (face-to-face π-π stacking (Figure 4A and 4E), partial overlapped π-π stacking (Figure 4B and 4F), non-π-π stacking (Figure 4C and 4G) and C-H···π interactions (Figure 4D and 4H), respectively, via weak intermolecular interactions. In addition, single crystal X-ray diffraction analysis indicated that the pyrene easily formed a dimer by π-π stacked aggregates with an interplanar distance of 3.53 Å.[39] More importantly, upon excitation, the pair of pyrene molecules via π-π stacking interactions tend to move toward one another and towards complete overlap.[40] Such movement can change the unfavourable interactions with the neighbouring molecules in the aggregate state.

On the other hand, the pyrene-based dimer mainly adopted two possible close-packed models, namely *H*-aggregation and *J*-aggregation. *H*-aggregation can be defined as the pyrenes being parallel via face-to-face π-π stacking with a high degree of carbon atoms overlapping each other, where the dipole–dipole interactions repulsive each other, leading to enhanced energy. Thus, the *H*-aggregation can result in blue-shifted absorption spectra with a quenched fluorescence compared to its monomer, due to the lowest excited energy level being forbidden. Another close-packed model involves the pyrene molecules being arranged in an "in-line" fashion. In this case, the highest excited energy level is forbidden and the lowest excited energy level is allowed, thus, *J*-aggregation could cause both absorption and emission spectra to red-shift compared to its monomer. According to McRae's theory, the aligned angle (θ) between transitional moments and the centre-to-centre axis of the two chromophores is a significant parameter for determining the *H*- or *J*-aggregation, and an aligned angle value larger than 54.7° belongs to *H*-aggregation, and a value for the aligned angle (θ) of less than 54.7° belongs to *J*-aggregation (Figure 4E-4F). [41,42] It is clear that both *H*- and *J*- aggregation exhibit a distinguishing exciton-vibrational coupling. In *H*-aggregation, the ratio of the first two vibronic peak intensities in the absorption spectrum decreases with increasing excitonic coupling, while the ratio of the 0-0 to 0-1 emission intensity increases with increasing disorder and rising temperature, while the *J*-aggregation displays the opposite characteristics.[43,44,45,46]

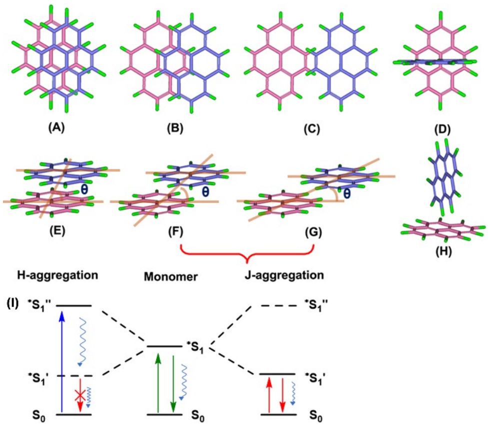

Fig. 4 The four packing models of pyrene via π-π stacking or C-H···π interactions. (A)-(D) top view, and (E)-(H) side view. (I) The excitation/de-excitation processes within *H*-aggregation (left side) and *J*-aggregation (right side).

Moreover, the electron transfer couplings of the dimer can be evaluated via the energy splitting method (Fig. 4I), [47] which is a reliable approach for understanding the excitation energy transfer between neighbouring molecules in the dimer system. The splitting energy (Δε) of the exciton state is defined as half of the energy gap of the excited S_1 and S_2 state of the dimer, and per the following equation:

$$\Delta\varepsilon = \frac{1}{2}\Delta\mathrm{E} = \frac{1}{2}\left(E_{s2} - E_{s1}\right)$$

The excited state energies of the S_1 and S_2 states can be performed by Time-Dependent Density Functional Theory (TD-DFT) calculations. If Δε > 0, the aggregation belongs to *H*-aggregation, and if Δε < 0, it belongs to *J*-aggregation. [48]

How to achieve a high-efficiency pyrene-based luminescent materials

As an excellent chromophore, the possible applications for pyrene or pyrene-based luminescent materials is in the aggregated state or the solid state include organic light emitting diodes (OLEDs) , [23] anti-counterfeiting, [49,50] and bioimaging. [51] However, the formation of π-π stacking of pyrene with low quantum yield is ubiquitous and limits the high-technological application of high-efficiency pyrene-based luminescent materials in many fields. The doping strategy has been explored in order to solve the molecular aggregation problem for pyrene but not thoroughly. [52, 53] Indeed, how to suppress the π-π stacking and improve the luminescence efficiency of pyrene-based emitters in the aggregated state remains a challenge. According to RIM, molecules with a twist conformation with rotators (such as phenyl ring, C=C bond, etc.) tend to possess AIE characteristics, such as the typical luminogens of TPE and its derivatives.[54] Indeed, TPE-decorated pyrene derivatives (**1**) illustrated bright emission in the aggregated state, [55] and many new non-typical pyrene-based emitters with AIE characteristics have been explored.[55] On the other hand, when α-cyanostyrenes decorate the pyrene, the compound **2** exhibits a weak emissive in solution, but enhanced emission intensity in the aggregated state, ascribe to increased π-π interactions. [56 57]

Moreover, excited-state intramolecular proton transfer (ESIPT) is also an important photophysical mechanism for improving the luminescence efficiency. [58] For ESIPT molecules an enol−keto tautomerism can exist, where the proton was transferred from a donating group (such as -OH, -NH_2) to an accepting group (such as -C=O, -N=O) upon phototautomerization within a subpico-second time scale. [59] Generally, most ESIPT fluorophores exhibit AIE character. [60] Thus, it is an alternative approach to construct pyrene-based ESIPT molecules to improve the emission in the aggregate state or in the solid state. For example, Qiao *et al.* reported an asymmetric bis-Schiff base pyrene-based emitter **3** with ESIPT and AIE characteristics. The compound **3** exhibits a "turn-on" response, high selectivity to recognize CN^- with a large Stokes shift of 243 nm, and the limit of detection (LOD) is as low as 1.32 ×10^{-7} M. Also, the low cytotoxicity of compound was applied to detect CN^- in food and cell imaging in living cells such as *C. elegans*, mice and HeLa cells. [61]

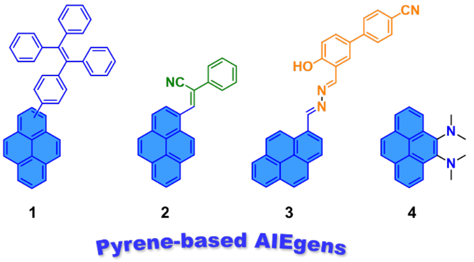

Fig. 5 The typical molecular structure of pyrene-based AIEgens.

Unexpectedly, Dong *et al*. found that both 9-anthraldehyde and 9,10-anthracene-carboxaldehyde displayed clear AIE properties, which can be attributed to the synergistic effect of the steric effects and enhanced intermolecular H-bonding interactions via the presence of the aldehyde group (-CHO). [62] Konishi *et al.* attempted to introduce *N*,*N*-dimethylamine substituents at the 9,10-positions of anthracene or 4,5-positions of pyrene, and the 4,5-bis(*N*,*N*-dimethylamino)pyrene (**4**) all of which exhibit a novel AIE feature, due to the *N*,*N*-dimethylamine units at 4,5-position stabilizing the S_1/S_0 minimum energy conical intersection (MECI).[63] These examples provide a molecular design strategy for improving the luminescence efficiency of pyrene via the ACQ-to-AIE transformation.

Purpose and Perspective

Given the presence of the large π-conjugated aromatic system, pyrene prefers to arrange itself via tight intermolecular π-stacking, which leads to both high charge carrier mobility and hole injection ability.[23] DFT calculations predicted that 2,7-diphenyl-substituted pyrenes exhibit a hole mobility value of 2.95 cm^2 V^{-1} S^{-1}; the electron mobility is 6.24 cm^2 V^{-1} S^{-1} for 4,5-dithenypyrene.[64] Thus, pyrenes are excellent semiconducting materials for the preparation of organic field-effect transistor (OFET) devices.[65] Moreover, with excellent photoluminescence (PL) and high mobility, the triarylamine-decorated pyrenes for example reveal high hole-transporting and emitting properties in OLEDs.[66] On the other hand, when high field-effect transistor active materials were doped into the host of a highly photoluminescence pyrene, the organic light-emitting field-effect transistors (OLEFETs) displayed both thin-film transistors (TFT) and high PL characteristics.[52] However, with the development of organic electronic and fluorescent technologies, pyrene and its derivatives as important luminescent materials have been re-examined by chemists and material scientists. Since the reviews entitled "*Pyrene-Based Materials for Organic Electronics*" and "*Pyrene-fused pyrazaacenes: from small molecules to nanoribbons*" were published by Müllen [23] and Mateo-Alonso, [67] the past decade has seen many researchers not only devote themselves to developing new pyrene-based semiconductors materials for new chemical intermediates, but also focus on their fantastic optical behaviour and high-tech applications, such as organic light-emitting diodes (OLEDs), organic photovoltaic solar cells (OPVs), organic field effect transistors (OFETs), circular polarized luminescence (CPL), phosphorescence, metal-organic frameworks (MOFs), lithium-ion batteries, fluorescent probe, [37] biomedical, etc.

Although there are several review papers that focus on fascinating pyrene-based structures and their potential applications, and the practice application potential is closely related to their aggregation behaviour, the fundamentals of the aggregation behaviour of pyrene-based luminescent materials have rarely been discussed. Herein, we provide a comprehensive review on the progress of the emission and electronic behaviour of new pyrene-based luminescence molecules in the aggregated state. A brief introduction to the fundamental chemical and physical properties of pyrenes is provided to highlight recent developments in efficient design strategies for the preparation of multifunctional pyrene-based luminescent materials. Moreover, this review provides a new perspective for understanding the luminescence mechanism and optoelectronic properties of pyrene-based molecules and establishing the relationship of these factor in the aggregated state or in the solid state. This also provides a set of guidelines for developing new pyrene-based luminescent molecules for practical applications.

Pyrene-based chemical intermediates

The development of new chemical intermediates is fundamental for accessing new advanced functional materials, and offers new opportunities for constructing the next-generation materials and electronics. Due to its special electronic structure, pyrene exhibits a varying electron affinity at different positions, which can be divided into active sites (1-, 3-, 6- and 8-positions), the *K*-region (4-, 5-, 9- and 10-positions) and the nodal plane ((2- and 7-positions), respectively.[53] Dewar *et al.* predicted that the activity of electrophilic substitution of pyrene at 10 substituted positions via DEWAR-PI molecular orbital calculations. The nodal plane 2- and 7-positions show the highest whel and intermediate relative energies up to 20.5 kcal/mol than the active sites (0.1 kcal/mol for 1-, 3-, 6- and 8-positions) and the K-region (8.8 kcal/mol for 4-, 5-, 9- and 10-positions). Thus, the pyrene undergoes an electrophilic substitution preferentially at the active sites.[68] On the other hand, when there are substituents at the active site, this could destroy the molecular symmetry and strengthen the electronic coupling, finally affecting the $S_1 \leftarrow S_0$ and $S_2 \leftarrow S_0$ transitions. Moreover, for the substituents at the node plane, both the HOMO-1 and LUMO+1 energy levels shows a large change, but a limited influence on the HOMO and LUMO level.[25]

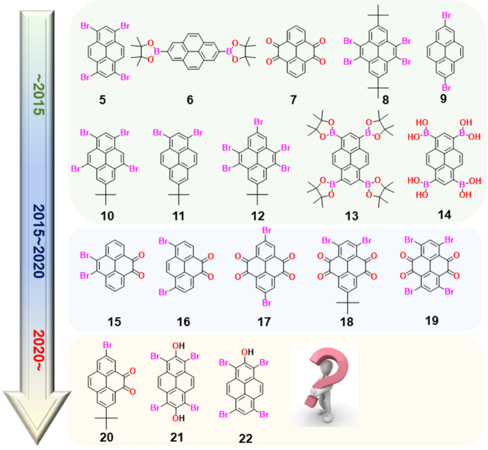

Fig. 6 The synthesis of pyrene-based chemical intermediates.

Given the diversity of active reaction sites, much effort has been devoted to developing new pyrene-based chemical intermediates for various functional applications. As shown in Fig. 6, prior to 2015, researchers have mainly focused on the functionalization of pyrene via a single chemical synthetic method (such as bromination, oxidation, borylation etc.). Classical intermediates, such as the mono-, di- tri- and tetra-substituted bromopyrenes were reported, and the research mainly concentrated on the relationship between the substituent position and the optical properties of the resulting luminescent materials. As the knowledge associated with pyrene syntheses increased, a two-step synthetic strategy was widely utilized for modifying both the active sites and *K*-regions of pyrene. Under such conditions, the reaction order and the types of reaction reagents were found to affect the production of pyrene-based intermediates and their yield. For example, bromination of pyrene-4,5-diketone can be achieved using the 9,10-dibromopyrene, 4,5-

diketone with *N*-bromosuccinimide as the brominating agent, instead of liquid bromine; 9,10-dibromopyrene, 4,5-diketone was obtained. [69, 70] Recently, the integration of pyrene-based semiconductor materials into interdisciplinary research has become an emerging research field that has greatly accelerated the development of pyrene chemistry. Meanwhile, new pyrene-based luminescent materials with novel optoelectronic properties or multifunctional applications have been designed and synthesized from (new) chemical intermediates. Indeed, fundamental research on pyrene-based intermediates has opened a new avenue for developing high-performance functional materials for advanced applications.

The aggregation behaviour of pyrene on substrate surfaces

Organic dyes bound to a solid surfaces via weak interactions (such as van der Waals' forces, π-stacking, etc.) can display unpredictable optical/electronic behaviour, such as fluorescence enhancement/quenching, plasmon resonance enhanced fluorescence,[71] surface-enhanced Raman scattering (SERS), [72] and enhanced photo-induced catalysis ability, [73] etc. Such a hybrid material can be applied to specific applications in high-resolution imaging, analysis technologies and photocatalysis for energy conversion.

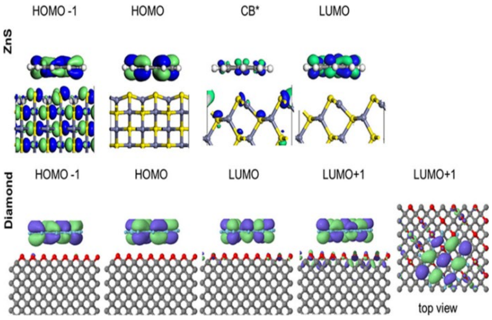

Fig. 7 Single-particle electron density isosurfaces of selected orbitals relevant to the lowest energy excitations for the pyrene@ZnS (upper panels) and pyrene@ Diamond (lower panels) systems. Reproduced from Copyright (2020) American Chemical Society. [74]

Pyrene as a planar structure molecule is easy to deposit on substrates via physical technologies, such as physical vapor deposition or spin coating. McCluskey *et al*. [74] analyzed the optical properties of pyrene deposited on different substrates via spectroscopic methods and first-principle calculations. The results indicated that the pyrene on the surface of both semiconducting and insulating substrates exhibits a monomer emission in the range of 370-400 nm, and the emission intensity was dependent on the substrate. The photoluminescence excitation (PLE) spectra of pyrene show two main absorption peaks at 272 and 335 nm both in solution and in the aggregation state. The absorption peak intensity (272/335 ratio) is dependent on the chosen substrate, which is attributed to the orbital hybridization that takes place between the molecule and the surface. Theoretical results indicated that the PLE absorption peaks at 272 nm and 335 nm are assigned to the HOMO-1→LUMO orbital contribution and HOMO→LUMO transition, respectively (Fig. 7). When the HOMO-1 level falls within the substrate valence band in the ZnS substrate, the hybridization of the molecular state with surface states can enhance the absorption peak at 272 nm, while when the HOMO-1 level falls in the substrate bandgap with negligible hybridization in the diamond substrate, no clear enhanced absorption intensity peak at 272 nm was observed. The surface-enhanced fluorescence phenomenon on the semiconducting and insulating substrates could be an efficient method to improve detection in air pollution monitoring applications.

Furthermore, the emission of pyrenes on gold nanoparticles can be modulated by the use of flexible chains thereby adjusting the orientation degree and the degree of interactions between the metal and organic moiety. [75] Zerbetto *et al*. observed that the compounds **23** and **24** with a short alkyl chain (4C) exhibit a red-shifted emission with an enhancement of the fluorescence quantum yield and a shortening of the excited-state lifetime upon contact with the gold nanoparticles, while compound **25** with a longer alkyl chain (11C) exhibited quenched fluorescence. This unusual emission behaviour is mainly attributed to the competition between the pyrene-pyrene interactions *via* van der Waals forces and the chain-chain interactions to create a different local morphology, but not the odd-even effect. As shown in Fig. 8, when compounds **23**-**25** were combined with gold nanoparticles, the energy level of compound **25** with the long chain could be affected via the dipole moment transition of the electric field of the light, leading to quenched fluorescence. By contrast, when a short chain was present, the orientation of the compounds **23** and **24** could lower the charge transfer state and improve the excited exciton transition. Thus, both examples provide a new perspective for understanding the surface effect in relation to the emission behaviour and electronic transitions of pyrene on various surfaces.

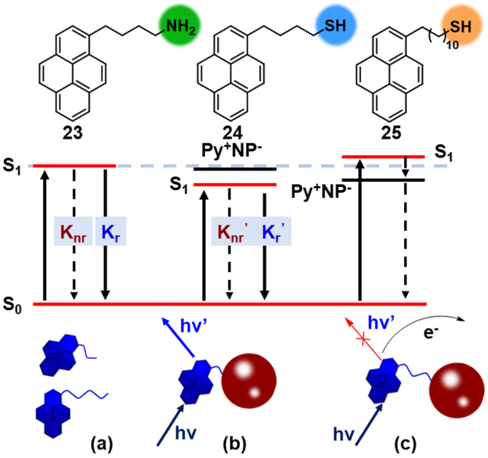

Fig. 8 Molecular structures of **23-25** with different chain lengths and schematic representation of the photophysical processes involving the pyrene ligands. The energies of the fluorescent and the charge state of (a) free pyrene, the pyrene-based emitter with (b) the short chain and (c) the long chain binding to the gold nanoparticle, respectively.

Pyrene-based fluorescent dyes at the substrate surface not only exhibit an unexpected photophysical behaviour, but also the metal surface play an important role to improve the reaction activity. Mateo-Alonso and co-workers[76] have investigated the cyclocondensation reaction of the intermediate tetraketone (O) and tetraamine (A) for the *in-situ* formation of pyrene-fused pyrazaacenes (PPAs) on coinage metal (such as Au, Ag, and Cu) surfaces under ultrahigh vacuum conditions. The results indicated that the different substrates play a significant role to affect the reactive activity and the yield of products. Among them, the Ag (111) surface can promote the cyclocondensation reaction between the ketone groups and the amine to yield PPA-based oligomers with 19 linearly fused rings (Fig. 9). The methodology provides an efficient strategy to construct large π-conjugated nanostructures on solid surfaces.

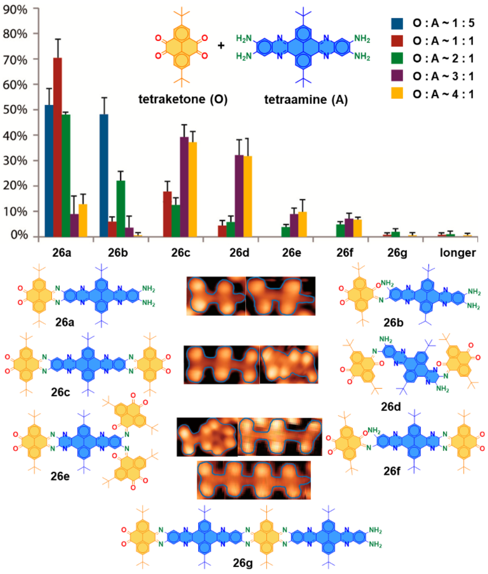

Fig. 9 Condensation products **26a-g** of tetraketone and tetraamine. Reproduced from Copyright (2016) American Chemical Society. [76]

The aggregation behaviour of pyrene-based emitters in solution and in solid state

Pyrene-based intermediates are one of the key building blocks in the manufacture of various high-quality organic materials for organic syntheses, organic electronics, and materials science**.** Up to now, various pyrene-based compounds have been designed and synthesized from the above-mentioned pyrene-based chemical intermediates **5**-**22**. [53] As we know, the 1,3,6,8-tetrabromopyrene **5** is a popular chemical precursor and has been widely used to construct various luminescence materials for many applications. The pyrene core exhibits many advantages, such as (1) good luminescence properties and colour-tunable emission behaviour, (2) facile functionalization, (3) low cost etc.. For example, the 1,3,6,8-arylsubstituted pyrenes **26** with various organic chromophores exhibit a bright emission colour from blue to orange-red, with larger red-shifted emission colour (>65 nm) from 462 nm to 635 nm in the thin film compared to in solution (Figure 6A). [77] The red-shifted emission mainly is attributed to molecular aggregation, via π-π interactions or intermolecular interactions, etc., which is a common phenomenon in traditional pyrene systems. [23] Our group has reported an efficient one-pot synthesis of novel expanding π-conjugated pyreno[2,1-b]furan molecules **27** from the intermediate **22** (Fig. 10BD). A single crystal X-ray diffraction analysis and DFT calculations indicated that these molecules adopted a coplanar framework with a small dihedral angle, leading to a strong face-to-face π-π interaction at a distance of 3.38 Å (Figure 7C). Thus, this series of pyrenes exhibited a large red-shifted emission (> 96 nm) with a maximum peak at 636-640 nm. Thus, the large overlap degree of face-to-face π-π interactions can change the emission peak to long-wavelength. Moreover, these compounds exhibit novel two-photon absorption (TPA) properties with a tuneable TPA cross section (δ) value by regulating the electronic effects of the terminal substituted group of the pyreno[2,1-b]furan molecules, and the compound **27b** with a *tert*-butyl group exhibits the largest TPA cross section of 533 GM. Such compounds could be excellent fluorescence probes for potential applications in bioimaging. [78]

Single-crystal X-ray diffraction provide a visual tool to analyse the molecular arrangement in the aggregation state, but in most cases, crystals suitable for such single-crystal X-ray diffraction analysis are relatively rare. To further understand the aggregation behaviour of larger π-conjugated 1,3,6,8-substituted pyrenes in solution, using pyrene-based octaldehyde **28** as a model compound[79], Sankararaman *et al.* investigated the effect of solvent, concentration and temperature on the aggregation behaviour via PL spectra (Figure 6B). As the concentration increased from 5×10^{-8} M to 10^{-5} M, the emission colour changed from green to red with the maximum emission peak red-shifted from 500 nm to 612 nm. An enhanced emission intensity was observed in cyclohexane, and the short-wavelength emission band was assigned to the monomer emission and the long-wavelength emission band to the excimer emission. Generally, pyrene does not easily form the dimer at concentrations less than 10^{-5} M, however due to the presence of the eight aldehyde functional groups of compound **28**, the strong intermolecular π-π and C-H···O interactions could promote enhanced intermolecular interactions, resulting in an excimer emission both at high concentration or in the solid state. More importantly, the molecular aggregation may be disrupted by the polarity of the solvent, its concentration, and by raising the temperature, which has been verified by concentration-dependent and variable-temperature ^{1}H NMR spectra. More recently, Pandey *et al.* observed that pyrene exhibits an intermolecular excimer at low concentration (20 μM) in deep eutectic solvents constituted of hydrated lanthanide salts and urea. [80] These examples not only offer new characterization methods to investigate the aggregation behaviour of pyrene, but also provide a perspective to understand the aggregation behaviour of pyrene and its derivatives in the solution state.

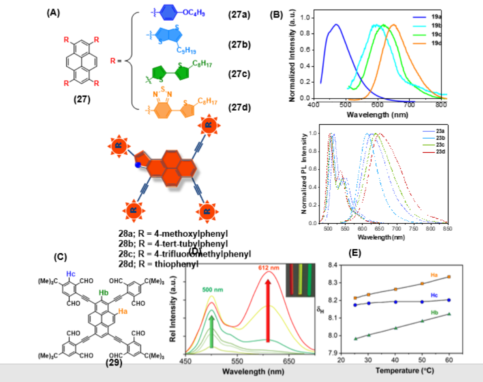

Fig. 10 (A) The molecular structure of 1,3,6,8-tetrakisarypyrenes **27** and the emission spectra of compounds **27** in the solid-state, (B) pyreno[2,1-b]furan molecules **28** and their emission spectra in THF solution and in the solid state. (C) 1,3,6,8-substituted pyrene-based octaaldehyde **29**, (C) Concentration-dependent emission of **29** in cyclohexane (concentration increased from 5 × 10^{-8} M to 10^{-5} M, λ_{ex} = 362 nm), insert: photograph of compounds **29** in $CDCl_3$ under UV irradiation at different concentration, (E) Effect of temperature on proton NMR chemical shifts of **29**. Reproduced from Copyright (2010) [77] & (2006) [79] American Chemical Society.

To enrich the database of pyrene-based luminescence materials, our group has concentrated on developing various pyrene-based chemical intermediates for various potential applications. Recently, the compounds 1,3,6,8-tetrabromo-2,7-dihydroxypyrene **21** and 1,3,6,8-tetrabromo-2-hydroxypyrene **22** were synthesized via a stepwise synthetic route involving borylation, hydroxylation and bromination of pyrene in high yield. Compared to 1,3,6,8-tetrabromopyrene **5**, the new pyrene intermediates exhibited advantages as follows: the bromine atom at the pyrene core could undergo various Pd-catalyzed coupling reactions (such as Suzuki-Miyaura, Sonogashira and Buchwald–Hartwig reaction, etc.), and the presence of a hydroxyl group at the 2- or 2,7-positions of pyrene not only offers the possibility to functionalize the pyrene at these sites, but also can narrow the full width at half maxima (FWHM) of the emission both in solution and in the solid state. [81]

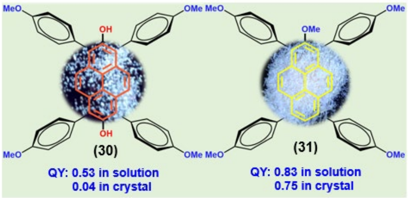

Fig. 11 (A) Molecular structures of compounds **21** and **22** and photographs of the corresponding compounds **21** and **22** in the crystal state under UV irradiation; (B) Molecular structure of compounds **23**; (C) Emission spectra of compounds **23** in THF solution (10^{-5} M) (dotted line) and the solid state (solid line), insert: Photographs of the corresponding compounds as a powder.

For example, 1,3,6,8-tetrakis(4-methoxylphenyl)-2,7-dihydroxypyrene **29** and 1,3,6,8-tetrakis(4-methoxylphenyl)-2-hydroxypyrene **30** were synthesized from bromopyrene intermediates **21**or **22** using 4-methoxylphenyl boronic acids in considerable yield. Due to the presence of the -OH group, there are several types of hydrogen bonds in the unit cell, leading to weak fluorescence in the crystalline state. Moreover, compound **29** emits a dual emission at 454 and 500 nm, with Commission International Eclairage (CIE) coordinates of (0.19, 0.30), the latter originating from the excimer emission. When the -OH group was replaced by a methoxyl group, compound **30** also exhibited a dual emission with the maximum emission peak at 446 nm with a weak shoulder peak at 555 nm (CIE: x=0.17, y=0.18). The fluorescence quantum yield was enhanced from 0.04 (in compound **29**) to 0.75 (in compound **30**) in the crystalline state, indicating that the -OH group can strengthen the intermolecular interaction via hydrogen-bonds, while weaker hydrogen-bonding interactions contribute to quenching the fluorescence efficiency (Fig. 11). In addition, these compounds containing a hydroxyl group at the 2,7-positions display a narrower FWHM of 23 nm in the solid state compared to 1,3,6,8-subsitituted pyrene. [81] In addition, the XRD technologies offer an efficient approach for the analysis of the effect of the size of nanoparticles, layer spacing and the morphology to the emission of the pyrene-based luminescent materials. Thus, this provides a feasible methodology to analysis the aggregation behaviour.

Aggregated pyrene-based molecules for fluorescent probes

Much effort has been devoted to the development of novel organic luminescent materials as fluorescent probes for explosives, metal ion detection, [82] as well as disease diagnosis and treatment. [83] [84] On the one hand, as an excellent fluorescent probe, the pyrene-based fluorophores show a high selectivity and specificity to metal ions and anions. On the other hand, pyrene and its derivatives with strong intermolecular interactions can quench the fluorescence in the aggregated state, and the "turn-off" luminescent behaviour of pyrenes could be utilized for the recognition and determination of metal ions, [85] organic gases, hazards etc. For example, pyrenes can be employed as excellent fluorescence probes for nitro-explosives detection.[86] Trinitrotoluene (TNT) can interact with pyrene, and the excited electron of pyrene can transfer to the LUMO of the TNT via a photo-induced electron transfer (PET) process,[87] resulting in fluorescence quenching (Figure 11A). Wang and co-workers[88] reported three alkyl chain-dependent, 1,3,6,8-tetrakisarylsubstituted pyrenes **31** with intense blue emission (436~438 nm) and high fluorescence quantum yield (QY) efficiency (> 0.86) in solution. However, the emission of these compounds could be red-shifted to 472~492 nm with decreased QY efficiency (< 0.36) in the solid state, due to enhanced π-π interactions. Interestingly, the emission behaviour was affected by the odd- and even-numbered alkyl chains, and the 1,3,6,8-tetrakis (pentylphenyl)pyrene (odd number) **31b** exhibited a crystallization-induced emission enhancement with QY of 0.72 in the crystal state. The odd-even effect also plays a significant role in detecting the nitro-explosives. For example, the 1,3,6,8-tetrakis(pentylphenyl)pyrene shows high sensitivity and selectivity for *ortho*-nitroaniline (*o*-NA) with a luminescence quenching efficiency up to 92.1%, and a limit of detection (LOD) less than 9.99×10^{-8} M in solution (Figure 11C). Moreover, when *o*-NA was in contact with the test strip coated with compound **32b**, the emission was near quenched within 5 min. Thus, these pyrene-based luminescent materials can be considered excellent fluorescent probes for selective detection of nitro-explosives.

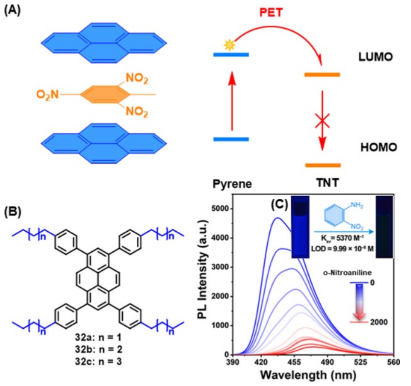

Fig. 12 (A) Schematic representation of the interaction model of pyrene with TNT and its possible photoinduced electron transfer mechanism for sensing trinitrotoluene by pyrene; (B) molecular structure of **32**; (C) the emission intensity change on detection of nitroaniline *versus* the concentration of the trinitrotoluene added, insert: photograph of **32b** detecting the nitroaniline under UV irradiation. Reproduced from Copyright (2023) Elsevier Ltd. [88]

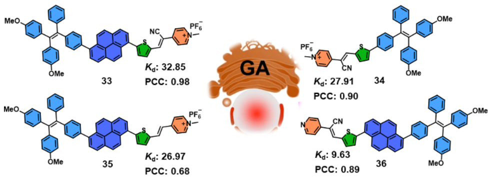

Fig. 13 (a) Molecular structure of **33**-**36** and the corresponding ROS generation abilities (k_d: nmol/min): decomposition rates; Reproduced from Copyright (2022) Nature Publishing Group.[89]

Photodynamic therapy (PDT) has become an important treatment option for cancer cell clearance and bacterial death, due to its advantages of non-invasiveness and spatiotemporal selectivity. Photosensitizers are a key therapeutic agent of PDT and play a pivotal role in inducing the oxygen to be the singlet oxygen ($^1O_2$) or reactive oxygen species (ROS) to kill cancer cells and bacteria under irradiation. Pyrene is sensitive to the external microenvironment, resulting in distinguishable optical behaviour via intra-/inter-molecular interactions. Moreover, the presence of the pyrene unit is beneficial for reducing the energy gap between the lowest singlet state (S_1) and the lowest triplet state (T_1) (ΔE_{ST}) for enhancing fast ISC rate and high $^1O_2$ generation capacity. Guo and coworkers reported four pyrene-based photosensitizers **32**-**35** with AIE characteristics for effective cancer PDT. In particular, the AIEgens **32** can target the Golgi apparatus (GA) via caveolin/raft-mediated endocytosis with a Pearson correlation coefficient up to 0.98 (Figure 12). Moreover, the homologous pyrene-based AIEgens also possess a high ROS generation rate. Thus, this example offers a molecular design strategy for the development of pyrene-based AIEgens for use in PDT. [89]

Molecular motion of pyrene-based molecules in the aggregated state

Disordered motion is an intrinsic property of molecules, and this process is uncontrollable in the sub-picoseconds time scale; the typical disordered motion is Brownian movement. [90] Such molecular motion has been well investigated in gas and liquid systems. However, few examples have focused on the molecular motion of molecules in the aggregated state or solid state. [91] The main reason is that the strong inter-/intra-molecular interactions can also fix the molecular movement in the solid-state, but limited experimental technologies make it difficult to monitor the imperceptible changes in their physical and chemical properties. Although single crystal X-ray diffraction and solid-state nuclear magnetic resonance (NMR) spectroscopy offer a visual tool for gaining insight into molecular motion in the solid-state, there remain some limitations. For example, the greatest challenge is cultivating high-quality suitable crystals of complicated compounds suitable for single crystal X-ray diffraction analysis.

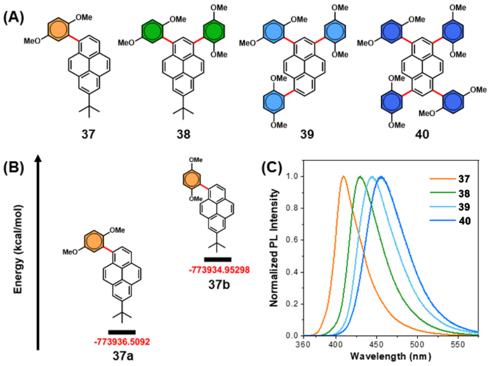

Fig. 14 (A) The pyrene-based molecules **36**-**39**; (B) Potential energy surface for **33** (Gaussian 09 W (B3LYP/6-311G(d,p) basis set); (C) Emission spectra of compounds **36**-**39** in the solid state. Reproduced from the author.

Previously, our group reported a set of new dimethoxyphenyl-decorated pyrene-based compounds **36**-**39** for investigating the effect of molecular conformation on the photophysical properties, [92] where the sterically bulky 2,5-dimethoxyphenyl group acts as a rotator to produce various molecular conformations via molecular rotation (Figure 14). Density functional theory (DFT) calculations indicated that the conformers of each compound have small energy barriers (less than 2.61 kal/mol), resulting in each molecule possessing various conformers for the same system via a molecular rotation (Figure 14B). The use of more substituents allows for more conformers. Moreover, the emission behaviour is closely related to the number of molecular conformations, and the diversiform can cause a broaden full width at half maxima (FWHM) emission for the pyrene-based luminescence materials in the aggregated state. As show in Figure 13C, the FWHM increased from 37 nm to 57 nm from compound **36** to **39** (Figure 14C). Such research offers a new molecular design guideline to endow organic luminescence materials with high colour purity.

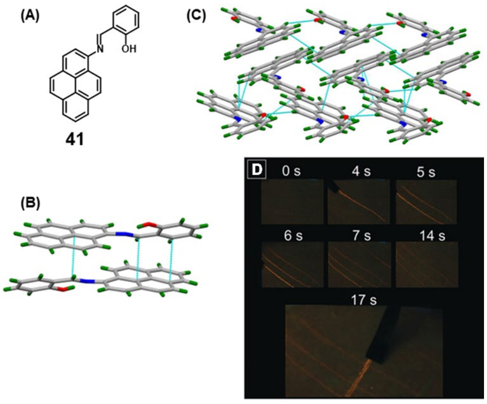

Fig. 15 (A) The pyrene-based Schiff-base **40**; (B) and (C) The molecular packing via weak interactions, (D) Visual demonstration of the fast turn-on/off fluorescence processes. Reproduced from Copyright (2019) Wiley-VCH Verlag GmbH & Co. KGaA. [93]

Eyes are very sensitive to light in dark environments, even to faint light, but very sluggish to daylight. In another words, the "light-up" type luminescent materials could be more sensitive to detect changes in the microenvironment. Inspired by the AIE phenomenon, Tang *et al*. presented a new AIE luminogen (AIEgens), (*E*)-2-[(pyren-1-ylimino)methyl]phenol **41** (Figure 14A), which exhibited bright emission in the amorphous state but was non-emissive in the crystalline state, due to the strong π-π interactions, resulting in a strong fluorescence quenching in the crystalline state. Single-crystal X-ray diffraction analysis revealed that the multiple π-network plays a crucial role to drive the formation of the tight molecular packing dominated by π-π stacking, leading to a crystallization-induced quenching phenomenon (Figure 14B). Interestingly, the dark crystalline form of AIEgen **41** could light-up its emission under external stimuli, which also quickly disappears with an average lifetime of 20 s (Figures 14C-14E). The emission turn-on and a fast self-recovery process can be explained by the disruption of the π-π interactions, which results in a fluorescence turn-on. The molecular morphology changed from the crystalline state to amorphous, but the spontaneous and fast molecular motion was beneficial to a molecular rearrangement to the π-network at room temperature, driven by the formation of π-π interactions, leading to a weaken emission. [93]

Aggregated pyrene-based emitters with white-light emission

Natural sunlight is composed of different wavelengths of light in the whole visible light region, to form a vivid white light, while artificial white-light is generated from white-light-emitting compounds, including a mixture component of blue/yellow emitters, single molecular white-light emitters. Moreover, the latter has attracted great attention from researchers, due to their potential commercial value in white-organic light-emitting devices as well as for fundamental research on luminescence mechanisms. Tang and co-workers have summarized the fundamental strategies to achieve efficient organic white-light-emitters. [94] Inspired by the weak electron communication of the nodal plane of pyrene by the carbon atoms at the 2,7-positions, Feng *et al*. synthesized an asymmetrical tetraphenylethylene (TPE)-substituted pyrene **42** with AIE characteristics, where naked TPE and diethylaminophenyl-substituted TPE units were introduced at the 2,7-positions of pyrene (Figure 15A).[95] When the ethoxylphenyl-substituted TPE unit was at the 2-position, compound **42** emitted blue emission ($\lambda_{max\ em}$ = 474 nm) with a high quantum yield of 0.47 in the thin film. Interestingly, the compound **42** with asymmetric TPE units (blue and yellow fluorophores) at the 2,7-positions, displays a tuneable emission from blue (435 nm) to warm white (dual emission: 436 nm and 538 nm, CIE: x = 0.30 and y = 0.41), then to yellow emission (533 nm) as the water fraction increased from 0 to 99%. (Figures 16B-C). This provides a molecular strategy to synthesize pyrene-based single molecules with white-light emission and AIE characteristics.

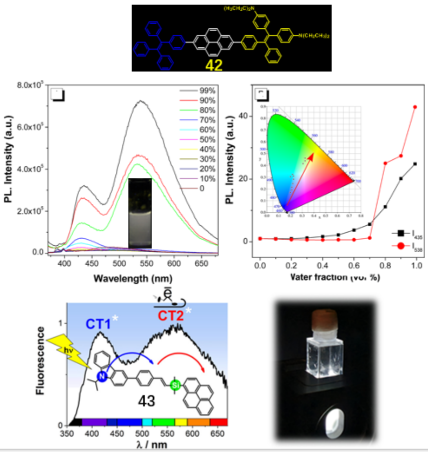

Fig. 16 (A) The asymmetric 2,7-substituted pyrene-based AIEgen **42**; (B) PL spectra of **42** in THF/water mixtures with different water fractions (f_w); (C) Plot of I/I$_0$ *versus* the composition of a THF/water mixture of **42**, where I$_0$ is the PL intensity in pure THF solution at 435 nm or 538 nm. Inset: CIE coordinates of the emission of **43** in THF/water mixtures with different f_w (0–

99 vol%). Reproduced from the author. (D) The emission spectra of pyrene-based emitter containing a silicon atom **43** in acetonitrile solvent; (E) Photograph of compound **43** with white-light emission in acetonitrile. Reproduced from Copyright (2020) American Chemical Society.

Similarly, when an Si spacer is employed as a bridge, each substituent still retains their unique optical properties. Although the π-communication between the substituents has been broken, the intramolecular excited-state processes continue to work.[96] Based on this fundamental knowledge, Bayda-Smykaj *et al*. reported a new charge-transfer molecule **43** by incorporating styrylcarbazole (D) and pyrene (A) using a dimethylsilyl bridge. Compound **43** with the D-π-A characteristic exhibits three completely different types of emission depending on solvent polarity. [97] The maximum emission band is at *ca*. 375 nm with a long-lived fluorescence lifetime (ι = 112 ns) in the non-polar solvent hexane, which originates from the local excited state emission of pyrene. For mid-range polarity solvents (e.g. THF and DCM), the compound exhibits a broad charge-transfer emission (CT1, λ_{em} = 402 nm, Φ_f = 0.64, ι = 16.4 ns), which is ascribed to the intramolecular charge transfer (ICT) process that occurs at the styrylcarbazole units. More importantly, compound **43** emits a white-light emission with CIE coordinates of (x = 0.33 and y = 0.36) and exhibits a dual emission a CT1 emission at 416 nm with another CT emission (CT2) with a λ_{em} = 560 nm (ι = 15 ns) in the polar solvent acetonitrile. The CT2 emission is originating from the styrelcarbazole moiety to the pyrene aromatic unit (Figure 15D-E). These examples and molecular strategies open a new avenue for constructing high-performance organic white-light emission materials.

Aggregated pyrene-based emitters with phosphorescence

Most polycyclic aromatic hydrocarbons usually exhibit bright emission but no phosphorescence at room temperature, due to the spin-forbidden transition of $S_1 \rightarrow T_1$ via the ISC process. Pyrene as an excellent fluorophore, emits intense fluorescence or excimer emission depending on the degree of aggregation. However, its phosphorescence has rarely been observed under a mild environment. As shown in Scheme 2, pyrene has a large ΔE_{ST} between S_1 and T_1 up to 1.737 eV, and the larger ΔE_{ST} is unfavourable for accelerating the ISC efficiency and achieving the phosphorescence. To improve the ISC process and enhance the spin-orbit coupling and block the nonradiative decays, efficient approaches (such as the heavy atom effect, [98] halogen bonding, [99] n-π* transitions, and charge transfer) have been demonstrated to realize a high-efficiency phosphorescence, even room-temperature phosphorescence (RTP).

Gabbaı *et al*. reported that the self-assembled cocrystals between the trinuclear mercury(II) complex [(o-C_6F_4Hg)$_3$] and pyrene resulted in the formation of a 1:1 adduct, which emitted red RTP with a phosphorescence lifetime of 985±11 μ s. A crystal structure analysis reveals a binary supramolecular stacked structure where the pyrene molecules are arranged in parallel with the complex Hg(II)@pyrene (Figure 17A).[100] On the other hand, due to the toxicity of heavy metals, enormous efforts have been devoted to exploring pure organic phosphorescence materials. Doping the organic phosphors into selected host materials could be an alternative strategy to achieve RTP. [101] Tang *et al*. presented a feasible strategy to achieve persistent RTP via strong electrostatic interaction between electron-rich 1-methoxypyrene and electron-deficient molecules of the matrix polyacrylonitrile (PAN). As shown in Figure 17B-D, the doped films emitted blue fluorescence (λ_{em} = 410 nm) under UV irradiation. After delaying 1 ms, a red afterglow was observed with the maximum band at 617 nm with a lifetime of 11.7 ms. DFT calculations indicated that the value of the binding energies between the PAN and compound **44** is 17.64 Kcal mol^{-1}, implying a strong noncovalent interaction between the two species. This provides a new design strategy to achieve pure persistent RTP from amorphous films consisting of strong electron-rich organic dyes. [102]

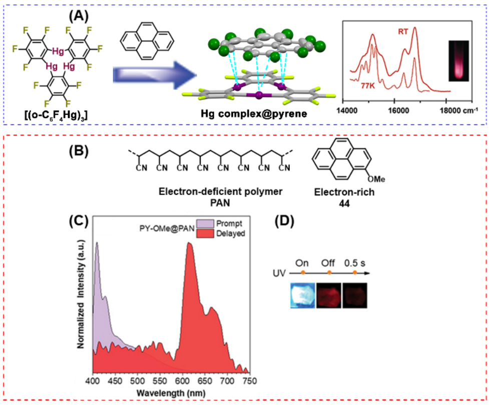

Fig. 17 (A) The self-assembled mercury (II) complex with pyrene with red RTP properties in the solid state, Reproduced from Copyright (2003) American Chemical Society. [100] (B) and (C) The emission and phosphorescence spectra of the self-assembly architecture between electron-deficient PAN and electron-rich **44** in doped film; (D) Luminescence photographs of doped films under UV irradiation and after removal of UV irradiation with different duration times. Reproduced from Copyright (2021) Wiley-VCH Verlag GmbH & Co. KGaA. [102]

Pyrene derivatives with planar structures display mechanoluminescence (ML) or mechanochromism (MC) under external stimuli. [57] [103] Given pyrene prefers to form a dimer via π-π stacking, the planar pyrene-based intermediate of 4-bpin-2,7-di-*tert*-butylpyrene **46** [104] exhibits a dual emission with monomer-ML and excimer-ML properties, while 2,7-di-*tert*-butylpyrene **45** and 4-bromo-2,7-di-*tert*-butylpyrene **47** are ML-active (Figures 18A-C). The MC phenomena is mainly originating from the enhanced π–π interactions and increased exciton coupling each other under stimuli. On the other hand, strong intermolecular interactions are beneficial and result in ML phenomena (Fig. 18). [105] Thus, the example provides a new perspective to understand the MC and ML mechanisms. More interestingly, the new intermediate pyrene-1,3,6,8-tetraboronic ester **13** not only displays a reverse mechano-driven fluorescence colour change from blue (420 nm) to yellow (530 nm) with enhanced emission, but also exhibits mechano-driven phosphorescence both in 2-methyltetrahydrofuran (MTHF) solution at 77K and in the solid at room temperature under air with a phosphorescence quantum yield of 2.9%.[106] This phenomena is mainly contributing to the strong intermolecular electronic coupling and a low singlet–triplet energy gap of the dimer assembly.

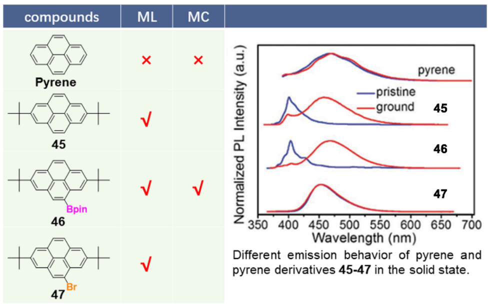

Fig. 18 The molecular structure of the pyrene and pyrene derivatives **45**-**47** and their different emission behaviour in solid state. Inset: PL spectra of pyrene and pyrene derivatives **45**-**47** in the pristine (blue line) and ground states (red line). Reproduced from Copyright (2018) Wiley-VCH Verlag GmbH & Co. KGaA.[105]

Pyrene-based dimer molecules with circularly polarized luminescence (CPL) properties

Circularly polarized luminescence is generated from chiral systems, which can emit differential emission of left-hand and right-handed circularly polarized (CP) light, and has attracted widespread interest due to their promising applications in 3D displays, optical information storage, chiral sensors, bioencoding, as well as in asymmetric photochemical synthesis.[107] The degree of CPL is evaluated by the luminescence dissymmetry factor (g_{lum}), which is defined in the equation as shown below:

$$g_{lum} = 2 \times \frac{I_L - I_R}{I_L + I_R} = 2 \times \frac{CPL}{I}$$

where I_L and I_R are the intensity of left-handed and right-handed circularly polarized light, and I is the sum of the emission intensity of I_L and I_R. Theoretically, the highest value of $|g_{\mathrm{lum}}|$ is 2, meaning that the pure CPL emission forms left-handed or right-handed polarized emission. The basic fact is that the pure chiral organic systems show a relatively low g_{lum} value of less than 0.01,[108] due to the strong electric dipole character of their electronic transitions.[109] Thus, much effort has been devoted to exploring new high-performance chiral systems with large g_{lum} value for various practical applications. The molecular self-assembly system is one of the most important strategies to amplify the glum values via different electronic transition processes, including Förster resonance energy transfer (FRET), photon up-conversion (UC), charge transfer (CT), or organic radical emission.[110] However, it is worth noting that the CPL properties for this chiral system are closely associated with the excited state of chiral emitters. Thus, the development of high-efficiency CPL properties of organic luminescent materials with high g_{lum} is a high-priority task and a significant challenge.

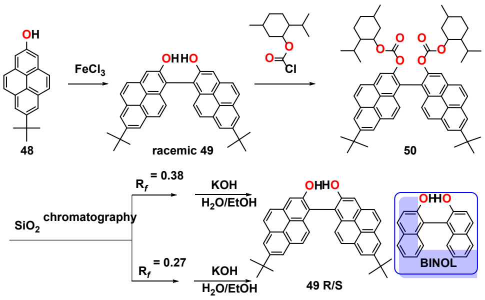

Fig. 19 Synthesis and separation procedure of pyrene-based axially chiral molecule R-**49** and S-**49** from 7-(*tert*-butyl)pyren-2-ol **48 R/S**.

Pyrene is a typical chromophore with bright emission, long lifetime and high quantum yield, which could be an ideal candidate for CPL research. Inspired by the classical chiral molecule 1,1'-binaphthalen-2,2'-diol (BINOL), Sugiura *et al.*[111] synthesized new pyrene-based chiral molecules for CPL spectroscopy from 2-hydroxy,7-*tert*-butyl-pyrene **47**, which was involved in a Lewis-acid catalyzed C–H activation to afford racemic *rac*-bipyrenol **48**, where the *tert*-butyl group at the 7-position can increase the solubility of the target compound. Further treatment with (-)-menthyl chloroformate quantitatively afforded a diastereo-mixture of **49**, which can readily be separated by column chromatography with retardation factors (R_f-value) of 0.38 for **R-50**, and 0.27 for **S-50**. Subsequently, the corresponding diastereomers R/S- were involved in a base-catalyzed hydrolysis to afford optically pure R/S-**50** (Figure 19). The pyrene-based dimer shows a clear CPL spectrum with the $|g_{\mathrm{lum}}|$ value of 3.6×10^{-4}. Compared to 1,1'-binaphthalen-2,2'-diol (BINOL), the pyrene-based chiral molecule exhibits a higher quantum yield, larger g_{lum} value and large chiral spaces, which could be a new chiral core for constructing high-performance chiral systems. Indeed, when the hydroxyl group was replaced by nucleophilic substituents, such as (1)-menthyl chloroformate,[111] methyl, thiol, alkyl linkages and amine, a high quantum yield and clear CPL spectra were evident.[112]

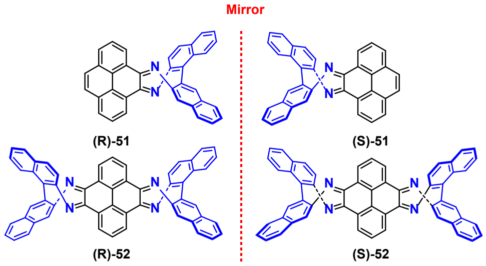

Fig. 20 Molecular structures of 4,5-substituted pyrene-based chiral molecules R/S-**62** and 4,5,9,10--substituted pyrene-based chiral molecules R/S-**63**.

By integrating the BINOL units into the 4-,5- or 4-,5-,9- and 10-positions of pyrene, Jiang *et al.*[113] synthesized the chiral pyrene-based binaphthalene compounds **51**-**52** (Figure 22). All compounds show mirror image CD spectra in the entire absorption region with CD intensity of > 10^{-2} deg M^{-1} cm^{-1}, indicating that the chiral information can transfer from the chiral BINOL group(s) and the pyrene ring. However, both compounds show weak fluorescence in chloroform with maximum emission peaks at 393 nm (Φ_f = 0.03) and 460 nm (Φ_f = 0.02), respectively. The fluorescence behaviour in the solid state was not discussed. Besides, this example offers useful insights into designing a new pyrene-based chiral systems by a chiral induction mechanism.

On the other hand, the more popular approach to construct pyrene-based chiral molecules is to introduce the chiral group into the pyrene, for example, decorating the pyrene at the 1,6-positions or 2,7-positions using BINOLs unit as substituent groups, Ema *et al*. reported a set of new pyrene-based CPL luminescence molecules **53**-**59** (Figure 20). The monomer of compound (R,R)-**53** displays a blue emission (431 nm) without a CPL signal when the concentration was less than ~10^{-5} M. As the concentration increased, the compound exhibits an excimer emission (527 nm) with a clear CPL signal with |g_{lum}| of -5.0 ×10^{-4} when the concentration is up to 4.0 × 10^{-3} M. The concentration-dependent emission spectra of compounds **53**-**59** indicated that high concentration is better for CPL activity, Moreover, in the absence of a carbonyl group, the compounds **60** and **61** exhibit weak CPL. Thus, the presence of the -OH and carbonyl groups are essential for the formation of the excimer, resulting in an intense (-)-CPL signal. Interestingly, the compound (R,R)-**54** exhibited solvent-dependent inversion of the sign of circularly polarized luminescence (CPL) without a change in the emission wavelength, and the |glum| values are up to -0.012 and +0.012 in the nonpolar (toluene) and polar (DMSO) solution with opposite CPL signs. This switching CPL property originates from the inversion of excimer chirality caused by the presence or absence of intermolecular hydrogen bonds in the excited state. [114]

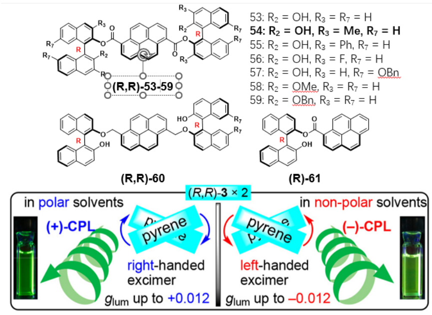

Fig. 21 Molecular structures of **53–61** and structural and CPL properties of (R,R)-**54,** Reproduced from Copyright (2020) American Chemical Society.[114]

The formation of the face-to-face intramolecular excimer of pyrene is contributing to improving the |glum| values. [114] When the two pyrene molecules were arranged in an asymmetrically twisted configuration in a γ-cyclodextrin (CD) cavity, the intramolecular excimer systems can induce CPL with |glum| of 0.0071-0.012. [115] In fact, Ema *et al*. [116] also reported a set of simple D2-symmetric macrocycles consisting of pyrene and (R)-BINOL units, where the ether linkers (-OCH_2-, -CH_2O- or –CO-) were connected to the 1,6-positions or 2,7-positions of the pyrene core (Figure 21). The two pyrene rings were fixed by the BINOL, resulting in a left-handed twist excimer with completely parallel µ and m. The CD signal of **62**, **64** and **65** exhibited (-)-CD, and **63** exhibits (+)-CD, indicating that the CD signal of these compounds originate from the pyrenes but is not a BINOL-related induced CD. Due to the presence of the ether linker, compounds **62** and **63** (containing -OCH_2-) display an excimer fluorescence (487 nm and 475 nm) and compounds **64** and **65** (containing -CH_2O-) display a monomer emission (431 nm and 408 nm) in CH_2Cl_2. The regioisomers (R,R)-**62** and (R,R)-**63** exhibit clear CPL with high |glum| values of 0.053, 0.022, respectively. The (R,R)-**57** still retained an intense CPL in the solid state (g_{lum}= 0.011, Φ_{fl}=0.06, λ_{em}, max=494 nm). However, the excimer CPL of (R,R)-**64** and (R,R)-**65** were detected with |glum| values of 0.0024 and 0.0084, but monomer CPL signals were not observed. In addition, as a control compound, the chiral molecule (R,R)-**66** exhibited an excimer emission at 486 with a relatively large |glum| value of 0.032. Both examples provide a new perspective for the molecular design of pyrene-based CPL molecules to improve the glum value via strengthening the inter-/intramolecular rigid dimer structure.

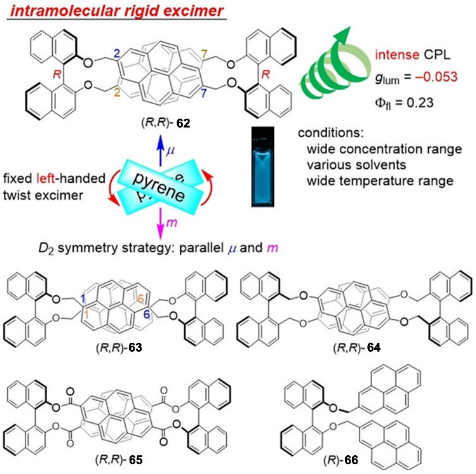

Fig. 22 Molecular structures of (R,R)-**62**-**65** and (R)-**66** and highlights of the CPL properties. Reproduced from Copyright (2022) Wiley-VCH Verlag GmbH & Co. KGaA. [116]

Helicenes have received special attention due to their sterically distorted structure and high circular dichroism values and fantastic electronic properties, [117] [118] but the synthesis and characterization of expanded π-conjugated helicenes remain a challenge because the methodology of controllable *ortho*-fused aromatic rings is rare. [119] Pyrene shows a differentiated position-dependent reactivity at the active sites, K-region, and node plane, and could be an excellent candidate for constructing pyrene-fused [*n*]helicenes with great chiroptical properties. Yamato *et al*. synthesized a set of new pyrene-based [4]helicenes **67** and **68**, [120] and pyrene-based [5]helicenes **69**-**71** [121] [122] by a Wittig reaction and photo-induced cyclization reactions (Figure 23). All the compounds exhibited bright blue emission, but the chiroptical properties were not discussed.

Recently, Ravat *et al*. presented two kinds of C2- and C1-symmetric pyrene-fused [5]helicene **72** and **73**, which were synthesized via a one-pot Suzuki coupling−C−H activation reaction or a Scholl-type oxidative cyclodehydrogenation reaction between 2,2′-diiodo-8,8′-dimethyl-1,1′- binaphthalene and 2-(2,7-di-*tert*-butylpyren-4-yl)-4,4,5,5-tetramethyl- 1,3,2-dioxaborolane. [123] Compound **73** exhibits a larger absorption dissymmetry factor (g_{abs} = 2.3×10^{-3} at 415 nm) compared to compound **72** (g_{abs} = 1.5×10^{-3} at 415 nm) with similar g_{lum} (2.1×10^{-3}). Following the same synthetic approach, the C1- and C2-symmetric pyrene-fused [7]helicenes **74** and **75** were also synthesized for expanding the π-conjugation compared to compounds **72** and **73**, , and as the phenyl ring fused, the absorption dissymmetry factor ($g_{abs} = 2.5\times10^{-3}$ at 421 nm for **75** and $g_{abs} = 2.7\times10^{-3}$ at 402 nm for **74**) was increased from the [5] helicene to [7] helicene, and the luminescence dissymmetry factor (glum) for **74** (2.6×10^{-3} at 490 nm) is slightly higher than that of **75** (1.3×10^{-3} at 471 nm). [124] Despite the similar molecular structures for **72**-**73** and **74**-**75,** the C1- symmetric **73** and **74** show a relatively higher quantum yield and g_{lum} compared to the C2-symmetric pyrene-fused[*n*]helicenes, and maybe the former shows a more rigid molecular conformation, due to the presence of the *tert*-butyl group at the 7-position of pyrene (Figure 23).

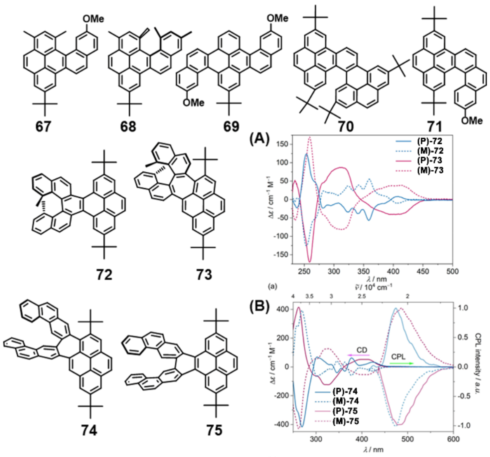

Fig. 23 Pyrene-based helicenes **67**-**75**; (A) Electronic CD spectra of P- and M- enantiomers of **72** and **73** and (B) P- and M- enantiomers **74** and **75** in DCM (10^{-5} M). Reproduced from Copyright (2021) (2022)& American Chemical Society . [123], [124]

On the other hand, Liu *et al*. developed a symmetric V-shaped chiral molecule by linking achiral pyrene cores to *trans*-1,2-cyclohexane diamine units **76** (Figure 24), where the pyrene moieties prefer to form an intramolecular excimer, and self-assemble to a helical hexagonal packing, resulting in spacer-dependent circular dichroism (CD) and CPL properties. As the chain (spacers) increased, the molecule becomes more flexible, thus the g_{CD} values of rigid **76a**, semirigid **76b** and flexible **76c** were 5.92×10^{-4} (344 nm), 1.03×10^{-4} (351 nm) and 0.69×10^{-4} (347 nm), respectively. Moreover, the shorter chain in **76a** could increase the molecular rigidity, leading to amplified chirality properties up to *ca*. 61-fold g_{CD} (3.59×10^{-2}) and 53-fold g_{lum} (2.64×10^{-2}), compared to **76c**. This example indicated that molecular rigidity, molecular conformation, and supramolecular self-assembly can greatly improve the molecular chirality transfer and excimer formation, resulting in an amplified CPL signal. [125]

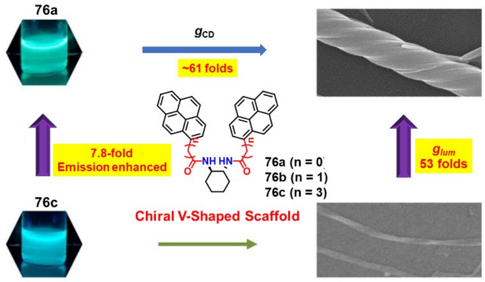

Fig. 24 Molecular structures (R-enantiomers) of symmetric and chiral V-shaped molecules **76** and highlights of the CPL properties. Reproduced from Copyright (2021) Wiley-VCH Verlag GmbH & Co. KGaA. [125]

Furthermore, Liu's research group[126] reported a mechanically interlocked strategy to construct a monolayer 2D chiral polyrotaxane (2D CPR) **77** with CPL activity via a self-assembled host–guest interaction, where the *β*-cyclodextrin (β_{CD}) acts as a chiral macrocyclic, where encapsulated 1,6-diaminopyrene acts as a bridge (Figure 25). The 2D CPR **77** exhibits blue emission with a strong Tyndall effect in solution. Moreover, the layered 2D CPR **77** displayed a strong induced negative CPL signal at 450 nm. Supramolecular self-assembly is a popular strategy to improve electronic circular dichroism and CPL properties of pyrene-based chromophores. [127] Yang *et al*. also reported pyrene-substituted *γ*-CDs, which can form aggregated nanostructures with chiroptical properties by supramolecular assembly, resulting in high g_{abs} and g_{lum} values up to 4.3×10^{-2} and 5.3×10^{-2}, respectively. [128] These examples open up new vistas for the development of high g-value pyrene-based CPL materials via supramolecular self-assembly.

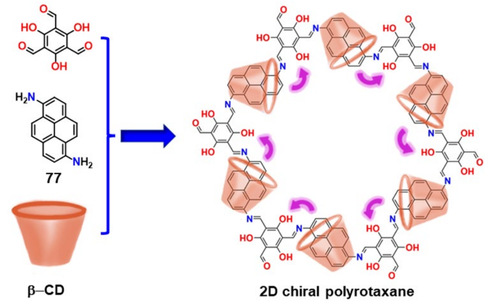

Fig. 25 Synthetic process for two-dimensional chiral polyrotaxane via host–guest induced chirality from C3, 1,6-dianmionpyrene **77** and β-cyclodextrin (β–CD) with a monolayer structure. Reproduced from Copyright (2022) Wiley-VCH Verlag GmbH & Co. KGaA. [126]

Pyrene-based self-assembly supramolecular architectures

Pyrene-based self-assembly architectures are an important member of the organic luminescent materials family, which contains metal-organic frameworks (MOFs), covalent organic frameworks (COFs), hydrogen-bonded organic frameworks (HOFs), as well as self-assembly complexes, due to their well-ordered nanostructures with tuneable molecular channels, as well as impressive optical behaviour in the aggregated state. These self-assembly architectures are widely applied in gas storage, [129] separation, [130] catalysis, [131] [132] [133, 134] fluorescence probes, [135] [136]electrolytes, [137] as well as biosensing and bioimaging. [138]

Pyrene-based MOFs with enhanced emission

Generally, linear-shaped 2,7-pyrene dicarboxylic acid **78**, and star-shaped 1,3,6,8-tetra(4-pyridine) pyrene **82** are remarkable organic ligands for constructing fantastic topological structures with lanthanide metal ions, [136, 139] and metal clusters. [140] These ligands show bright emission in solution but can quench the fluorescence in the aggregation state, due to strong intermolecular interactions. The pro-ligand 1,3,6,8-tetra(4'-carboxylphenyl)pyrene **80** (**TBAPy**) is aggregation-induced enhanced emission (AIEE) active. [141] [142] Once the pro-ligands are coordinated with metal ions, such as zinc (II), the pyrene-based MOFs with fantastic topologies emit intense emission in the aggregation state. [143] Recently, Smit,[144] Deria[145] with co-workers summarized the synthesis of pyrene-based ligands for the construction various of pyrene-based MOFs by the incorporation of metals or ligands in the structure, and their potential applications have been discussed in these reviews. Moreover, more than 200 articles and reviews related to pyrene-based MOFs and their applications have been published according to the Clarivate database. In this section, we attempted to select some of the latest, classical research work for understanding the optical and electrical conductivity behaviour of pyrene-based self-assembly architectures in an aggregation state.

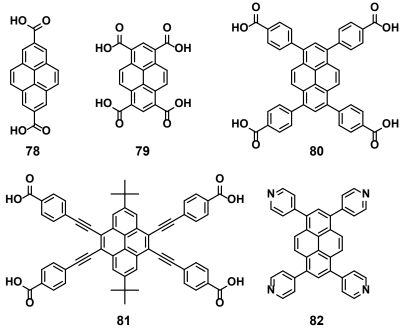

Fig. 26 The typical pyrene-based pro-ligands **78**-**82** for constructing pyrene-based MOFs.

Pyrene-based MOFs with intensity fluorescent have attracted extensive attention due to their potential applications. Rosseinsky reported a pyrene-based microporous fluorescent MOF (**In@80**) via pro-ligand **80** coordinating with the rare-earth metal In(II) ion, and the resultant MOF exhibits highly emissive, good quantum yield (6.7%) and millisecond fluorescent lifetime. When the **In@80** was exposed to anhydrous DMF solvent, the emission of **In@80(DMF)** containing DMF show a blue-shifted emission with enhanced emission intensity and a maximum emission peak at 480 nm, and increased emission lifetime from 0.089 to 0.110 ms, compared to **In@80** in the absence of DMF solvent (Figure 27). [146] This example indicated that the solvent molecule could prolong the fluorescence lifetime of MOFs, which offer a new direction to understand how the solvent polarity, the position in the channel and the size all affect the emission behaviour in the solid-state.

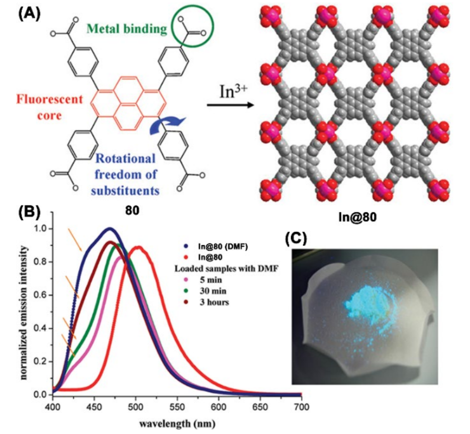

Fig. 27 (A) The molecular structure of the pyrene-based MOF **In@80** from the pro-ligand **80**; (B) Emission spectra of **In@80** (red line) and the exposure of **In@80** to DMF (**In@80 (DMF)**) for 5 min, 30 min and 3 h, respectively. © Photograph of sample of **In@80(DMF)** under UV irradiation. Reproduced from Copyright (2021) (2022)& American Chemical Society.[146]

Stang *et al.* reported a heteroligation-directed three-component coordination-driven self-assembly strategy to synthesize a pyrene-based discrete organoplatinum(II) double-metallacycle **Pt@82** by a one-pot synthesis using pro-ligand **82**, dicarboxylate pro-ligand, and phosphine-capped 90° Pt(II) acceptor in a molar ratio of 1:2:4 in a mixture of acetone and water (Figure 28A). Although pro-ligand **82** is insoluble in acetone, the final complex shows good solubility under the same conditions. The single-crystal X-ray diffraction analysis revealed that the complex shows a 3D supramolecular framework via hydrogen-bonding interactions. It is interesting that pro-ligand **82** show a fluorescence quenching behaviour in the polar solvent nitromethane, but the pyrene-based complex **Pt@82** has a bright blue emission with the maximum emission peak at 431 nm in DMSO solvent (Figures 28B-D). Moreover, the pyrene-based complex **Pt@82** show an enhanced emission with a maximum emission peak at *ca.* 475 nm in the solid state compared to pro-ligand **82**, and maybe the π−π stacking of pyrene has been suppressed. [147]

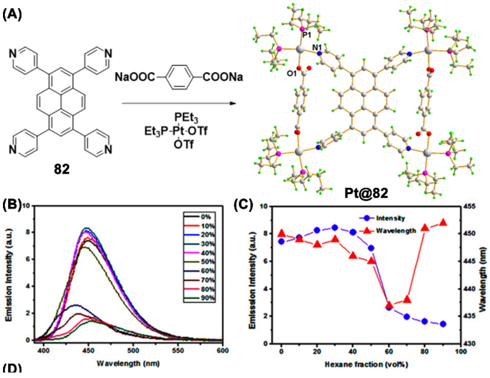

Fig. 28 (A) Molecular structure of the pyrene-based MOF **Pt@82**; (B) Emission spectra of **Pt@82** and (C) plot of relative emission intensity (I/I0) *versus* the composition of an acetone/hexane mixture; (D) fluorescence photograph of **Pt@82** in different acetone/hexane mixtures. Reproduced from Copyright (2021) (2022) & American Chemical Society. [147]

Pyrene-based MOFs with electrical conductivity

Generally, most MOFs are electrical insulators with a conductivity lower than 10^{-10} S cm, [148] Recently, researchers have observed some special MOF architectures and properties including not only novel topology structures but also that they exhibit high charge mobility and/or electrical conductivity [149] which have potential application in energy storage, [150] and electrocatalysis. [151] Thus, the development of electrically active MOFs is an important branch of this research field, and many types of conductive MOFs have been explored. [152] [153]

Electrical conductivity is a key parameter for evaluating the electrical properties of MOFs, Dincă *et al*. summarized the basic approaches (involving through-bond pathways, extended conjugation, through-space pathways, and redox hopping) to achieving electrical conductivity in MOFs. [154, 155] For example, Hupp, Farha and coworkers reported a thermally stable, Zr-based MOF (NU-1000) via solvothermal reaction of $ZrCl_4$, proligand **80** and benzoic acid in *N*,*N*-diethylformamide by an atomic layer deposition synthetic technique. [156] Given the size of nickel bis(dicarbollide) (NiCB) is match well with the triangular channels of the Zr-based MOF (**NU-1000**), and the LUMO energy of NiCB is located between the conduction bands and valence bands of the pro-ligand **80** and NU-1000. When the electron-deficient NiCB as a guest molecule was embedded into the mesoporous NU-1000, the insulated Zr-based MOF **NiCB@NU-1000** can convert it to an electrically conductive system with a conductivity of 2.7×10^{-7} S/cm. Moreover, when manganese oxide (MnO_2) (**Mn-AIM-NiCB@NU-1000**) was deposited in the complex, the installed manganese oxide exhibits a specific capacitance of 276 F/g_{MnO2} at a charge-discharge current density of 0.02 mA cm^{-2}, which suggests there is potential for various electrochemical applications (Figure 29 A and 29B). [157]

Sumby *et al*. [158] reported a 3D stable non-interpenetrated pyrene-based MOF via a π-rich photoactive organic component **80** coordinated with s-block-metals (alkali metals sodium or potassium ion) (Figures 29 C and 29D). Both complexes show a high molar density of 1.62 mol dm^{-3} for **Na@80**, and 1.40 mol dm^{-3} for **K@80**. Both complexes also show a broad absorption band from 225 to 450 nm in the solid state, which also exhibits an intense fluorescence (515 nm for complex **K@80**, and 490 nm for **Na@80**) compared to the pro-ligand **80**. Quantum-chemical calculation results reveal that both complexes show two orders of magnitude hole-transfer rate constants (5.7×10^{12} s^{-1} for **Na@80)**, and 1.5×10^{12} s^{-1} for **K@80**) compared to NU-1000 (3.3×10^{10} s^{-1}) (Table 1) [159], indicating that the π-rich, pyrene-based MOFs are good in terms of electronic activity. The position and orientation of the ligand plays a significant role to affect the electronic coupling and hole-transfer rate constant, and the close packing can improve the hole-transfer rate constants.

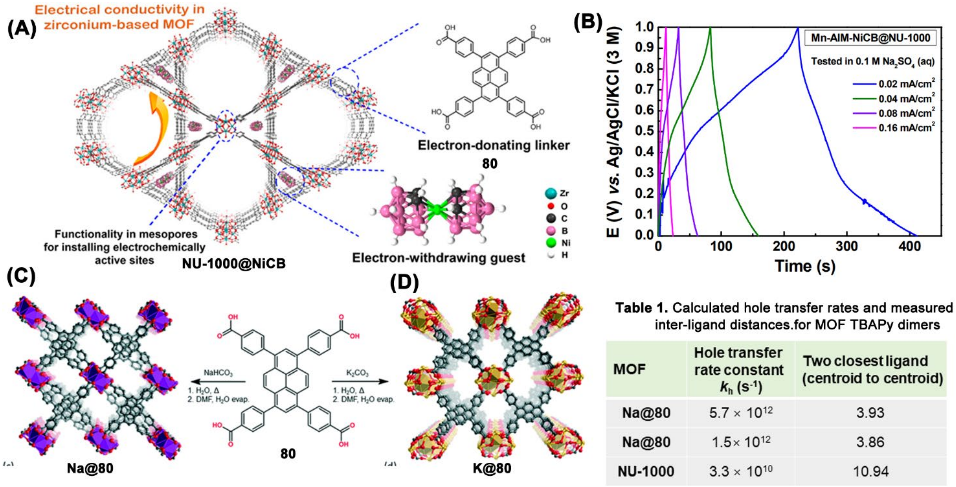

Table 1. Calculated hole transfer rates and measured inter-ligand distances.for MOF TBAPy dimers

MOF	Hole transfer rate constant k_h (s^{-1})	Two closest ligand (centroid to centroid)
Na@80	5.7×10^{12}	3.93
Na@80	1.5×10^{12}	3.86
NU-1000	3.3×10^{10}	10.94

Fig. 29 (A) Molecular structure of the pyrene-based **NU-1000,** (B) Charge-discharge curves of the **Mn-AIM-NiCB@NU-1000** thin film, measured at various charge-discharge current densities. Reproduced from Copyright (2018) & American Chemical Society. [157] Molecular structure of the pyrene-based (C) **Na@80** and (D) **K@80.** Reproduced from Copyright (2018) Royal Society of Chemistry. [158]

Pyrene-based MOFs with light harvesting

On the other hand, pyrene-based MOFs with high-capacity mesoporous channels can act as highly efficient containers for gas storage, and drug delivery. [160] Thus, Ruan *et al*. reported an anionic-ligand-installed pyrene-based MOF for the fluorescence detection of paraquat with a nM-scale detection limit. The presence of the anionic ligands plays a significant role to improve the sensing performance by electrostatic interactions. [161] Moreover, when the chromophore was encapsulated into the mesoporous channels of pyrene-based MOFs via an ion exchange process, the new complex displays a colour-tuneable emission. Yan *et al*. developed a block crystal anionic cluster-based MOF via the ionothermal synthesis between the pro-ligand **80** and [HOEtMIm]Cl. The pyrene-based MOF (**Mn@80**) exhibited a blue emission with a maximum emission peak at 475 nm,

Commented [CR1]: This all should be at the bottom left of the page under the diagram.

which is blue-shifted by 74 nm compared to the pro-ligand **80**. This is attributed to the synergistic effect of the strong electron withdrawing Mn^{2+} cations and the spatial isolation effect. The fluorescence lifetime of **Mn@80** (3.43 nm) is longer than the pure pro-ligand **80** (1.51 ns) in the solid state. Moreover, when the anionic type pyrene-based MOF **Mn@80** was encapsulated in the D-π-A cation dye cyanine (DMP), the crystal colour of the new MOFs **Mn@80@DMP** was changed from pale yellow to red, and the emission was red-shifted to 602 nm with a longer fluorescence lifetime up to 7.38 nm, due to the Förster resonance energy transfer (Figure 30). In addition, the pyrene-based MOF **Mn@80@DMP** exhibited a distinct light absorption from the UV/visible to the NIR region, which generates a maximum photocurrent of 608 nA cm^{-2} under a 403 nm monochromatic light irradiation. This example offers a great opportunity to develop novel pyrene-based MOFs for potential applications in light harvesting and photoelectric conversion.[162]

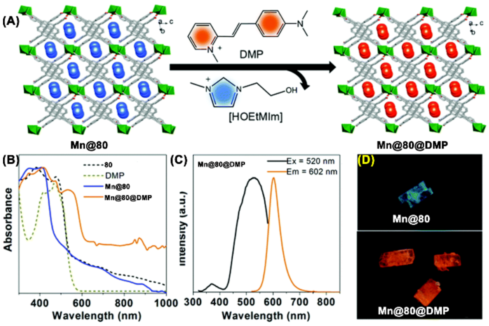

Fig. 30 (A) Schematic diagram of the pyrene-based MOFs **Mn@80** and **Mn@80@DMP** via the ion exchange experiment by the incorporation of DMP cations; (B) UV-vis-NIR absorption of pro-ligand TBAPy, DMP, **Mn@80** and **Mn@80@DMP;** (C) Emission spectra of **Mn@80@DMP** and (D) the fluorescence photograph of **Mn@80** and **Mn@80@DMP** under UV irradiation. Reproduced from Copyright (2020) Royal Society of Chemistry [162]

Pyrene-based COFs

Since Yaghi and co-workers reported the first example of covalent organic frameworks (COFs) in 2005, [163] they have become an attractive class of emerging multifunctional porous materials, due to their structural regularity, permanently porous, large surface area, outstanding stability, and low-density, etc.[164, 165, 166] COFs are composed of lightweight elements (such as C, N, H, Si, B etc.) and connected by covalent bonds with two-dimensional (2D) or three-dimensional (3D) topological structures. [167] Up to now, the diversity of ligand linkage has enriched the *CURATED-COFs* database, [168 169]

Pyrene prefers to form an excimer, resulting in an energy loss process. However, the fluorescent properties of pyrene-based COFs can be regulated by the linkage types with geometric configuration (such as bulky stereoscopic groups, twist conformation groups, as well as the length of linkages, etc) to suppress the ACQ effect in the aggregation state. Since Jiang *et al.* first reported luminescent pyrene-based COFs via the self-assembly of 2,7-pyrenediboronic acid **83** in 2009, [170] pyrene-based COFs have gradually become an important member of the COF family. Many efficient synthetic methodologies for novel pyrene-based COFs have been reported. The typical pyrene-based building blocks are 1,3,6,8-tetrakis(4-formylphenyl) pyrene (**84**) and 1,3,6,8-tetrakis(4-aminophenyl)pyrene (**85**) with 2D or 3D linkages for designing and constructing 2D or 3D pyrene-based COFs. Based on the excellent fluorescence of the pyrene units and the tuneable functional linkages, novel pyrene-based COFs with fantastic optoelectronic properties in the aggregation state are accelerating the development of these crystalline porous materials, and driving different application scenarios, such as photocatalysis, [171] chemical detection,[167] lithium–sulfur batteries,[172] solvent separation,[173] biomedical, [174] explosive detection [175] etc.

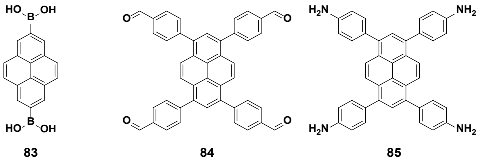

Fig. 31 Typical pyrene-based pro-ligands **83**-**85** for constructing pyrene-based COFs.

A multi-component synthetic strategy is widely used to prepare copolymers, [176] which provides an optional strategy to endow new molecular structures with chemical and physical properties beyond themselves. Gu *et al.* [177] developed a one-pot multi-component COF synthesis involving the pro-ligand **84**, acetaldehyde, and 2,2'-(1,4-phenylene)-diacetonitrile, to achieve a crystalline and porous, containing buta-1,3-diene linkage COF architecture **Py-Bde-COF**, which exhibits a temperature-dependent fluorescence behaviour. The intensity of the photoluminescence decreased monotonically as the temperature increased (Figure 32). Compared to most multi-component syntheses of COFs, [178 179] this synthetic strategy increased the diverse choice of linkers and simplified the synthetic process, which open up a new route for preparing and functionalizing COFs for various applications.

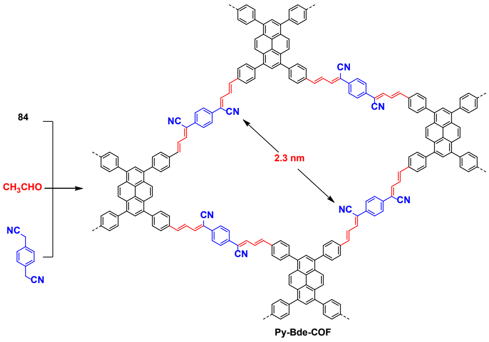

Fig. 32 Multi-component synthesis of the pyrene-based COF (**Py-Bde-COF**). Reproduced from Copyright (2022) & American Chemical Society. [177]

Bein *et al.* reported three highly crystalline quaterthiophene-linked 2D pyrene-based COFs with tuneable electronic properties via the incorporation of the pro-ligand **85** and molecular semiconductors (quaterthiophene (4T), 4H-thieno[3,4-c]pyrrole-4,6(5H)-dione (TPD) or thieno[3,4-b]thiophene (TT)) into COFs, where the pyrene acts an electron-donating group and the quaterthiophene unit acts as an electron-withdrawing group. The three donor-acceptor type pyrene-based COFs emitted a red colour with maximum emission peaks in the range from 654 to 773 nm, respectively. The time-correlated single photon counting traces indicated fast and efficient formation of a charge transfer state between the imine-linked pyrene and the quaterthiophene subunits. [180]

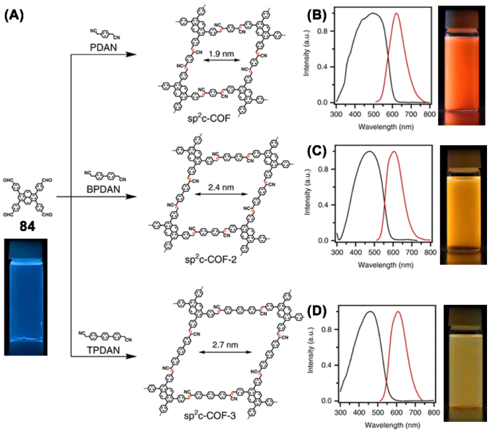

Fig. 33 (A) Syntheses of **sp^{2}c-COF 1-3** via a condensation reaction; (B)-(D) UV-vis and emission spectra of (B) **sp^{2}c-COF 1,** (C) **sp^{2}c-COF 2,** and (C) **sp^{2}c-COF 3** in the solid state, insert: Fluorescence photograph of the corresponding pyrene-based **sp^{2}c-COF 1-3** under UV irradiation. Reproduced from Copyright (2018) & Nature Publishing Group. [181]

When the pyrene-based building blocks bear linkages with a twisted conformation, the pyrene-based COFs show a bright emission. Jiang *et al.* [181] presented three new 2D layered pyrene-based sp^2 carbon-conjugated COFs (**sp^2-c-COF 1-3**) (Figure 33A), where the pyrene moieties and arylyenevinylene linkers were connected via a C=C linkage. The result was a large π-conjugated 2D layered framework along both the x and y directions. As the length of the linkages increased, the porous size of COFs increased from 1.90 to 2.69 nm for the pyrene-based **sp^2-c-COF 1-3**. Moreover, the three COFs exhibit stable (over one year) high fluorescence (QY: 14~21%) in the thin film (Figures 33B-D). When the pyrene-based building block **85** was linked with tetraphenylethene (TPE) using amine units as linkages, the 2D pyrene-based COFs show a maximum emission at 474 nm with improved QY of 21% The QY is larger than most reported imine-based COFs. [182] Thus, this molecular design strategy is devoted to developing high-efficient luminescent pyrene-based COFs in the aggregated state. [183]

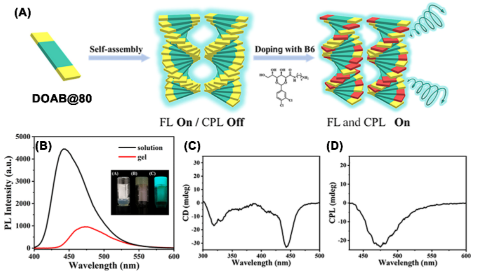

Fig. 34 (A) Schematic representation of the self-assembly process of the pyrene-based COF **DOAB@80** and co-gel chirality induced by B6 and the CPL signal; (B) Emission spectra of **DOAB@80** in EtOH (2.0 × 10^{-5} mol L^{-1}) and the gel phase; (C) CD spectrum and (D) CPL spectrum of the co-gel of **DOAB@80** and B6. Reproduced from Copyright (2022) & American Chemical Society.[184]

Ren *et al*. reported a novel tetraphenylpyrene COF **DOAB@80** via the ionic self-assembly strategy between pro-ligand **80** and dimethyldi-*n*-octadecylammonium bromide (DOAB) (Figure 34A), which exhibits a high fluorescence quantum yield both in solution (87%) and in the solid-state (69%). Moreover, the self-assembled COF can gel in toluene and *o*-xylene solution with a helical supramolecular structure, but not in other solvents, such as hexane, cyclohexane, ethyl acetate, and dichloromethane. Although the pyrene-based COF **DOAB@80** is achiral, it was self-assembled to a co-gel with chiral molecule B6 in toluene solution. The co-gel exhibits an induced CD signal at 335 and 440 nm, which corresponds to the absorption peak of compound **DOAB@80** in the self-assembled system. The co-gel shows strong CPL signals at *ca*. 475 nm with a luminescence dissymmetry factor (glum) of 3.2×10^{-3} (Figure 33B-D). [184]

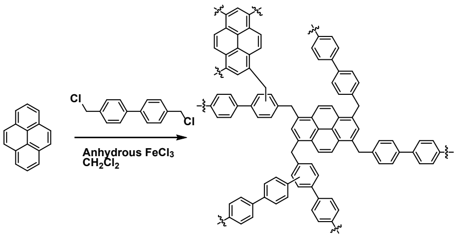

86

Fig. 35 Synthetic route for the preparation of pyrene-based COF **86** via a one-step Friedel−Crafts alkylation reaction.

Babujohn *et al.* reported a one-step facile Friedel−Crafts alkylation reaction between pyrene and bis(1,4-dichloromethyl)biphenyl to hypercross-linked polymer **86** in high yield (>90%), using ferric chloride as a Lewis acid catalyst (Figure 35). The polymer **86** displayed multiple micro- and mesopores in the polymeric network with surface areas of 296, 264, and 698 m^2/g, respectively, which exhibited a high adsorption capacity to a variety of toxic organic pollutants (such as naphthalene, dichlorodiphenyldichloroethylene, carbamazepine, and bisphenol A).[185] This example offers the prospect of application for wastewater treatment and pollutant removal.

Pyrene-based HOFs with electrochemiluminescence

As for COFs, hydrogen-bonded organic frameworks (HOFs) are a class of porous crystalline material self-assembled by hydrogen-bonding interactions between organic building blocks. [186] Due to the presence of weak interactions (π-π, van der Waals, and/or C-H···π interactions), the metal-free nature of HOFs displays more flexible and reversible structures with great biocompatibility and low biotoxicity. [187] Due to the HOFs system being connected by weak interactions, especially hydrogen-bond interactions, some special pro-ligands, such as 1,3,6,8-tetra(4′-carboxylphenyl)pyrene (**80**) and its homologue, 1,3,6,8-tetra(6-carboxynaphthalen-2-yl)pyrene (**87**) and pyrene-1,3,6,8-tetrasulfonic acid (**88**) are preferred for constructing pyrene-based HOF architectures (Figure 36).

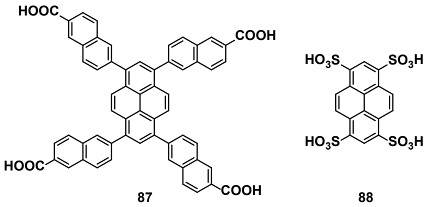

87 **88**

Fig. 36. Pro-ligand structures of **87** and **88** used to form HOFs.

Using pro-ligand **80** as a building block, Xiao *et al*. [141] synthesized the new pyrene-based HOF (**Py-HOF**) with AIE features via a number of hydrogen bonds, which exhibits superb and stable electrochemiluminescence (ECL) intensity. The presence of the strong O-H···O hydrogen bonds suppresses the intramolecular movement and lowers the nonradiative transition in the aggregation state. The ligand **80** in the **Py-HOF** architecture adopted a slipped face-to-face *J*-aggregate packing, which is beneficial to enhancing the ECL emission. Compared to the low-porosity **Py-HOF-210ºC** and **Py-HOF-180ºC**, the higher porosity of **Py-HOF** results in more intensified ECL emission (Figure 37). Thus, the **Py-HOF** can be an "on-off" ECL probe for the hypersensitive detection of miRNA-141.

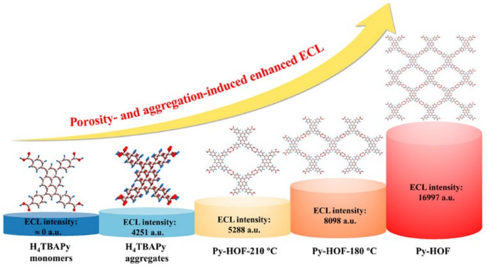

Fig. 37. The ECL intensities were enhanced from 0 a.u. to 16997 a.u. as the porosity were increased from pro-ligand **80** to **Py-HOF.** Reproduced from Copyright (2022) & American Chemical Society. [141]

Pyrene-based luminescence materials with high exciton utilization in OLEDs

Due to the excellent fluorescence of pyrene, pyrene-based compounds are preferred candidates for organic light-emitting diodes. Müllen *et al*. summarized many types of pyrene-based materials for organic electronics in 2011. [23] In this section, we prefer to present typical eye-catching research work on pyrene-based luminescence materials for OLED applications, including new pyrene-based luminescence materials with hot exciton mechanism, AIE characteristics, or thermally activated delayed fluorescence properties.

Azaacene, containing electronegative N atoms, show a high air/thermal stability with relatively low HOMO and LUMO energy levels, as well as highly electron affinity. Generally, azaacene compounds are utilized in OFET and organic/perovskite solar cells (OSCs and PSCs) as charge carrier transport materials, due to their large π-conjugated planar backbone, resulting in carrier mobility. However, azaacene is not often employed in OLED devices due to the ACQ effect. Pyrene-fused pyrazaacenes involve pyrene units and electron-withdrawing pyrazine rings, and have a large aromatic π-sextet, and higher air/thermal stability. Currently, many group found that the pyrene-fused pyrazaacenes containing -CN groups could lower the energy level of S_1 state and reduce the ΔE_{ST} between S_1 and T_1 state. Thus, the pyrene-fused pyrazaacenes provide a possibility of using triplet exciton for improve the exciton utilization efficiency (EUE).

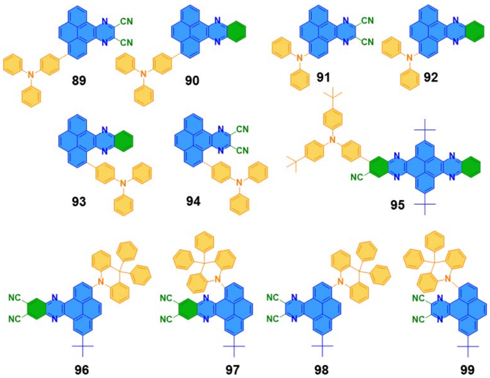

Fig. 38 Molecular structure of the pyrene-based red emitters **89-99.**

For example, Lu *et al*. reported a set of pyrene-based red emitters by decorating electron-donor triphenylamine (TPA) groups at the pyrene core (Figure 40). Due to the isomeric effect, the compounds **89**, and *trans*-**90** with a *trans*-conformation show a higher fluorescence quantum yield (87% and 81%) than the *cis* compounds **94** (19%) and **93** (12%), attributed to the *trans*-configuration effectively hindering the energy loss via nonradiative decay paths. Moreover, the compound *trans*-**91** exhibits a large, red-shifted emission up to 715 nm in the thin film, due to the stronger pull-push electronic structure. Interestingly, the red emitters **8**9, *cis*-**94,** and *trans*-**91** show relatively small ΔE_{ST} (< 0.11), resulting in an efficient reverse intersystem crossing to improve the utilization of the triplet excitons, which display typical TADF characteristics. Indeed, the TADF-OLED based on the red emitter *trans*-**89** realizes the state-of-the-art device performance with a high EQE of 15.5% and an electroluminescent peak of 668 nm in the deep-red region; CIE coordinates of (0.66, 0.35). **[188]**

Wang and co-worker [189] synthesized a set of pyrene-fused pyrazaacenes with a red TADF emitter for OLED applications. To achieve a high-efficiency TADF emitter, the position of the substituent (9,9-diphenyl-9,10-dihydroacridine, DPAC) on the pyrene core and the expanding π-conjugated of molecular backbone were tuned by molecular engineering, and the compounds of *trans*-isomers **96** and **98** show a higher photoluminescence quantum yield up to 78%~89%, compared to the *cis*-isomers **97** and **99**. Thus, the **96** and **98** based TADF-OLED devices show a higher EL efficiency and low turn-on voltage with $\lambda_{em\ max}$ of 596 nm and 640 nm, and EQE of 14.07% and 23.95% compared to **97** and **99**; the EQE are 3.28% for **97** and 2.42% **99**, respectively. The CE_{max} and PE_{max} are 51.17 cd A^{-1} and 53.58 lm W^{-1} for **96**, and 24.44 cd A^{-1} and 22.48 lm W^{-1} for **98**, respectively. In contrast, **97** and **99** show a relatively poor EL performances with CE_{max} of 2.15 and 0.84 cd A^{-1}. The transient PL delay spectra indicated that the compounds **96** and **98** possess efficient TADF characteristics involving intersystem crossing (ISC) and RISC processes ($S_1 \rightarrow T_1 \rightarrow S_1 \rightarrow S_0$), resulting in a highly EUE of triplet exciton in T_1 state.

Furthermore, Fan, Ma and co-workers [190] reported a pyrene-fused pyrazaacenes **95** via integrating the strong electron-donating group TPA and the electron-accepting cyano group, which was used as a red fluorophore and applied in a doped-OLED device with excellent electroluminescence properties. The compound exhibits a $\lambda_{em\ max}$ at 604 with high PLQY of 94.6% in the solid state. The calculated ΔE_{ST} between the S_1 and T_1 state is as low as 0.12 eV. The compound **95** based red OLED device exhibits the highest EQEs of 41.30% at 610 nm, indicated that this compound can maximize the harvest of singlet and triplet excitons via the RISC process, resulting in a high EQE. The turn-on voltage decreased from 2.45 V to 2.0 V as the doping ratio increased from 3 wt% to 12 wt%, indicative of the great charge carrier transport properties. Thus, the development of novel pyrene-fused pyrazaacenes with TADF properties provides a possibility to improve the EUE for organic optoelectronic devices via a molecular design strategy.

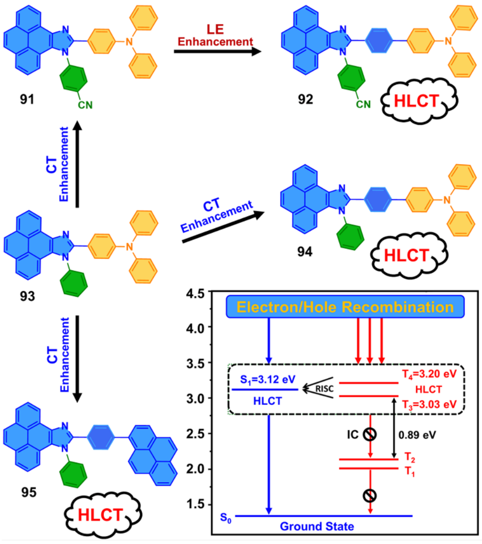

Fig. 39 Molecular structure of the pyrene-based Imidazole compounds 91-95 and possible model of exciton relaxation in the EL process of **95** with the NTOs for S_1, T_3, and T_4.

According to the calculation (**Scheme 2**), the relatively low ΔE_{ST} between the S_1 and T_2 states can contribute to improve the exciton utilization via a RSIC process. Up to now, some novel high exciton utilization pyrene-based luminescent materials have been explored.

Imidazole and its derivatives display intensive blue fluorescence with different excited states of local excited (LE), hybridized local and charge-transfer (HLCT), and charge transfer (CT), depending on the terminal substituents present. [191] For example, according to theoretical calculations, the expanding π-conjugation can contribute to modulating the excited state from LE/CT to HLCT from compound **102** to **100**. The highly mixed excited state of LE and CT for compounds **103** and **101** is beneficial for enhancing the fluorescent performance and high radiative exciton ratio. Thus, the non-doped OLED devices with **103** and **101** as the emitters exhibit excellent electroluminescence with a maximum CE of 9.16 and 8.74 cd A^{-1}, respectively, maximum EQE of 8.47% and 7.52%, respectively, maximum brightness of 30344 and 50046 cd m^{-2}, respectively, and a nearly 100% exciton utilization. [192] Moreover, a high-performance hybrid white OLED was fabricated using **101** as a blue-emitting component with the maximum EQE, PE, and CE of 21.19%, 61.46 lm W^{-1}, and 62.13 cd A^{-1}, respectively (Figure 39).

When the TPA unit was replaced by a pyrene unit, the pyrene-based weak electronic donor-acceptor molecule, 9-phenyl-10-(4-(pyren-1-yl)phenyl)-9H-pyreno[4,5-d]imidazole (**104**) (Figure 39A), emits blue emission ($\lambda_{max\ em}$ = 462 nm) in thin film with a quantum yield of 0.52. Moreover, the HLCT-dominant molecule **104** shows an improvement of the EUE efficiency of 55% in the non-doped OLED, and the corresponding OLED exhibits excellent performance with a maximum brightness of 75,687 cd m^{-2}, a maximum current efficiency of 13.38 cd A^{-1}, and a maximum external quantum efficiency (η_{ext}) of 8.52%. Generally, the theoretical EQE of a fluorescent OLED is less than 5%, but the pyrene-based imidazole derivatives display excellent OLED properties with larger EQE of up to 5%. The triplet exciton has been utilized for improving the EQE value. The S_1-T_1 energy gap was evaluated by experiment with a value of 0.95 eV, and NTO analysis indicated that the energy gap between T_4 and T_3 and S_1 is small, which is beneficial to a fast RSIC process from $T_4 \rightarrow S_1$ and $T_3 \rightarrow S_1$ transition, however the $T_n \rightarrow T_1$ is forbidden (Figure 39B). The exciton relaxation in the EL process is in accordance with the "hot mechanism". [193]

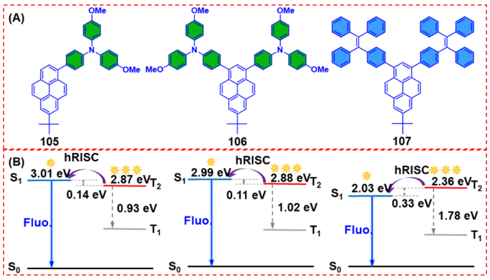

Fig. 40 Molecular structure of the Y-shaped pyrene-based blue emitters **105-107,** and the corresponding schematic diagram of the energy-transfer process calculated at the M062X/6-31G(d, p) level. Reproduced from the author.

More recently, our group presented two pyrene-based blue emitters **105** and **107** with AIE characteristics, which showed excellent blue EL properties both in non-doped or doped OLED devices (Figure 41A). The blue emitter **106** is an ACQ molecule.[194] The L_{max} luminescence, η_{ext}, η_c, and η_p of the doped-OLED devices are 10290 cd m^{-2}, 6.11%, 12.28 cd A^{-1}, and 12.86 lm W^{-1} for **105**, and 6651 cd m^{-2}, 7.27%, 12.65 cd A^{-1}, and 12.42 lm W^{-1} for **107** in the optimized OLED configurations, respectively. While in the non-doped OLED devices, the **107** displays higher EL properties with L_{max} η_{ext}, η_c, and η_p of 23162 cd $m^{-2,}$ 4.90%, 11.23 cd A^{-1} and 9.67 lm W^{-1}, respectively. The EQE of these fluorescent OLED devices can be explained by the "hot exciton" mechanism, where the triplet excitons at T_2 was transferred to the lowest single excited (S_1) state *via* a reverse intersystem crossing (RISC) process, leading to a high exciton utilization efficiency (η_r) up to (77.3%) (Figure 41B). This example presents a new basis for designing pyrene-based "hot exciton" AIEgens to achieve high-performance OLED.

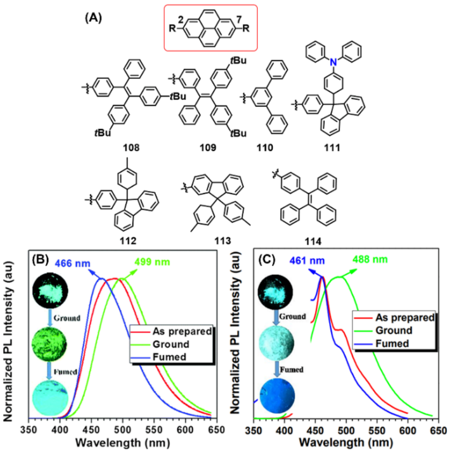

Fig. 41 Molecular structure of the linear-shaped 2,7-disubstituted pyrene-based blue emitters **105-111.** Reproduced from Copyright (2018) Royal Society of Chemistry. [195]

Interestingly, when pyrene was combined with the TPE unit, which was decorated at the active sites of the 1-, 3-, 6- and 8-positions, the K-region of the 4-, 5-, 9- and 10-positions, or the node plane of the 2- and 7-positions, the prepared compounds display a tunable-emission with intriguing aggregation-induced emission characteristics. [95, 196] [197] Li *et al.* [195] synthesized a set of linear-shaped 2,7-substituted pyrenes (**108-111**) with AIE characteristics *via* the introduction of different aromatic substituent groups (Figure 42A). Due to the effect of the substituents, the compounds **108** and **109** with TPE units exhibited mechanochromism effects with a large, red-shifted emission up to 33 nm under external force stimulus (Figure 42B-C). Moreover, all compounds were utilized as emitting layers for fabricated non-doped OLED devices with excellent EL properties. The presence ofthe triphenylamine units is beneficial to improve the hole-injection ability and enhance the power efficiency. The compound **111** exhibited the lowest turn-on voltage at 3.1 V. The EL emission was finely tuned via changing the substituents, the length of π-conjugation and the mode of linkage, and the emission changed from sky blue (484 nm) for **108** to deep blue (444 nm) for **111,** following the order of $\lambda_{EL\ max}$: **105** > **109** >**112** > **113** > **110** > **111**. More importantly, **110** revealed the best device performance with an $\eta_{EQE,max}$ up to 3.46% at a CIE coordinate of (0.15, 0.09). Similarly, Tang[198] *et al* reported a TPE unit substituted at the 2,7-positions of pyrene **114**, which exhibits a blue-shifted emission at 462 nm with a higher quantum yield of 0.62 in thin film. This was applied in a non-doped OLED with a maximum luminance of 15750 cd m^{-2}, a current efficiency of 7.34 cd A^{-1}, a power efficiency of 6.40 lm W^{-1} and an external quantum efficiency of 3.19%. Moreover, this high-performance OLED device exhibits a low turn-on voltage, improvement of the luminance, external quantum efficiencies and low roll-off efficiency, indicated that the pyrene-based AIEgens show extreme advantages in high efficiency blue devices. [198]

Since the new pyrene-based chemical intermediate 2-*tert*-butyl-1,3,5,9-tetrabromopyrene **10** was reported by Feng and Yamato in 2013, [199] [200] many new butterfly-shaped 1,3,5,9-substituted pyrenes [201] have been synthesized from this new intermediate **10**. According to the literature, the 1,3,5,9-substituted pyrenes display distinctive advantages, such as good thermal stability, high (deep) blue (even violet) fluorescence with high fluorescence quantum yield, a small, red-shifted emission in the solid state compared to in solution, and are excellent candidates for constructing high-performance (deep) blue OLED devices. For example, compounds **115**[199, 201] emitted deep blue emission (< 443 nm) with high quantum yield (> 0.72) both in solution and in the thin film. Further, Feng, Yamato *et al*. reported a controllable regioselective strategy for the asymmetric functionalization of pyrene at the 1,3- and 5,9-positions, [202] and a new intermediate 1,3-diphenyl-5,9-dibromopyrene was prepared for constructing dipolar molecules. For example, 1,3-diphenyl-5,9-diarylethynyl)pyrenes **116**, which exhibits a colour-tuneable emission from pure blue (474 nm) to orange-red (566 nm) in the solid state via changing the substituents at the 5,9-positions. Moreover, due to the unbalanced electronic distribution of these asymmetrically substituted dipolar molecules, this set of compounds **116** exhibit a clear solvatochromism effect. In particular, compound **116f** shows distinct emission colour changes from deep blue, to green, yellow, or even orange-red, as the solvent polarity increases from cyclohexane to DMF.

Based on the new intermediate, Hu *et al*. reported a set of asymmetric 1,3- and 5,9-aryl substituted pyrene-based emitters with weak electron-acceptor characteristics, via the introduction of suitable substituents at the 5,9-positions. Compound **117** exhibits a strong near ultraviolet (NUV) emission (<434 nm) with considerable quantum yield both in solution and in the solid state, which was utilized for the preparation of NUV OLED devices. Especially, the CBP-based doped OLED with the CBP host exhibits NUV light emission CIEy < 0.05. Moreover, compound **117b** reveals an EL performance with EQE, CE, and PE values of 2.97%, 1.25 cd A^{-1}, and 1.31 lm W^{-1}, respectively. This example was the first demonstration of high-efficiency NUV OLED devices using pyrene-based luminescence materials. [203] When the 5,9-positions were substituted by larger π-conjugated polycyclic aromatic hydrocarbons units, such as naphthyl, phenanthryl, anthryl groups, the series of 1,3-phenyl- 5,9-diaromatic substituted pyrene derivatives **118** still displayed colour-tuneable emission from violet-blue (409 nm, **115a**) to pure-blue (465 nm, Py-**118d**) depending on the extent of the expanding π-conjugation of the substituents at the 5,9-positions. Based on these compounds, the non-doped OLEDs show a relatively low turn-voltage (V_{on}) of about 3.0 V, with (deep) blue EL peak at 429 nm (**115a**), 436 nm (**118a**), 448 nm (**118b**) and 459 nm (**118c**) with highly EQE (> 2.92 %) respectively. Especially, the emitter **118c** based OLED exhibited the best EL performance with EQE, CE, and PE values of 5.73%, 6.42 cd A^{-1}, and 4.69 lm W^{-1}, respectively. [204] The maximum EQE of up to 5.73% for **118c** based fluorescent OLED is over the limitation of 5% for conventional fluorescent OLEDs and is ascribed to the high utilization of the triplet (T_1) presumably via the triplet-triplet annihilation (TTA) process.

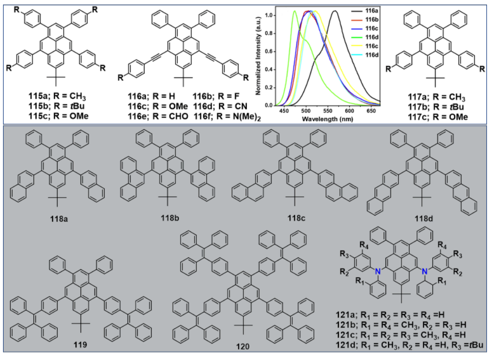

Fig. 42 Molecular structures of the 1,3,5,9-substituted pyrene-based blue emitters **112**-**118**. (A) Emission spectra of compound **113** in the solid state, Reproduced from Copyright (2018) Elsevier Ltd. [202] (B) Normalized EL spectra of **118** at a luminance of 10 000 cd m^{-2}, and (C) EQE *versus* luminance plots. Reproduced from Copyright (2022) Wiley-VCH Verlag GmbH & Co. KGaA. **[205]**

Moreover, when the TPE units were introduced at the 4,5-positions, the butterfly-shaped pyrene-based compound **119** was found to exhibit a fantastic AIE characteristic emission and the maximum emission peak is at 491 nm and the quantum yield is 0.58 in the thin film. This was utilized as an emitting layer for an OLED device, which exhibited an EL performance with a maximum luminance of 11450 cd m^{-2}, a current efficiency of 6.51 cd A^{-1}, power efficiency of 6.24 lm W^{-1} and external quantum efficiency of 3.35%.[206] Furthermore, the highly twisted pyrene-based AIEgen 2-*tert*-butyl-1,3,5,9-tetra(4-(1,2,2-triphenyl-vinyl)phenyl)pyrene **120** was employed as an emitting layer for OLED devices with excellent electroluminescence properties. Compound **120** exhibits an intensive emission with a maximum emission peak at 467 nm and quantum yield of 0.78 in thin film. The non-doped OLED exhibited an EL emission at 468 nm with high performance (EQE_{max}: 4.10%, CE_{max}: 7.38 cd A^{-1} and PE_{max}: 6.42 lm W^{-1}). [207] Recently, electron-donating substituents derived from diphenylamine were introduced at the 5,9-positions of pyrene. The compounds **121**[205] display ultrahigh luminance and extremely low-efficiency roll-off characteristics with the maximum luminance of 48280, 37490, 37850, and 44 450 cd m^{-2} with considerable EQE_{max} of 4.30%, 4.31%, 4.06%, and 4.25% at a high luminance of ≈ 10000 cd m^{-2} for **121a**-**121d**, respectively. In addition, the high EQE may contribute to the high triplet exciton utilization efficiency (29% for **121a**, 29% for **121b**, 27% for **121c**, and 28% for **121d**) via a triplet–triplet annihilation (TTA) process. [208] Moreover, these compounds exhibit narrow full width at half-maximum (FWHM) of about 50 nm. On the other hand, the optimized device of the representative blue emitter **121a** displays an extremely long LT97 and LT95 (lifetime to 97% or 95% of the initial luminance) of 303 and 534 h at an initial luminance at 1000 cd m^{-2}. Compared to the 1,3,5,9-tetraarylsubstituted pyrenes, using the pyrene-based AIEgens as an emitting layer, where the substituents were located at 1,3- or 1,3,5,9-positions, the (non-) doped OLED showed huge advantages not only in higher EL performance, such as luminance, power efficiency, but also a more stability optoelectronic device, as well as a lower turn-on voltage. Thus, these examples open the door for constructing new pyrene-based luminescent materials with (deep) blue, narrow band emission properties for high-performance electroluminescent devices.

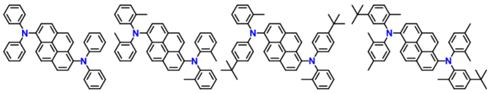

122 123 124 125

Fig. 43 Molecular structures of the 1,6-disubstituted pyrene-based blue emitters **122**-**125**.

On the other hand, when the functionalized diphenylamine moiety was selected as the substituted group introduced at the 1,6-positions of pyrene, the compounds **122**-**125** emit blue emission with high quantum yield both in solution and in the solid state. Each compound when used for a doped OLED showed a high current efficiency (CE) of over 7 cd A^{-1} and a high EQE of over 7.5%. [209] The compound **124** shows the highest CE of 9.97 cd A^{-1}, and the compound **125** exhibits the highest EQE of 9.25% with LT95 lifetime of 471 h, but all of these OLED devices show a large turn-on voltage up to 8.86 V. However, the authors also did not discuss why the EQE of the fluorescent OLED devices more than the theoretical EQE?

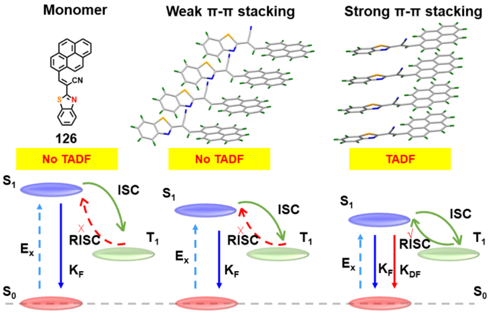

Fig. 44 Molecular structure of the pyrene-based emitters **126** with different crystal packings and schematic of TADF of aggregates induced by strong intermolecular π–π interactions.

More importantly, the molecular packing also affects the electronic transition, leading to TADF properties. Yang *et al*. reported a new AIEgen pyrene-based emitter **126**. The crystalline powder shows an ordered π-π stacking with orange-yellow fluorescence, but the compound **126** could show a red-shifted emission with TADF properties under stimuli, which originated from the strong face-to-face intermolecular π-π stacking, according to the crystal packing. Theoretical calculations indicated that both types with different molecular packing could decrease the singlet energy, but the triplet-state energy almost remained unchanged after grinding, resulting in a lower ΔE_{ST} and fast the RSIC process form the T_1 state to S_1 for TADF emission in aggregates. Thus, this example offers a new perspective to development new non-TADF emitters with TADF properties via strong intermolecular interactions in the aggregate state.

Table 1 EL performance of OLEDs based on pyrene derivatives **175**-**192**.

Device	λ_{EL} (nm)	*V*on (V)[b)]	*L* (cd m^{-2})[a)]	$\eta_{C, max}$ (cd A^{-1})[a)]	$\eta_{P,max}$ (lm W^{-1})[a)]	$\eta_{ext,max}$ (%)[a)]	η_r (%)	CIE (x, y)[c)]
89	668	3.5	2769	10.5	9.46	15.50	-	(0.66, 0.35)
90	544	3.8	4495	16.9	13.95	5.12	-	(0.39, 0.56)
91	640	4.3	1258	11.2	8.21	13.90	-	(0.64, 0.35)
92	560	3.8	2871	20.3	16.77	6.42	-	(0.45, 0.54)
93	536	4.5	469	1.19/-	0.83	0.40	-	(0.39, 0.56)
94	669	5.9	555	0.95/-	0.51	1.56	-	(0.63, 0.36)
95	610	2.45	4272	73.68	101.08	41.3	-	(0.54, 0.46)
96	640	3.0	2026	24.44	22.48	26.26	-	(0.62, 0.37)
97	684	4.4	628	0.84	0.60	3.13	-	(0.67, 0.31)
98	596	3.0	3567	51.17	53.58	22.62	-	(0.54, 0.46)
99	648	4.4	1922	2.15	1.31	3.52	-	(0.66, 0.34)
100	476	3.8	6100	1.90/-	-	1.13	29	(0.16, 0.24)
101	468	3.4	50046	8.74/-	-	7.52	86	(0.15, 0.21)
102	448	3.0	6300	1.58/-	-	1.84	33	(0.15, 0.10)
103	464	2.8	30344	9.16/-	-	8.47	91	(0.14, 0.13)
104	475	3.0	75687	13.38/-	10.75	8.52	82	(0.15,0.22)

105	482	2.9	10290	12.28/ 6.51	12.86	6.11	40.7	(0.16, 0.31)
107a	466	3.1	6651	12.65/ 8.02	12.42	7.27	77.3	(0.18, 0.27)
107b	484	3.1	23162	11.23/ 11.23	9.67	4.90	52.1	(0.22, 0.37)
108	484	4.9	15546	6.91	3.55	3.25		(0.20, 0.29)
109	460	4.3	3514	2.85	1.82	2.19		(0.16, 0.17)
110	448	4.2	18287	2.94	1.79	3.46		(0.15, 0.09)
111	444	3.1	9754	1.72	1.52	2.10		(0.15, 0.08)
112	456	3.9	6081	2.50	1.37	1.37		(0.17, 0.18)
113	452	4.3	1996	2.27	1.37	1.70		(0.16, 0.11)
114	492	3.1	15750	7.34	6.03	3.19		(0.23, 0.39)
117a	422	3.2		1.15	1.13	2.99		(0.15, 0.046)
117b	422	3.4		1.25	1.31	2.97		(0.15, 0.049)
117c	423	3.6		1.24	1.09	2.97		(0.15, 0.043)
119	488	3.2	11450	6.51	6.24	3.35		(0.19, 0.28)
120	468	3.2	11849	7.38	6.42	4.10		(0.17, 0.26)
121a	474	3.7	48280	7.75		4.30	29	(0.132, 0.27)
121b	471	3.9	37490	6.33		4.31	29	(0.131, 0.21)
121c	473	3.7	37850	6.45		4.06	27	(0.134, 0.24)
121d	477	3.8	44450	7.33		4.25	28	(0.137, 0.26)
122	462	8.86		8.72	3.59	8.34		（0.137, 0.142）
123	457	9.59		7.07	2.56	7.57		（0.138, 0.121）
124	466	9.25		9.97	3.75	8.47		(0.128, 0.178)
125	463	9.13		9.67	3.69	9.25		(0.133, 0.145)

Configuration:

Device 1 (**89**): ITO/HATCN (6 nm)/TAPC (45 nm)/TCTA (5 nm)/TPBi (10 wt%): **89** (30 nm)/TmPyPb (40 nm)/LiF (1 nm)/Al (120 nm)
Device 2 (**90**): ITO/HATCN (6 nm)/TAPC (45 nm)/TCTA (5 nm)/ **90** (20 nm)/TmPyPb (40 nm)/LiF (1 nm)/Al (120 nm)
Device 3 (**91**): ITO/HATCN (6 nm)/TAPC (45 nm)/TCTA (5 nm)/TPBi (10 wt%): **91** (30 nm)/TmPyPb (40 nm)/LiF (1 nm)/Al (120 nm)
Device 4 (**92**): ITO/HATCN (6 nm)/TAPC (45 nm)/TCTA (5 nm)/ **92** (20 nm)/TmPyPb (40 nm)/LiF (1 nm)/Al (120 nm)
Device 5 (**93**): ITO/HATCN (6 nm)/TAPC (45 nm)/TCTA (5 nm)/ **93** (20 nm)/TmPyPb (40 nm)/LiF (1 nm)/Al (120 nm)
Device 6 (**94**): ITO/HATCN (6 nm)/TAPC (45 nm)/TCTA (5 nm)/TPBi (10 wt%): **94** (30 nm)/TmPyPb (40 nm)/LiF (1 nm)/Al (120 nm)
Device 7 (**95**): ITO/HAT-CN (10 nm)/TAPC (40 nm)/TCTA (10 nm)/CBP: **95** (3 wt%) (20 nm)/B4PyMPM (55 nm)/Liq (2 nm)/Al (120 nm)
Device 8-11 (**96-99**): ITO/TAPC (40 nm)/mCP (5 nm)/mCBP: **96-99** (10 wt%) (20 nm)/B3PYMPM (50 nm)/LiF (1 nm)/Al (100 nm)
Device 12-15 (**100-103**): ITO/HATCN (5 nm)/TAPC (55 nm)/TCTA (5 nm)/**100-103** (30 nm)/TPBi (40 nm)/LiF (0.5 nm)/Al (100 nm)
Device 16 (**104**): ITO/MoO3 (10 nm)/TAPC (40 nm)/ **104** (25 nm)/TPBi (40 nm)/LiF (0.5 nm)/Al (100 nm)
Device 17 (**105**): ITO/HATCN (5 nm)/TAPC (50 nm)/TCTA (5 nm)/mCP (5 nm)/ **105** (10 wt%): PPF (20 nm)/TmPyPb (30 nm)/LiF (1 nm)/Al
Device 18 (**107**): ITO/HATCN (5 nm)/TAPC (50 nm)/TCTA (5 nm)/mCP (5 nm)/ **107** (10 wt%): PPF (20 nm)/TmPyPb (30 nm)/LiF (1 nm)/Al
Device 19 (**107**): ITO/HATCN (5 nm)/TAPC (50 nm)/TCTA (5 nm)/mCP (5 nm)/ **107** (20 nm)/ PPF (5 nm)/TmPyPb (30 nm)/LiF (1 nm)/Al
Device 20-25 (**108-113**): ITO/PEDOT: PSS/NPB (40 nm)/**108-113** (10-20 nm)/TPBI (35 nm)/Ca: Ag
Device 26 (**114**): ITO/HATCN (5 nm)/TAPC (40 nm)/TCTA (5 nm)/**111** (20 nm)/Bepp2 (45 nm)/Liq (2 nm)/Al
Device 27-29 (**117**): ITO/HATCN (5 nm)/TAPC (40 nm)/CBP: **117** (5 wt%) (20 nm)/B3PyPB (40 nm)/LiF (1 nm)/Al (100 nm)
Device30-31 (**119-120**): ITO/NPB (30 nm)/TCTA (10 nm)/**119-120** (20 nm)/TPBi (40 nm)/LiF (1 nm)/Al (100 nm)
Device 32-35 (**121**): ITO/2-TNATA (30 nm)/NPB (30 nm)/α, β-AND: **121** (4 wt%) (25 nm)/TPBi (30 nm)/LiF (1 nm)/Al (100 nm)
Device 36-39 (**122-125**): ITO/2-TNATA (60 nm)/NPB (20 nm)/α, β-ADN: **122-125** (4 wt%) (35 nm)/Alq3 (15 nm)/LiF (1 nm)/Al (200 nm)

Based on the mentioned-above examples, the development of pyrene-based luminescent materials are remarkable candidates for OLED materials, due to their relative low turn-on voltage, bright solid state emission, and high quantum yield to achieve excellent EL efficiency. Especially, pyrene-based AIEgen emitters are better feasible alternatives for OLED applications with high exciton utilization efficiency (EUE), via a reasonable molecular designing for tuning the $\Delta E_{S1\leftarrow Tn}$ (n≥1) to achieve a hot exciton or TADF materials.

Pyrene-based luminescent materials for OFET

Pyrene-based materials not only exhibit bright emissive behaviour but also are excellent semiconductors for organic optoelectronics. Since Zhu *et al*. first reported 1,3,6,8-tetrakis(2-thiophene)pyrene **127** as a *p*-type semiconductor with 3.7 $\times 10^{-3}$ cm^2 V^{-1} s^{-1} with an on/off ratio of 10^4 in a FET device, [210] many advanced OFET devices using pyrene-based luminescent materials as active materials have been fabricated. [211] Recently, with the further development of preparation technologies, high-performance organic optoelectronics have been reported. Zhang *et al*. reported two isomers, 1,6 and 2,7-*trans*-β-styryl substituted pyrenes **128** and **129**, which were synthesized by a Suzuki-coupling reaction, and which exhibited a considerable quantum yield of 28.8% and 27.4% in the crystallized state, respectively. Notably, compound **129** is an AIE-active molecule, whereas **128** is an ACQ material. Moreover, both compounds display impressive *p*-type semiconducting properties and the hole mobilities increased as the substrate temperature increased from 25 to 50 °C. The compound **129** shows higher hole mobility up to 1.66 V^{-1} s^{-1} with on/off ratio of 10^8 compared to compound **128** (0.15 cm^2 V^{-1} s^{-1}). [212]

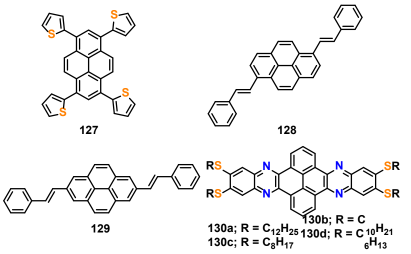

Fig. 45 Molecular structure of the pyrene-based semiconductors emitters **127-130.**

Pyrene shows high electron affinity and charge-carrier mobilities which originates from the large π-conjugated electron system. Moreover, the well-ordered molecular packing with larger π-frameworks can contribute to improving the charge-carrier mobility due to the efficient intermolecular π–π orbital overlap along the stacked conjugated cores. [213] Based on this strategy, Jabbourb *et al.* [65] synthesized four pyrene-based azaacenes **130**, which showed similar LUMO energies of 2.97 eV, Moreover, these compounds display *p*-type characteristics with hole mobility of ~ 10^{-3} cm^2 V^{-1} s^{-1}. Due to the electron-rich molecular structure, pyrene is a good building block for the preparation of *p*-type organic semiconductors with high hole mobility.

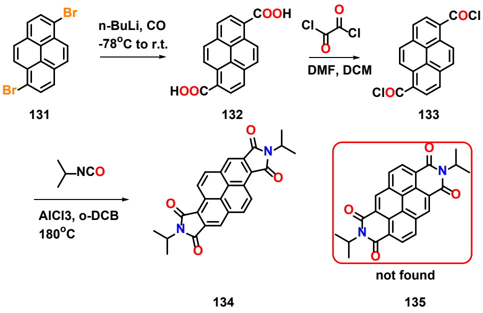

Fig. 46 Synthetic route to the pyrene-based diimide **126**.

On the other hand, the key point in constructing n-type organic semiconductors is developing electron-deficient large π-conjugated frameworks. Fullerene, [214] naphthalene diimide (NDI), [215] perylene diimide (PDI), [216] diketopyrrolopyrrole, [217] and heteroacenes [218] are typical electron-deficient frameworks, which can be utilized as electron-deficient acceptors for OFET and OPV devices. Some of these compounds show high electron mobilities as high as 16 cm^2 V^{-1} s^{-1}. [219] Thus, researchers have devoted time to functionalizing the pyrene to form electron-deficient units by employing molecular design strategies. Pei *et al.* [220] first synthesized a new pyrene-based diimide **134** from 1,6-dibromopyrene **131** by the following synthetic route (Figure 45): (1) 1,6-dibromopyrene **131** was treated with *n*-BuLi and carbon dioxide to give pyrene-1,6-dicarboxylic acid **132**, which subsequently underwent a substitution reaction and a cyclization reaction to afford the 1,2,6,7-substituted pyrene-based diimide **134.** This product contains five-membered imide rings, whilst the pyrene-based diimide **135** with six-membered imide rings was not observed. This maybe reveals a lower energy barrier in the cyclization process when the cyclization occurs at C2 and C7 positions of pyrene. This example offers a strategy to functionalize the pyrene ring at the non-K region for the construction of new *n*-type pyrene-based diimides for organic electronics.

Subsequently, Zhang *et al.* reported a series of 4,5,9,10-substituted pyrene-based diimide derivatives **136** and **137** via functionalizing the K-region of the pyrene core. Compound **136a** exhibits bright fluorescence with a high fluorescence quantum yield of 59.7% in solution, but almost quenched emission in the solid state due to strong intermolecular interactions. For **137a**, the compound with a bulky *tert*-butyl group show a quantum yield of 79.5% in dilute solution (< 10^{-7} M), due to the rigid and planar molecular conformation. Compound **137a** displays a clear excimer emission at 480 nm with a decreased fluorescence quantum yield from 79.5% to 18.3% in the solid state. Interestingly, both compounds display two-photon absorption (TPA) properties with the highest TPA cross-sections of 89.15 GM for **137a** and 40.74 GM for **136a**, respectively. Further, the selected crystals of **136a**, **137a** and **137b** were utilized to fabricate OFET devices using Au as source and drain electrodes. The devices exhibited n-type characteristics with the highest electron transport mobility of 2.51×10^{-4} cm^2 V^{-1} s^{-1}, 0.46 cm^2 V^{-1} s^{-1} and 0.51 cm^2 V^{-1} s^{-1} for **137a**, **136a** and **137b,** respectively. Moreover, when the source and drain electrodes instead employed Ag, the electron transport mobilities improved to 3.08 cm^2 V^{-1} s^{-1} for **136a** and 2.36 cm^2 V^{-1} s^{-1} for **136b**. [221] Thus, these pyrene-based diimide derivatives with good fluorescence properties and electron transport mobilities are excellent candidates for a new perspective on advanced organic electronics.

However, when the large π-frameworks of pyrene-based azaacenes were integrated with strong electron-withdrawing units, excellent n-type organic semiconductors could be produced. Liu *et al.* reported new B←N fused dibenzoazaacenes **138**[222] and **139**[223] which exhibited great stability under ambient conditions from the pyrene-based intermediates 1,3,6,8-tetrabromopyrene-4,5,9,10-tetraone **19** [222] and 7-*tert*-butyl-1,3-dibromopyrene-4,5,9,10-tetraone **18** [224], respectively. The B-containing pyrene-based azaacene **138** possessed low-lying LUMO energy levels and high electron affinities, resulting in fantastic n-type characteristics. Moreover, compound **138** possesses an ultralow LUMO value of −4.58 eV. Furthermore, the OFET devices based on **139** display unipolar n-type behaviour with an electron mobility of 0.21 cm^2 V^{-1} s^{-1} with an on/off current ratio of 105 −106, while in the compound **138**, containing more B←N unit, the OFET shows a higher electron mobility of 1.60 cm^2 V^{-1} s^{-1} with a threshold voltage of 14 V. More importantly, these OFET devices both B←N-containing pyrene-based azaacenes **138** and **139** exhibit excellent ambient stability under air. In addition, the compounds containing the B←N unit exhibit large, red-shifted absorption peaks in the red or near-infrared (NIR) region (686/628 nm for **130**, and 685/712 nm for **129**, respectively) with high molar absorption coefficients ~10^{-5} M^{-1} cm^{-1}. Both examples offer a novel strategy to develop pyrene-based *n*-type organic semiconductors via integrating the B←N unit into the pyrene core for lowing the LUMO energy levels and improving the electron affinities.

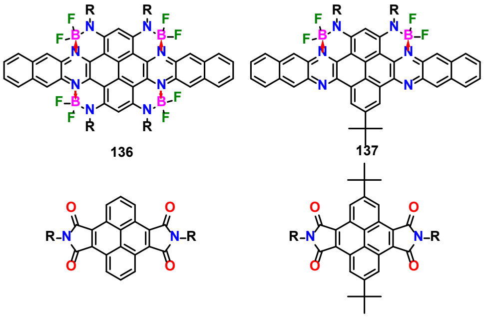

R = n-pentyl R = n-hexyl R = n-heptyl

Fig. 47 High mobilities of pyrene-based pyrene-based diimide **136 a d 137** and B←N fused azaacenes **138** and **139.**

Pyrene-based luminescent (intermediates) materials for energy conversion and storage

The energy issue is one of the three major problems facing humanity. With the rapid depletion of fossil fuels and the growing concern for environmental protection, the development of new energy and new energy materials has become a hot research topic around the world. Solar energy is an important energy resource with renewable and clean features. However, how to efficiently convert and store solar energy is the most important issue for energy utilization and sustainable development. The solar-electric conversion, solar-chemical conversion and solar-thermal conversion are three important solar energy conversion techniques. In terms of energy storage, rechargeable batteries have received much attention in the development of energy storage technologies, due to their practical application in emerging various portable electronic devices, especially in electric vehicles. [225] Among them, high-performance materials are the key points in the development of energy conversion and storage. Organic materials are an important alternative component due to their wide availability, inexpensiveness, and given that their molecular structure and function can be modified and optimized. [226] [227] In this section, we will introduce pyrene-based luminescent (intermediates) materials as energy conversion and storage materials for potential application in organic photovoltaic (OPV) solar cells, rechargeable batteries, and for solar-thermal energy conversion and storage.

Pyrene-based luminescent materials for OPV

Organic photovoltaic (OPV) cells are considered to be emerging light-harvesting technologies, which play a significant role to convert solar energy into electricity. Fullerene and its derivatives possess a large spherical π-electron surface which could be an excellent electron acceptor for OPV solar cells. However, due to their high cost, poor visible light absorption, low phase stabilities, and low phase stabilities, fullerene acceptor-based OPVs display a low device performance. [228, 229] To solve this problem, much effort has contributed to developing non-fullerene acceptors with tuneable photoelectronic properties (such as energy levels, light absorption, and electron mobilities) to replace fullerene. [230] Most non-fullerene acceptor OPV materials exhibit high power conversion efficiencies (PCEs) of up to 17%. [231, 232] Among them, NDI and PDI have been widely used as good electron-deficient groups for OPV applications.[233] Yu *et al*. reported two compounds which were synthesized via the integration of a pyrene-based diimide core and two perylene diimide units at the *ortho*-position. [234] Due to the large π-conjugated framework with a planar structure, compound **140** show an excimer emission with a fluorescence quantum yield of 0.14. Meanwhile, compound **141** exhibits an emission with maximum emission peak at 579 nm with a higher quantum yield of 0.43, which is likely due to the effect of the substituent at β-position of the PDI core, which results in a more twisted molecule. The electron-deficient compounds **140** and **141** were used for application in bulk heterojunction organic photovoltaic (OPV) cells, where the compounds act as electron acceptors and the PBT7-Ph as the donor. The bulk heterojunction OPV cell gives a considerable power conversion efficiency (PCE) value of 4.92% for compound **140**, and 3.53% for compound **141**. Moreover, the electron mobility and hole mobility were calculated to be 4.46×10^{-4} cm^2 V^{-1} s^{-1} and 3.12×10^{-5} cm^2 V^{-1} s^{-1} for compound **140**, and 3.48×10^{-4} cm^2 V^{-1} s^{-1} and 5.33×10^{-5} cm^2 V^{-1} s^{-1} for compound **141**.

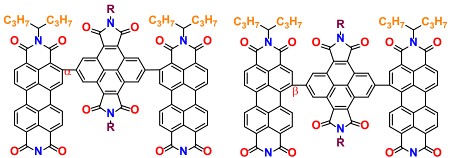

Fig. 48 Synthetic procedure of the pyrene-based diimide containing perylene diimide units **140-141.**

For organic solar cells (OSCs) devices, high-performance cathode interfacial layers (CILs) are one of the most important components for improving the power conversion efficiencies (PCEs) of OSCs. The CILs with low work functions play a crucial role in lowering the interface barriers and allowing for faster charge transport. [235, 236] Organic cathode interfacial materials include types of non-conjugated and conjugated surface modifiers. Among them, the organic cathode interfacial materials with π-conjugated backbones can contribute to exhibiting a good absorption in the range after 300 nm, resulting in an enhanced photocurrent in the devices. 4,5,9,10-Pyrene-based diimides with n-type characteristics could be excellent cathode interfacial materials due to the delocalization of π-electron and the long-wavelength absorption band, as well as their ability to readily form a high film roughness morphology. Zhang *et al.* [237] synthesized three new self-doped pyrene-based diimides **142**-**144** as cathode interfacial materials for improving the PCEs, via introducing amino, amino N-oxide and quaternary ammonium bromide as the functional groups. These compounds exhibit good solubilities, high electron mobility, and have a wide range of light absorption. The OPV devices based on **142**-**144** as CIMs exhibit high PCEs of 17.24% and 17.56%, 18.25% respectively, which is improved by 51.3% compared with that of the device without cathode interfacial layer (12.06%). Due to the presence of the pyrene-based diimide, the devices demonstrated efficient charge transport and extraction processes, as well as high external quantum efficiency of up to 80%. The above-mentioned examples open a new avenue for the development of pyrene-based diimide materials for potential application in organic solar cells.

Given the issues with global warming, how to utilize green energy is becoming increasingly important. Energy conversion technologies and materials are attracting extensive attention both in the academic and industrial communities. Moreover, how to break the theoretical limits to energy conversion efficiency is a key challenge.[238] Multiple exciton generation (MEG) is defined as the situation where one high-energy photon can produce more than one exciton, which is a feasible strategy to go beyond the limiting efficiencies that can harvest the thermalization energy losses. Beard *et al*. observed that 1-pyrenecarboxylic acid can sensitize MEG in semiconductor quantum dots (QDs), via an initial fast electron transfer from pyrene to PbS QDs, and the MEG quantum yield was enhanced from 113 ± 3% to 183 ± 7%. This example offers a possible strategy to enhance MEG using pyrene-based luminescence materials. [239]

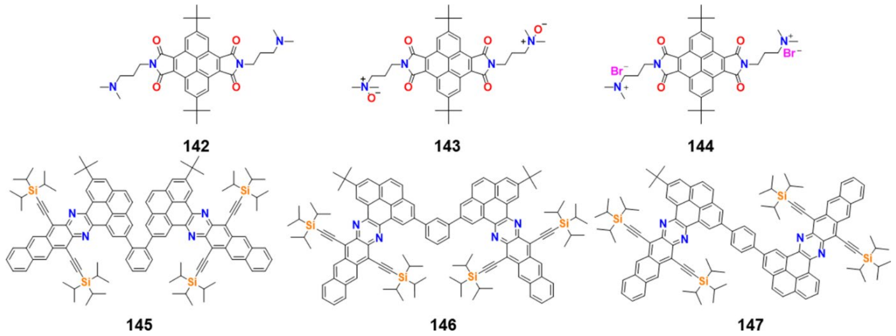

Fig. 49 Molecular structure of the pyrene-based diimides **131**-**133** and pyrene-based azaacenes **134**-**136** for OPV application.

In singlet fission, a single exciton of high-energy could split into two low-energy triplet excitons, which is a promising strategy to overcome the Shockley–Queisser limit. [240] The predicted maximum solar conversion efficiency for a single p-n junction is ~33%. Mateo-Alonso *et al*. reported three new families of pyrene-fused azaacene dimers which were composed of two dibenzodiazahexacene units via a phenylene ring as bridge at the *ortho* (**145**), *meta* (**146**) and *para* (**147**) substitution positions. [241] Among them, the compounds undergo singlet fission with high (T_1T_1) triplet quantum yields of 125% for **145** and 82% for **146** in toluene, respectively. This example offers a new application perspective in solar cells for pyrene-fused azaacene with singlet fission.

Pyrene-based materials for organic batteries

The battery is an energy storage device that can convert chemical energy into electricity. Moreover, rechargeable batteries are considered as an unmatched energy storage technology to solve both energy and environmental problems. The electrode materials are a vital component of traditional commercial rechargeable batteries. For example, Li-ion batteries contain transition-metal oxides or phosphate salts, such as $LiCoO_2$, $LiFePO_4$, or $LiMn_2O_4$ as cathode materials. However, due to their capacity limitations, low stability, and safety concerns, etc., it is imperative that much effort focuses on developing alternative electrode materials for next-generation rechargeable batteries.

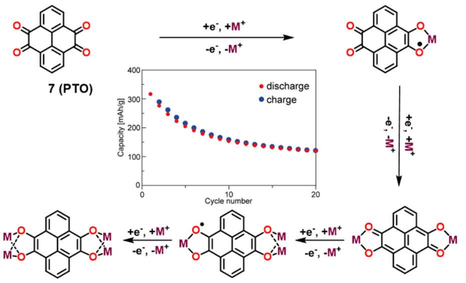

Fig. 50 The optimized structure and redox reaction mechanisms of **PTO** (**7**) electrode materials. Insert: Charge–discharge cycling of pyrene-based intermediate **7**/Li battery (20 cycles, 0.2 C rate) in $LiN(SO_2CF_3)_2$ / tetraglyme at 45 °C. Reproduced from Copyright (2012) & American Chemical Society.[242]

Organic electrode materials have received significant attention for rechargeable batteries, which can achieve a high theoretical and experimental capacity, and great stability. Organic compounds with carbonyl groups not only can react with Li-ion to increase the redox properties, but also cross-link with functional groups to improve electronic conductivity. Since the intermediate pyrene-4,5,9,10-tetraone **PTO** (**7**) was first synthesized by Harris *et al*., [243] it has served as the electrode material in organic batteries, due to its electrochemical performance, high redox potential, and the modifiable active sites. Compound **7** with four carbonyl groups exhibits a high theoretical capacity of 409 mAh g^{-1}, [242] reasonably low reduction potential (0.5 V *versus* SHE), [244], and also displays a high affinity toward alkali metal ions (Li^+, Na^+, and K^+) and alkaline metal ions (Mg^{2+}).[245] Li and coworkers summarized the development of high-performance rechargeable batteries using intermediates **7** and its derivatives in a minireview in 2021. [246] Herein, we will discuss some of the latest examples using pyrene-based materials as organic electrode materials, and introduce new prospects for applying pyrenes in organic batteries.

Yoshida *et al*. first utilized the intermediate **7** as a cathode material in Li-ion batteries, which exhibited a decreased charge-discharge cycling (Figure 50). [242] The main reason is thought to be the greater solubility in organic liquid electrolytes. To solve the problem, four available strategies have been explored to stabilize the charge-discharge cycling and promote the capacity in pyrene-based systems, such as polymerization of **7**, carbon immobilization of **7**, or changing the polarity and optimization of the electrolytes. [246]

When the four carbonyl groups were introduced at the 4,5,9,10-positions of pyrene, the other active sites such as the 2,7-positions can also be further functionalized. Since Yoshida *et al*. reported the polymethacrylate polymer **148** bearing the molecule **7** as a cathode material that exhibits great charge-discharge properties with high capacity (231 mAh g^{-1}), [242] many novel functionalized pyrene-based polymers have been developed for various organic battery applications.

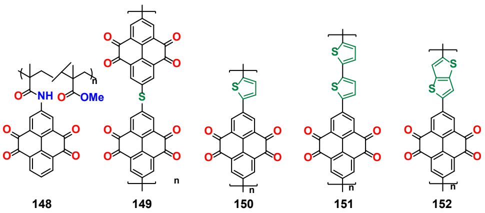

Figure 51. Molecular structure of the pyrene-based polymethacrylate polymers 148, pyrene-based polymer containing sulfur atom **149** or thiophene unit **150**-**152** as an anode material.

Wang *et al*. [247] synthesized a new poly(pyrene-4,5,9,10-tetraone sulfide) **149** via the substitution reaction between intermediate **17** and sodium in sulphide/*N*-methyl pyrrolidone (NMP), which was utilized as an anode material for Li and Na-ion batteries. The polymer **149** exhibits a high reversible specific capacity of 697.1 mAhg $^{-1}$ at 0.1 A g $^{-1}$ and a good rate of performance (335.4 mAhg $^{-1}$ at 1 A g^{-1}). The enhanced electrochemistry performance and conductivity were mainly due to the linkage of the sulfur atom and the linear polymer structure. Furthermore, using the thiophenes 2,2′-bithiophene or thieno[3,2-b]thiophene as linking units, three π-conjugated linear pyrene-based polymers **150**-**152** were synthesized for lithium-ion battery cathode materials. The carbonyl-rich **152** exhibits the best capability (182 mA h g^{-1} at 50 mA g^{-1}), excellent rate of performance (129 mA h g^{-1} at 2 A g^{-1}) and enhanced cycling stability, which was ascribed to the low solubility, expanded π-conjugation and planarity of the molecular frameworks. [248]

On the other hand, the carbonyl groups can be further modified for organic battery application. Seferos *et al*. synthesized a novel pyrene-fused azaacene polymer **153** as the anode material for a lithium-ion battery, which shows an increased capacity up to 1775 mAh g^{-1} (1535 mAh g^{-1}, subtracting the carbon additive contribution) with the number of cycles, ascribe to super-lithiation (Figure 52A and 52B). The high performance of this battery is ascribed to the rigidity of the large π-conjugated pyrene-fused ring, low solubility, and increased conductivity and electrochemical activity. *Ex situ* studies indicated that the amorphous anode electrode material undergoes a deformation-based mechanism of electrode activation, with the number of cycles, the crystallinity and sp^2 character also increased. [249]

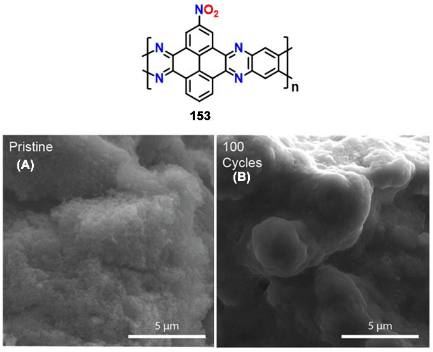

Fig. 52 Pyrene-based polymer structure of **153 and (A)** Cross-sectional scanning electron microscopy of pristine **146** electrode and (B) after 100 cycles at 50 mA g^{-1}. Reproduced from Copyright (2021) American Chemical Society . [249]

Conclusions and outlook

As AIE research has progressed over the past two decades, researchers have tended to pay more attention to luminescent materials in the aggregated state rather than the single molecule state. Pyrene is a crucial building block of luminescent materials and exhibits chemical and physical properties in the aggregated state that are different from those of the individual molecules. This review has highlighted the impact of the aggregation behaviour of pyrene-based materials on both optical and electronic properties. On one hand, pyrene displays an environment-dependent optical behaviour, due to high sensitivity to the microenvironment, which could be a useful fluorescence sensor for detecting the aggregate state of matter. On the other hand, the planar structure of pyrene easily forms a dimer, trimer or tetramer, etc via π-π stacking interactions, resulting in a red-shifted emission with quenched fluorescence. Pyrene is a key component of functional materials, and the pyrene-based molecular structures and their aggregated state play a significant role in affecting their properties, and boost (or limit) their practical application. Thus, great efforts have been devoted to the functionalization of the pyrene core in order to access increased numbers of pyrene-based intermediates and subsequently multi-functional pyrene-based luminescence materials.

The molecular packing in the pyrene system plays a vital role to affect both the optical behaviour and carrier mobility. On one hand, the symmetry structure of pyrene is impossible to show chiral properties, but the formation of intramolecular rigid excimer can induce the strong g_{lum} value in the solid state. On the other hand, the closely π-π stacking is also contributing to lower ΔE_{ST} and fast the RSIC process, resulting in an attractive TADF emission. Besides, the guest molecules were captured into the microporous (channel) of the self-assembled architecture by weak intermolecular interactions, which not only affect the emission intensity, emission colour, but also may increase the electrical conductivity.

New intermediates have been employed to access many types of pyrene-based functional materials, and their molecular structures and aggregation behaviour have been modulated for further improving their properties. For example, to achieve a high-performance luminescence material, it is necessary to suppress the stronger intra-/inter-molecular interactions (such as π-π stacking) via introducing a bulky group at the pyrene core. Moreover, molecular design strategies for constructing various pyrene-based AIE luminescent materials have been developed via decorating twisted moieties to solve the fluorescence quenching associated with pyrene (-based) molecules. Indeed, pyrene-based AIE material-based OLED devices show unique advantages in terms of relatively low turn-on voltage, high luminance and power efficiency, as well as high EUE. According to our calculations, pyrene has a large ΔE_{ST} between S_1 and T_1 up to 1.737 eV, but a low ΔE_{ST} between S_1 and T_2 less than 0.046 eV, indicating that the pyrene-based luminescent materials in the aggregated state are remarkable candidates for promoting the utilization ratio of higher triplet excitons to achieve a larger EQE value (>5%). In this respect, the cited examples open a new opportunity to develop new pyrene-based luminescent materials using precise molecular engineering for high-performance OLED with high brightness, EQE and long lifetime.

In contrast, from the molecular point of view, a well-ordered molecular packing model is more helpful to improve the high hole/electron mobility of organic semiconductor materials. Pyrene possesses a large π-conjugated molecular skeleton and combines a suitable charge-carrier unit, spawning a number of high mobility *p*-/*n*-type pyrene-based semiconductor molecules with charge mobilities ranging from 10^{-4} to $3.08\ \mathrm{cm^2\ V^{-1}\ s^{-1}}$, and high PCE value up to 18.25%. These examples offer solid evidence to confirm the use of pyrene-based luminescent materials for organic electronics applications.

This review provides a new perspective on the self-assembly of pyrene-based luminescent materials which endow fantastic optical and electronic behaviour, such as phosphorescence, CPL and electrical conductivity, dictated by their unique molecular structures and specific aggregate morphology.

Moreover, the pyrene-based intermediate **3** has been employed as a redox centre for organic battery cathode materials. However, the good solubility of **3** in organic electrolytes results in decreased charge-discharge cycling. Thus, much effort has been devoted to the functionalization of **3** as an active precursor for constructing polymers containing pyrene-4,5,9,10-tetraone units for high-capacity organic batteries.

Overall, pyrene-based luminescent materials have emerged as promising materials, for not only fundamental research on the relationship between molecular structure and property modulation, as well as their aggregation behaviour, but also for their efficient synthetic methodology, and high-tech applications in organic electronics, organic batteries, supramolecular self-assembly etc. Although this review has summarized a set of pyrene-based intermediates and their corresponding derivatives with considerable optical behaviour and potential application, there still remain many challenges in terms of controllable approaches to yield high-quality pyrene-based protocols, the morphological modulation, unclear structure-function relationships, and narrowband emission of pyrene-based luminescent materials in the aggregated state. With the development of synthetic techniques and intensive multidisciplinary research, as well as state-of-the-art analytical technology, new pyrene-based luminescent materials should emerge in large numbers, which will open up new avenues to high-performance solid luminescent materials with cutting-edge applications.

Author Contributions

Xing Feng: investigation, visualization, writing-original draft, supervision, funding acquisition; Xing Hui Wang: conceptualization and data curation; Carl Redshaw: supervision and writing-review & editing; Ben Zhong Tang: visualization and supervision.

Conflicts of interest

There are no conflicts to declare.

Acknowledgements

This work was supported by the National Natural Science Foundation of China (21975054), Natural Science Foundation of Guangdong Province of China (2019A1515010925), Shenzhen Key Laboratory of Functional Aggregate Materials (ZDSYS20211021111400001), the Science Technology Innovation Commission of Shenzhen Municipality (KQTD20210811090142053, JCYJ20220818103007014) Guangdong Provincial Key Laboratory of Information Photonics Technology (2020B121201011), the Open Fund of Guangdong Provincial Key Laboratory of Luminescence from Molecular Aggregates, Guangzhou 510640, China (South China University of Technology) (2019B030301003), Science and Technology Planning Project of Hunan Province (2018TP1017), CR thanks the University of Hull for support. XF thanks Dr. Jianyu Zhang (HKUST) for the DFT and TD-DFT calculations.

Notes and references

1. M. W. Davidson, *Microscopy Today*, 2011, **19**, 42-44.
2. G. Feng, G. Q. Zhang and D. Ding, *Chem. Soc. Rev.*, 2020, **49**, 8179-8234.
3. P. Zhou and K. Han, *Aggregate*, 2022, **3**, e160.
4. M. Kasha, *Radiat. Res.*, 1963, **20**, 55-71.
5. H. Yu, B. Chen, H. Huang, Z. He, J. Sun, G. Wang, X. Gu and B. Z. Tang, *Biosensors*, 2022, **12**, 348.
6. Kenry, C. Chen and B. Liu, *Nat. Commun.*, 2019, **10**, 2111.
7. Kenry and B. Liu, *Acc. Mater. Res.*, 2022, **3**, 721-734.
8. J. Qi, C. Chen, D. Ding and B. Z. Tang, *Adv. Healthc. Mater.*, 2018, **7**, e1800477.
9. C. Xu, R. Ye, H. Shen, J. W. Y. Lam, Z. Zhao and B. Zhong Tang, *Angew. Chem. Int. Ed.*, 2022, **61**, e202204604.
10. H. Abroshan, V. Coropceanu and J. L. Brédas, *Adv. Funct. Mater.*, 2020, **30**, 2002916.
11. H. Uoyama, K. Goushi, K. Shizu, H. Nomura and C. Adachi, *Nature*, 2012, **492**, 234-238.
12. L. Frédéric, A. Desmarchelier, L. Favereau and G. Pieters, *Adv. Funct. Mater.*, 2021, **31**, 202010281.
13. S. Hirata, Y. Sakai, K. Masui, H. Tanaka, S. Y. Lee, H. Nomura, N. Nakamura, M. Yasumatsu, H. Nakanotani, Q. Zhang, K. Shizu, H. Miyazaki and C. Adachi, *Nat. Mater.*, 2015, **14**, 330-336.
14. H. Chen, J. Zeng, R. Huang, J. Wang, J. He, H. Liu, D. Yang, D. Ma, Z. Zhao and B. Z. Tang, *Aggregate*, 2022, **4**, e244.
15. A. Ando, K. Ozaki, U. Shiina, E. Nagao, K. Hisano, K. Kamada and O. Tsutsumi, *Aggregate*, 2021, **3,** e125.
16. L. Yao, B. Yang and Y. Ma, *Sci. China Chem.*, 2014, **57**, 335-345.
17. W. Li, Y. Pan, R. Xiao, Q. Peng, S. Zhang, D. Ma, F. Li, F. Shen, Y. Wang, B. Yang and Y. Ma, *Adv. Funct. Mater.*, 2014, **24**, 1609-1614.
18. Y. Xu, X. Liang, Y. Liang, X. Guo, M. Hanif, J. Zhou, X. Zhou, C. Wang, J. Yao, R. Zhao, D. Hu, X. Qiao, D. Ma and Y. Ma, *ACS Appl. Mater. Interfaces*, 2019, **11**, 31139-31146.
19. J. Mei, N. L. C. Leung, R. T. K. Kwok, J. W. Y. Lam and B. Z. Tang, *Chem. Rev.*, 2015, **115**, 11718-11940.
20. J. Luo, Z. Xie, J. W. Lam, L. Cheng, H. Chen, C. Qiu, H. S. Kwok, X. Zhan, Y. Liu, D. Zhu and B. Z. Tang, *Chem. Commun.*, 2001, 1740-1741.
21. J. Mei, Y. Hong, J. W. Lam, A. Qin, Y. Tang and B. Z. Tang, *Adv. Mater.*, 2014, **26**, 5429-5479.
22. Y. Tu, Z. Zhao, J. W. Y. Lam and B. Z. Tang, *Matter*, 2021, **4**, 338-349.
23. T. M. Figueira-Duarte and K. Mullen, *Chem. Rev.*, 2011, **111**, 7260-7314.
24. A. Laurent, *Ann. Chim.Phys.*, 1837, **66**, 136.
25. A. G. Crawford, A. D. Dwyer, Z. Liu, A. Steffen, A. Beeby, L. O. Palsson, D. J. Tozer and T. B. Marder, *J. Am. Chem. Soc.*, 2011, **133**, 13349-13362.
26. A. Nakajima, *Bull. Chem. Soc. Jpn.*, 1971, **44**, 3272-3277.
27. A. Nakajima, *Spectrochim. Acta A Mol. Spectrosc.*, 1974, **30**, 860-862.
28. A. Nakajima, *J. Mol. Spectrosc.*, 1976, **61**, 467-469.
29. K. Kalyanasundaram and J. K. Thomas, *J. Am. Chem. Soc.*, 1977, **99**, 2039-2044.
30. L. J. C. Love and J. G. Dorsey, *Anal. Chem.*, 2011, **56**, 1132A-1148A.
31. C. Honda, M. Itagaki, R. Takeda and K. Endo, *Langmuir*, 2002, **18**, 1999-2003.
32. V. A. Ganaye, K. Keiding, T. M. Vogel, M.-L. Viriot and J.-C. Block, *Environ. Sci. Technol.*, 1997, **31**, 2701-2706.
33. S. V. Aathimanikandan, E. N. Savariar and S. Thayumanavan, *J. Am. Chem. Soc.*, 2005, **127**, 14922-14929.
34. Basim Abdullattif Ghalib, Ghaleb A. Al-Dahash, Ghaidaa A.Hafed Jaber and H. I. Abbood, *Aust. J. Basic Appl. Sci.*, 2014, **8**, 138-148.
35. A. Picchiotti, A. Nenov, A. Giussani, V. I. Prokhorenko, R. J. D. Miller, S. Mukamel and M. Garavelli, *J. Phys. Chem. Lett.*, 2019, **10**, 3481-3487.
36. X. Xu, S. Gunasekaran, S. Renken, L. Ripani, D. Schollmeyer, W. Kim, M. Marcaccio, A. Musser and A. Narita, *Adv. Sci.,* 2022, **9**, e2200004.
37. E. Manandhar and K. J. Wallace, *Inorg. Chim. Acta*, 2012, **381**, 15-43.
38. T. Förster, *Angew. Chem. Int. Ed.*, 1969, **8**, 333-343.
39. F. M. Winnik, *Chem. Rev.*, 2002, **93**, 587-614.
40. M. D. Cohen, *Mol. Cryst. Liq. Cryst.*, 2007, **50**, 1-10.
41. Y. Deng, W. Yuan, Z. Jia and G. Liu, *J. Phys. Chem. B*, 2014, **118**, 14536-14545.
42. E. G. McRae and M. Kasha, *J. Chem. Phy.*, 1958, **28**, 721-722.
43. F. C. Spano, *Acc. Chem. Res.*, 2010, **43**, 429-439.
44. M. Más-Montoya and R. A. J. Janssen, *Adv. Funct. Mater.*, 2017, **27**, 1605779.
45. C. Z. Wang, H. Ichiyanagi, K. Sakaguchi, X. Feng, M. R. J. Elsegood, C. Redshaw and T. Yamato, *J. Org. Chem.*, 2017, **82**, 7176-7182.
46. B. Heyne, *Photochem. Photobiol. Sci.*, 2016, **15**, 1103-1114.
47. C. P. Hsu, *Acc. Chem. Res.*, 2009, **42**, 509-518.
48. S. Li, L. Fu, X. Xiao, H. Geng, Q. Liao, Y. Liao and H. Fu, *Angew. Chem. Int. Ed.*, 2021, **60**, 18059-18064.
49. H. Wang, X. Ji, Z. A. Page and J. L. Sessler, *Mater. Chem. Front.*, 2020, **4**, 1024-1039.
50. X. H. Wang, L. R. Wang, X. Y. Mao, Q. S. Wang, Z. F. Mu, L. An, W. Zhang, X. Feng, C. Redshaw, C. Y. Cao, A. J. Qin and B. Z. Tang, *J. Mater. Chem. C*, 2021, **9**, 12828-12838.
51. K. Ayyavoo and P. Velusamy, *New J. Chem.*, 2021, **45**, 10997-11017.
52. T. Oyamada, H. Uchiuzou, S. Akiyama, Y. Oku, N. Shimoji, K. Matsushige, H. Sasabe and C. Adachi, *J. Appl. Phys.*, 2005, **98**.
53. X. Feng, J. Y. Hu, C. Redshaw and T. Yamato, *Chem. Eur. J.*, 2016, **22**, 11898-11916.
54. H. T. Feng, Y. X. Yuan, J. B. Xiong, Y. S. Zheng and B. Z. Tang, *Chem. Soc. Rev.*, 2018, **47**, 7452-7476.
55. M. M. Islam, Z. Hu, Q. S. Wang, C. Redshaw and X. Feng, *Mater. Chem. Front.*, 2019, **3**, 762-781.
56. J. Katla, H. R. Bhat, P. C. Jha, P. S. Ghalsasi and S. Kanvah, *ChemistrySelect*, 2017, **2**, 1902-1910.
57. X. Feng, J. Zhang, Z. Hu, Q. Wang, M. M. Islam, J.-S. Ni, M. R. J. Elsegood, J. W. Y. Lam, E. Zhou and B. Z. Tang, *J. Mater. Chem. C*, 2019, **7**, 6932-6940.
58. Y. Tsutsui, W. Zhang, S. Ghosh, T. Sakurai, H. Yoshida, M. Ozaki, T. Akutagawa and S. Seki, *Adv. Optical Mater.*, 2020, **8**, 1902158.

59. P. F. Barbara, P. K. Walsh and L. E. Brus, *J. Phy. Chem.*, 1989, **93**, 29-34.
60. V. S. Padalkar and S. Seki, *Chem. Soc. Rev.*, 2016, **45**, 169-202.
61. C. Bai, J. Zhang, Y. Qin, H. Huang, Z. Xia, Q. Zheng, H. Dai, P. Lu, H. Miao, C. Qu and R. Qiao, *Chem. Eng. J.*, 2022, **443**.
62. Z. Peng, Z. Wang, B. Tong, Y. Ji, J. Shi, J. Zhi and Y. Dong, *Chin. J. Chem.*, 2016, **34**, 1071-1075.
63. S. Sasaki, S. Suzuki, K. Igawa, K. Morokuma and G. I. Konishi, *J. Org. Chem.*, 2017, **82**, 6865-6873.
64. Y.-R. Shi, H.-l. Wei, Y.-t. Shi and Y.-F. Liu, *Synth. Met.*, 2017, **223**, 218-225.
65. B. R. Kaafarani, L. A. Lucas, B. Wex and G. E. Jabbour, *Tetrahedron Lett.*, 2007, **48**, 5995-5998.
66. Y.-C. Kung and S.-H. Hsiao, *J. Mater. Chem.*, 2010, **20**.
67. A. Mateo-Alonso, *Chem. Soc. Rev.*, 2014, **43**, 6311-6324.
68. M. J. S. Dewar and R. D. Dennington, *J. Am. Chem. Soc.*, 2002, **111**, 3804-3808.
69. S. N. Keller, N. L. Veltri and T. C. Sutherland, *Org. Lett.*, 2013, **15**, 4798-4801.
70. L. Zophel, D. Beckmann, V. Enkelmann, D. Chercka, R. Rieger and K. Mullen, *Chem. Commun.*, 2011, **47**, 6960-6962.
71. M. Bauch, K. Toma, M. Toma, Q. Zhang and J. Dostalek, *Plasmonics*, 2014, **9**, 781-799.
72. K. Saito, K. McGehee and Y. Norikane, *Nanoscale Adv*, 2021, **3**, 3272-3278.
73. D. J. Kang and B. S. Bae, *Acc. Chem. Res.*, 2007, **40**, 903-912.
74. J. R. Ritter, M. J. Caldas, T. J. da Silva, A. Calzolari and M. D. McCluskey, *ACS Appl. Electron. Mater.*, 2020, **2**, 2806-2812.
75. G. Battistini, P. G. Cozzi, J. P. Jalkanen, M. Montalti, L. Prodi, N. Zaccheroni and F. Zerbetto, *ACS Nano*, 2008, **2**, 77-84.
76. L. Jiang, A. C. Papageorgiou, S. C. Oh, O. Saglam, J. Reichert, D. A. Duncan, Y. Q. Zhang, F. Klappenberger, Y. Guo, F. Allegretti, S. More, R. Bhosale, A. Mateo-Alonso and J. V. Barth, *ACS Nano*, 2016, **10**, 1033-1041.
77. P. Sonar, M. S. Soh, Y. H. Cheng, J. T. Henssler and A. Sellinger, *Org. Lett.*, 2010, **12**, 3292-3295.
78. X. Wang, C. Zhang, J. Zeng, X. Mao, C. Redshaw, G. Niu, X. Yu and X. Feng, *J. Org. Chem.*, 2022, **87**, 12741-12748.
79. G. Venkataramana and S. Sankararaman, *Org. Lett.*, 2006, **8**, 2739-2742.
80. V. Khokhar, M. Kumar and S. Pandey, *Phys. Chem. Chem. Phys.*, 2022, **25**, 64-68.
81. X. Wang, J. Zhang, X. Mao, Y. Liu, R. Li, J. Bai, J. Zhang, C. Redshaw, X. Feng and B. Z. Tang, *J. Org. Chem.*, 2022, **87**, 8503-8514.
82. Z. Kowser, U. Rayhan, T. Akther, C. Redshaw and T. Yamato, *Mater. Chem. Front.*, 2021, **5**, 2173-2200.
83. Z. He, J. Wu, B. Qiao, H. Pei, Q. Xia, Q. Wu and H. Ju, *ACS Appl. Bio. Mater.*, 2020, **3**, 5342-5349.
84. U. Saha, S. Chatterjee, M. Dolai and G. Suresh Kumar, *ACS Appl. Bio. Mater.*, 2020, **3**, 7810-7820.
85. B. Daly, J. Ling and A. P. de Silva, *Chem. Soc. Rev.*, 2015, **44**, 4203-4211.
86. P. Beyazkilic, A. Yildirim and M. Bayindir, *ACS Appl. Mater. Interfaces*, 2014, **6**, 4997-5004.
87. G. B. Demirel, B. Daglar and M. Bayindir, *Chem. Commun.*, 2013, **49**, 6140-6142.
88. Z.-D. Yu, J.-Y. Cao, H.-L. Li, G. Yang, W.-X. Zhao, C.-Z. Wang, S.-H. Chen, M. R. J. Elsegood, C. Redshaw and T. Yamato, *J. Lumin.*, 2023, **253.**
89. M. Liu, Y. Chen, Y. Guo, H. Yuan, T. Cui, S. Yao, S. Jin, H. Fan, C. Wang, R. Xie, W. He and Z. Guo, *Nat. Commun.*, 2022, **13**, 2179.
90. J. L. Doob, *The Annals of Mathematics*, 1942, **43**.
91. S. Liu, Y. Li, H. Zhang, Z. Zhao, X. Lu, J. W. Y. Lam and B. Z. Tang, *ACS Mater. Lett.*, 2019, **1**, 425-431.
92. X. Song, H. Guo, S. Yu, L. Huang, C. Redshaw, Q. Zhang, R. Ye and X. Feng, *Dyes Pigm.*, 2023, **210**.
93. P. Alam, N. L. C. Leung, Y. Cheng, H. Zhang, J. Liu, W. Wu, R. T. K. Kwok, J. W. Y. Lam, H. H. Y. Sung, I. D. Williams and B. Z. Tang, *Angew. Chem. Int. Ed.*, 2019, **58**, 4536-4540.
94. J. Zhang, X. Zhao, H. Shen, J. W. Y. Lam, H. Zhang and B. Z. Tang, *Adv. Photonics*, 2021, **4**, 014001.
95. X. Feng, C. Qi, H. T. Feng, Z. Zhao, H. H. Y. Sung, I. D. Williams, R. T. K. Kwok, J. W. Y. Lam, A. Qin and B. Z. Tang, *Chem. Sci.*, 2018, **9**, 5679-5687.
96. M. Bayda-Smykaj, G. Burdzinski, M. Ludwiczak, G. L. Hug and B. Marciniak, *J. Phy. Chem. C*, 2020, **124**, 19522-19529.
97. M. Bayda-Smykaj, K. Rachuta, G. L. Hug, M. Majchrzak and B. Marciniak, *J. Phy. Chem. C*, 2021, **125**, 12488-12495.
98. Q. J. Shen, H. Q. Wei, W. S. Zou, H. L. Sun and W. J. Jin, *CrystEngComm*, 2012, **14**, 1010-1015.
99. W. Dai, X. Niu, X. Wu, Y. Ren, Y. Zhang, G. Li, H. Su, Y. Lei, J. Xiao, J. Shi, B. Tong, Z. Cai and Y. Dong, *Angew. Chem. Int. Ed.*, 2022, **61**, e202200236.
100. M. A. Omary, R. M. Kassab, M. R. Haneline, O. Elbjeirami and F. P. Gabbai, *Inorg. Chem.*, 2003, **42**, 2176-2178.
101. X. Meng, Q. Hu, X. Wang, T. Ma, W. Liu, X. Zhu and C. Ye, *J. Mater. Chem. C*, 2022, **10**, 17620-17627.
102. H. Wu, D. Wang, Z. Zhao, D. Wang, Y. Xiong and B. Z. Tang, *Adv. Funct. Mater.*, 2021, **31**.
103. H. Zhang, X. Chang, C. Ma, G. Huang, B. S. Li and B. Z. Tang, *ACS Appl. Mater. Interfaces*, 2022, **14**, 43926-43936.
104. Z. Liu, Y. Wang, Y. Chen, J. Liu, Q. Fang, C. Kleeberg and T. B. Marder, *J. Org. Chem.*, 2012, **77**, 7124-7128.
105. Y.-B. Gong, P. Zhang, Y.-r. Gu, J.-Q. Wang, M.-M. Han, C. Chen, X.-J. Zhan, Z.-L. Xie, B. Zou, Q. Peng, Z.-G. Chi and Z. Li, *Adv. Optical Mater.*, 2018, **6**.
106. V. C. Wakchaure, K. C. Ranjeesh, Goudappagouda, T. Das, K. Vanka, R. Gonnade and S. S. Babu, *Chem. Commun.*, 2018, **54**, 6028-6031.
107. T. Mori, *Chem. Rev.*, 2021, **121**, 2373-2412.
108. B. Lefeuvre, C. A. Mattei, J. F. Gonzalez, F. Gendron, V. Dorcet, F. Riobe, C. Lalli, B. Le Guennic, O. Cador, O. Maury, S. Guy, A. Bensalah-Ledoux, B. Baguenard and F. Pointillart, *Chem. Eur. J.*, 2021, **27**, 7362-7366.
109. G. Albano, L. A. Aronica, A. Minotto, F. Cacialli and L. Di Bari, *Chem. Eur. J.*, 2020, **26**, 16622-16627.
110. T. Zhao, J. Han, P. Duan and M. Liu, *Acc. Chem. Res.*, 2020, **53**, 1279-1292.
111. K. Hassan, K.-i. Yamashita, K. Hirabayashi, T. Shimizu, K. Nakabayashi, Y. Imai, T. Matsumoto, A. Yamano and K.-i. Sugiura, *Chem. Lett.*, 2015, **44**, 1607-1609.
112. K.-i. Sugiura and U. A. Liza, *Synthesis*, 2020, **52**, 3452-3460.

113. Y. Zheng, L. Zhao, Y. Zhang, C. Wang, K. Wang, D. Qi and J. Jiang, *Dyes Pigm.*, 2017, **141**, 245-250.
114. K. Takaishi, K. Iwachido and T. Ema, *J. Am. Chem. Soc.*, 2020, **142**, 1774-1779.
115. K. Kano, H. Matsumoto, S. Hashimoto, M. Sisido and Y. Imanishi, *J. Am. Chem. Soc.*, 1985, **107**, 6117-6118.
116. K. Takaishi, S. Murakami, F. Yoshinami and T. Ema, *Angew. Chem. Int. Ed.*, 2022, **61**, e202204609.
117. Z.-L. Gong, X. Zhu, Z. Zhou, S.-W. Zhang, D. Yang, B. Zhao, Y.-P. Zhang, J. Deng, Y. Cheng, Y.-X. Zheng, S.-Q. Zang, H. Kuang, P. Duan, M. Yuan, C.-F. Chen, Y. S. Zhao, Y.-W. Zhong, B. Z. Tang and M. Liu, *Sci. China Chem.*, 2021, **64**, 2060-2104.
118. Y. Zhu, Z. Xia, Z. Cai, Z. Yuan, N. Jiang, T. Li, Y. Wang, X. Guo, Z. Li, S. Ma, D. Zhong, Y. Li and J. Wang, *J. Am. Chem. Soc.*, 2018, **140**, 4222-4226.
119. T. Hosokawa, Y. Takahashi, T. Matsushima, S. Watanabe, S. Kikkawa, I. Azumaya, A. Tsurusaki and K. Kamikawa, *J. Am. Chem. Soc.*, 2017, **139**, 18512-18521.
120. J.-Y. Hu, X. Feng, A. Paudel, H. Tomiyasu, U. Rayhan, P. Thuéry, M. R. J. Elsegood, C. Redshaw and T. Yamato, *Eur. J. Org. Chem.*, 2013, **2013**, 5829-5837.
121. J. Y. Hu, A. Paudel, N. Seto, X. Feng, M. Era, T. Matsumoto, J. Tanaka, M. R. J. Elsegood, C. Redshaw and T. Yamato, *Org. Biomol. Chem.*, 2013, **11**, 2186-2197.
122. C.-Z. Wang, R. Kihara, X. Feng, P. Thuéry, C. Redshaw and T. Yamato, *ChemistrySelect*, 2017, **2**, 1436-1441.
123. A. K. Swain, K. Kolanji, C. Stapper and P. Ravat, *Org. Lett.*, 2021, **23**, 1339-1343.
124. A. K. Swain, K. Radacki, H. Braunschweig and P. Ravat, *J. Org. Chem.*, 2022, **87**, 993-1000.
125. S. Hu, L. Hu, X. Zhu, Y. Wang and M. Liu, *Angew. Chem. Int. Ed.*, 2021, **60**, 19451-19457.
126. L. Hu, X. Zhu, C. Yang and M. Liu, *Angew. Chem. Int. Ed.*, 2022, **61**, e202114759.
127. H. Shigemitsu, K. Kawakami, Y. Nagata, R. Kajiwara, S. Yamada, T. Mori and T. Kida, *Angew. Chem. Int. Ed.*, 2022, **61**, e202114700.
128. C. Tu, W. Wu, W. Liang, D. Zhang, W. Xu, S. Wan, W. Lu and C. Yang, *Angew. Chem. Int. Ed.*, 2022, **61**, e202203541.
129. J. Calbo, M. J. Golomb and A. Walsh, *J. Mater. Chem. A*, 2019, **7**, 16571-16597.
130. N. S. Bobbitt, M. L. Mendonca, A. J. Howarth, T. Islamoglu, J. T. Hupp, O. K. Farha and R. Q. Snurr, *Chem. Soc. Rev.*, 2017, **46**, 3357-3385.
131. Y. Hao, E. K. Papazyan, Y. Ba and Y. Liu, *ACS Catal*, 2021, **12**, 363-371.
132. F. P. Kinik, A. Ortega-Guerrero, F. M. Ebrahim, C. P. Ireland, O. Kadioglu, A. Mace, M. Asgari and B. Smit, *ACS Appl. Mater. Interfaces*, 2021, **13**, 57118-57131.
133. A. Singh, A. K. Singh, J. Liu and A. Kumar, *Catal. Sci. Technol.*, 2021, **11**, 3946-3989.
134. S. Kumar, B. Mohan, Z. Tao, H. You and P. Ren, *Catal. Sci. Technol.*, 2021, **11**, 5734-5771.
135. W. P. Lustig, S. Mukherjee, N. D. Rudd, A. V. Desai, J. Li and S. K. Ghosh, *Chem. Soc. Rev.*, 2017, **46**, 3242-3285.
136. Y.-G. Li, J.-J. Hu, J.-L. Zhang, S.-J. Liu, Y. Peng and H.-R. Wen, *CrystEngComm*, 2022, **24**, 2464-2471.
137. M. Li, R. P. Hicks, Z. Chen, C. Luo, J. Guo, C. Wang and Y. Xu, *Chem. Rev.*, 2023, **4**, 1712–1773.
138. S. Huang, G. Chen and G. Ouyang, *Chem. Soc. Rev.*, 2022, **51**, 6824-6863.
139. J. Jacobsen, A. Ienco, R. D'Amato, F. Costantino and N. Stock, *Dalton Trans.*, 2020, **49**, 16551-16586.
140. Z. Hu, Y. Wang and D. Zhao, *Chem. Soc. Rev.*, 2021, **50**, 4629-4683.
141. M. L. Lu, W. Huang, S. Gao, J. L. Zhang, W. B. Liang, Y. Li, R. Yuan and D. R. Xiao, *Anal. Chem.*, 2022, **94**, 15832-15838.
142. L. Zhu, B. Zhu, J. Luo and B. Liu, *ACS Mater. Lett.*, 2021, **3**, 77-89.
143. M. D. Allendorf, C. A. Bauer, R. K. Bhakta and R. J. Houk, *Chem. Soc. Rev.*, 2009, **38**, 1330-1352.
144. F. P. Kinik, A. Ortega-Guerrero, D. Ongari, C. P. Ireland and B. Smit, *Chem. Soc. Rev.*, 2021, **50**, 3143-3177.
145. S. S. Rajasree, X. Li and P. Deria, *Commun. Chem*, 2021, **4**, 47.
146. K. C. Stylianou, R. Heck, S. Y. Chong, J. Bacsa, J. T. Jones, Y. Z. Khimyak, D. Bradshaw and M. J. Rosseinsky, *J. Am. Chem. Soc.*, 2010, **132**, 4119-4130.
147. Z. Yang, Y. Wang, X. Liu, R. T. Vanderlinden, R. Ni, X. Li and P. J. Stang, *J. Am. Chem. Soc.*, 2020, **142**, 13689-13694.
148. L. Sun, M. G. Campbell and M. Dinca, *Angew. Chem. Int. Ed.* 2016, **55**, 3566-3579.
149. N. C. Jeong, B. Samanta, C. Y. Lee, O. K. Farha and J. T. Hupp, *J. Am. Chem. Soc.*, 2012, **134**, 51-54.
150. D. Rambabu, A. E. Lakraychi, J. Wang, L. Sieuw, D. Gupta, P. Apostol, G. Chanteux, T. Goossens, K. Robeyns and A. Vlad, *J. Am. Chem. Soc.*, 2021, **143**, 11641-11650.
151. S. Jin, *ACS Energy Lett*, 2019, **4**, 1443-1445.
152. L. Cao and C. Wang, *ACS Cent Sci*, 2020, **6**, 2149-2158.
153. C. Li, H. Zhang, M. Liu, F.-F. Lang, J. Pang and X.-H. Bu, *Ind. Chem. Mater.*, 2023, **1**, 9-38. Ind. Chem. Res.
154. L. Sun, M. G. Campbell and M. Dinca, *Angew. Chem. Int. Ed.*, 2016, **55**, 3566-3579.
155. L. S. Xie, G. Skorupskii and M. Dinca, *Chem. Rev.*, 2020, **120**, 8536-8580.
156. J. E. Mondloch, W. Bury, D. Fairen-Jimenez, S. Kwon, E. J. DeMarco, M. H. Weston, A. A. Sarjeant, S. T. Nguyen, P. C. Stair, R. Q. Snurr, O. K. Farha and J. T. Hupp, *J. Am. Chem. Soc.*, 2013, **135**, 10294-10297.
157. C. W. Kung, K. Otake, C. T. Buru, S. Goswami, Y. Cui, J. T. Hupp, A. M. Spokoyny and O. K. Farha, *J. Am. Chem. Soc.*, 2018, **140**, 3871-3875.
158. C. N. Coleman, P. C. Tapping, M. T. Huxley, T. W. Kee, D. M. Huang, C. J. Doonan and C. J. Sumby, *CrystEngComm*, 2021, **23**, 82-90.
159. C. W. Kung, S. Goswami, I. Hod, T. C. Wang, J. Duan, O. K. Farha and J. T. Hupp, *Acc. Chem. Res.*, 2020, **53**, 1187-1195.
160. Y. Tao, H. F. Chan, B. Shi, M. Li and K. W. Leong, *Adv. Funct. Mater.*, 2020, **30**, 2005029.
161. B. Zhao, Q. Yang, J.-S. Wang, F.-Y. Xie, H.-Y. Yu, Y. Li, Y.-X. Ma and W.-J. Ruan, *New J. Chem.*, 2021, **45**, 4401-4407.
162. X.-G. Yang, J.-H. Qin, Y.-D. Huang, Z.-M. Zhai, L.-F. Ma and D. Yan, *J. Mater. Chem. C*, 2020, **8**, 17169-17175.
163. A. P. Cote, A. I. Benin, N. W. Ockwig, M. O'Keeffe, A. J. Matzger and O. M. Yaghi, *Science*, 2005, **310**, 1166-1170.

164. Z. Meng and K. A. Mirica, *Chem. Soc. Rev.*, 2021, **50**, 13498-13558.
165. S. Mallakpour, E. Azadi and C. M. Hussain, *New J. Chem.*, 2021, **45**, 7014-7046.
166. J. Li, X. Jing, Q. Li, S. Li, X. Gao, X. Feng and B. Wang, *Chem. Soc. Rev.*, 2020, **49**, 3565-3604.
167. Q. Guan, L. L. Zhou and Y. B. Dong, *Chem. Soc. Rev.*, 2022, **51**, 6307-6416.
168. D. Ongari, A. V. Yakutovich, L. Talirz and B. Smit, *ACS Cent. Sci*, 2019, **5**, 1663-1675.
169. D. Ongari, A. V. Yakutovich, L. Talirz, B. Smit, Building a consistent and reproducible database for adsorption evaluation in Covalent-Organic Frameworks. Material Cloud Archive 2021.100.
170. S. Wan, J. Guo, J. Kim, H. Ihee and D. Jiang, *Angew. Chem. Int. Ed.*, 2009, **48**, 5439-5442.
171. N. Keller and T. Bein, *Chem. Soc. Rev.*, 2021, **50**, 1813-1845.
172. W. Liu, L. Gong, Z. Liu, Y. Jin, H. Pan, X. Yang, B. Yu, N. Li, D. Qi, K. Wang, H. Wang and J. Jiang, *J. Am. Chem. Soc.*, 2022, **144**, 17209-17218.
173. A. Natraj, W. Ji, J. Xin, I. Castano, D. W. Burke, A. M. Evans, M. J. Strauss, M. Ateia, L. S. Hamachi, N. C. Gianneschi, A. L. ZA, J. Sun, K. Yusuf and W. R. Dichtel, *J. Am. Chem. Soc.*, 2022, **144**, 19813-19824.
174. J. Y. Zeng, X. S. Wang, Y. X. Sun and X. Z. Zhang, *Biomaterials*, 2022, **286**, 121583.
175. G. Lin, H. Ding, D. Yuan, B. Wang and C. Wang, *J. Am. Chem. Soc.*, 2016, **138**, 3302-3305.
176. R. Hu, N. L. Leung and B. Z. Tang, *Chem. Soc. Rev.*, 2014, **43**, 4494-4562.
177. Y. Su, B. Li, H. Xu, C. Lu, S. Wang, B. Chen, Z. Wang, W. Wang, K. I. Otake, S. Kitagawa, L. Huang and C. Gu, *J. Am. Chem. Soc.*, 2022, **144**, 18218-18222.
178. L. Feng, K. Y. Wang, G. S. Day and H. C. Zhou, *Chem. Soc. Rev.*, 2019, **48**, 4823-4853.
179. P. L. Wang, S. Y. Ding, Z. C. Zhang, Z. P. Wang and W. Wang, *J. Am. Chem. Soc.*, 2019, **141**, 18004-18008.
180. N. Keller, D. Bessinger, S. Reuter, M. Calik, L. Ascherl, F. C. Hanusch, F. Auras and T. Bein, *J. Am. Chem. Soc.*, 2017, **139**, 8194-8199.
181. E. Jin, J. Li, K. Geng, Q. Jiang, H. Xu, Q. Xu and D. Jiang, *Nat. Commun.*, 2018, **9**, 4143.
182. Q. Gao, X. Li, G. H. Ning, K. Leng, B. Tian, C. Liu, W. Tang, H. S. Xu and K. P. Loh, *Chem. Commun.*, 2018, **54**, 2349-2352.
183. S. Xu and Q. Zhang, *Mater. Today Energy*, 2021, **20**.
184. Y. Zhao, X.-X. Zuo, H.-J. Huang, S.-Y. Gao, J.-Z. Wang, Z. Chen, W. Ngeontae and X.-K. Ren, *J. Phy. Chem. C*, 2022, **126**, 14566-14572.
185. A. Eluri, K. Sairam, J. D. Halpara and N. A. Babujohn, *ACS Appl. Polymer Mater.*, 2022, **4**, 6936-6948.
186. B. T. Liu, X. H. Pan, D. Y. Nie, X. J. Hu, E. P. Liu and T. F. Liu, *Adv. Mater.*, 2020, **32**, e2005912.
187. D. Yu, H. Zhang, Z. Liu, C. Liu, X. Du, J. Ren and X. Qu, *Angew. Chem. Int. Ed.*, 2022, **61**, e202201485.
188. A. Shang, T. Lu, H. Liu, C. Du, F. Liu, D. Jiang, J. Min, H. Zhang and P. Lu, *J. Mater. Chem. C*, 2021, **9**, 7392-7399.
189. T. Yang, Z. Cheng, Z. Li, J. Liang, Y. Xu, C. Li and Y. Wang, *Adv. Funct. Mater.*, 2020, **30**, 2002681.
190. X. J. Wang, H. Liu, K. Zhang, D. Yang, Z. H. Pan, C. K. Wang, M. K. Fung, D. Ma and J. Fan, *Mater. Horiz*, 2023, **10**, 938-944.
191. X. Qiu, S. Ying, C. Wang, M. Hanif, Y. Xu, Y. Li, R. Zhao, D. Hu, D. Ma and Y. Ma, *J. Mater. Chem. C*, 2019, **7**, 592-600.
192. Y. Liu, H. Liu, Q. Bai, C. Du, A. Shang, D. Jiang, X. Tang and P. Lu, *ACS Appl. Mater. Interfaces*, 2020, **12**, 16715-16725.
193. Y. Liu, X. Man, Q. Bai, H. Liu, P. Liu, Y. Fu, D. Hu, P. Lu and Y. Ma, *CCS Chem.*, 2022, **4**, 214-227.
194. J. Zeng, N. Qiu, J. Zhang, X. Wang, C. Redshaw, X. Feng, J. W. Y. Lam, Z. Zhao and B. Z. Tang, *Adv. Optical Mater.*, 2022, **10**, 202200917.
195. J. Yang, L. Li, Y. Yu, Z. Ren, Q. Peng, S. Ye, Q. Li and Z. Li, *Mater. Chem. Front.*, 2017, **1**, 91-99.
196. Z. Zhao, S. Chen, J. W. Y. Lam, Z. Wang, P. Lu, F. Mahtab, H. H. Y. Sung, I. D. Williams, Y. Ma, H. S. Kwok and B. Z. Tang, *J. Mater. Chem.*, 2011, **21**.
197. Z. Zhao, S. Chen, J. W. Lam, P. Lu, Y. Zhong, K. S. Wong, H. S. Kwok and B. Z. Tang, *Chem. Commun.*, 2010, **46**, 2221-2223.
198. X. Feng, Z. Xu, Z. Hu, C. Qi, D. Luo, X. Zhao, Z. Mu, C. Redshaw, J. W. Y. Lam, D. Ma and B. Z. Tang, *J. Mater. Chem. C*, 2019, **7**, 2283-2290.
199. X. Feng, J. Y. Hu, F. Iwanaga, N. Seto, C. Redshaw, M. R. J. Elsegood and T. Yamato, *Org. Lett.*, 2013, **15**, 1318-1321.
200. X. Feng, J. Y. Hu, H. Tomiyasu, Z. Tao, C. Redshaw, M. R. J. Elsegood, L. Horsburgh, S. J. Teat, X. F. Wei and T. Yamato, *Rsc Adv.*, 2015, **5**, 8835-8848.
201. X. Feng, J. Y. Hu, H. Tomiyasu, N. Seto, C. Redshaw, M. R. Elsegood and T. Yamato, *Org. Biomol. Chem.*, 2013, **11**, 8366-8374.
202. C.-Z. Wang, X. Feng, Z. Kowser, C. Wu, T. Akther, M. R. J. Elsegood, C. Redshaw and T. Yamato, *Dyes Pigm.*, 2018, **153**, 125-131.
203. H. Ran, Z. Zhao, X. Duan, F. Xie, R. Han, H. Sun and J.-Y. Hu, *J. Mater. Chem. C*, 2021, **9**, 260-269.
204. F. Xie, X. Yang, P. Jin, X.-T. Wang, H. Ran, R. Zheng, Z. Lei, H. Zhang, S.-J. Su and J.-Y. Hu, *J. Mater. Chem. C*, 2022, **10**, 10866-10875.
205. F. Xie, X. Yang, P. Jin, X. T. Wang, H. Ran, H. Zhang, H. Sun, S. J. Su and J. Y. Hu, *Adv. Optical Mater.*, 2022, **11,** 2202490.
206. X. Yang, Z. Zhao, H. Ran, J. Zhang, L. Chen, R. Han, X. Duan, H. Sun and J.-Y. Hu, *Dyes Pigm.*, 2020, **173**, 107881.
207. F. Xie, H. Ran, X. Duan, R. Han, H. Sun and J.-Y. Hu, *J. Mater. Chem. C*, 2020, **8**, 17450-17456.
208. J.-Y. Hu, Y.-J. Pu, F. Satoh, S. Kawata, H. Katagiri, H. Sasabe and J. Kido, *Adv. Funct. Mater.*, 2014, **24**, 2064-2071.
209. H. Jung, S. Kang, H. Lee, Y. J. Yu, J. H. Jeong, J. Song, Y. Jeon and J. Park, *ACS Appl. Mater. Interfaces*, 2018, **10**, 30022-30028.
210. H. Zhang, Y. Wang, K. Shao, Y. Liu, S. Chen, W. Qiu, X. Sun, T. Qi, Y. Ma, G. Yu, Z. Su and D. Zhu, *Chem. Commun.*, 2006, 755-757.
211. Y. Qiao, J. Zhang, W. Xu and D. Zhu, *Tetrahedron*, 2011, **67**, 3395-3405.
212. H. Ju, K. Wang, J. Zhang, H. Geng, Z. Liu, G. Zhang, Y. Zhao and D. Zhang, *Chem. Mater.*, 2017, **29**, 3580-3588.
213. J. Cornil, V. Lemaur, J. P. Calbert and J. L. Brédas, *Adv. Mater.*, 2002, **14**, 726-729.

214. C. Cui and Y. Li, *Energy Environ. Sci.*, 2019, **12**, 3225-3246.
215. S. V. Bhosale, M. Al Kobaisi, R. W. Jadhav, P. P. Morajkar, L. A. Jones and S. George, *Chem. Soc. Rev.*, 2021, **50**, 9845-9998.
216. R. Schroot, M. Jager and U. S. Schubert, *Chem. Soc. Rev.*, 2017, **46**, 2754-2798.
217. S. Yuvaraja, A. Nawaz, Q. Liu, D. Dubal, S. G. Surya, K. N. Salama and P. Sonar, *Chem. Soc. Rev.*, 2020, **49**, 3423-3460.
218. A. Borissov, Y. K. Maurya, L. Moshniaha, W. S. Wong, M. Zyla-Karwowska and M. Stepien, *Chem. Rev.*, 2022, **122**, 565-788.
219. W. Zhang, K. Shi, J. Lai, Y. Zhou, X. Wei, Q. Che, J. Wei, L. Wang and G. Yu, *Adv. Mater.*, 2023, **35**, 2300145.
220. L. Zou, X. Y. Wang, X. X. Zhang, Y. Z. Dai, Y. D. Wu, J. Y. Wang and J. Pei, *Chem. Commun.*, 2015, **51**, 12585-12588.
221. Z. H. Wu, Z. T. Huang, R. X. Guo, C. L. Sun, L. C. Chen, B. Sun, Z. F. Shi, X. Shao, H. Li and H. L. Zhang, *Angew. Chem. Int. Ed.* 2017, **56**, 13031-13035.
222. Y. Min, C. Dou, D. Liu, H. Dong and J. Liu, *J. Am. Chem. Soc.*, 2019, **141**, 17015-17021.
223. Y. Min, C. Dou, H. Tian, Y. Geng, J. Liu and L. Wang, *Angew. Chem. Int. Ed.*, 2018, **57**, 2000-2004.
224. X. Feng, F. Iwanaga, J. Y. Hu, H. Tomiyasu, M. Nakano, C. Redshaw, M. R. Elsegood and T. Yamato, *Org. Lett.*, 2013, **15**, 3594-3597.
225. M. Armand and J. M. Tarascon, *Nature*, 2008, **451**, 652-657.
226. P. Poizot, J. Gaubicher, S. Renault, L. Dubois, Y. Liang and Y. Yao, *Chem. Rev.*, 2020, **120**, 6490-6557.
227. T. B. Schon, B. T. McAllister, P. F. Li and D. S. Seferos, *Chem. Soc. Rev.*, 2016, **45**, 6345-6404.
228. G. Zhang, F. R. Lin, F. Qi, T. Heumuller, A. Distler, H. J. Egelhaaf, N. Li, P. C. Y. Chow, C. J. Brabec, A. K. Jen and H. L. Yip, *Chem. Rev.*, 2022, **122**, 14180-14274.
229. M. A. Lebedeva, T. W. Chamberlain and A. N. Khlobystov, *Chem. Rev.*, 2015, **115**, 11301-11351.
230. G. Zhang, J. Zhao, P. C. Y. Chow, K. Jiang, J. Zhang, Z. Zhu, J. Zhang, F. Huang and H. Yan, *Chem. Rev.*, 2018, **118**, 3447-3507.
231. Y. Li, X. Huang, K. Ding, H. K. M. Sheriff, Jr., L. Ye, H. Liu, C. Z. Li, H. Ade and S. R. Forrest, *Nat. Commun.*, 2021, **12**, 5419.
232. D. Luo, L. Li, Y. Shi, J. Zhang, K. Wang, X. Guo and A. K. K. Kyaw, *J. Mater. Chem. A*, 2021, **9**, 14948-14957.
233. A. W. Hains, Z. Liang, M. A. Woodhouse and B. A. Gregg, *Chem. Rev.*, 2010, **110**, 6689-6735.
234. D. Zhao, Q. Wu, Z. Cai, T. Zheng, W. Chen, J. Lu and L. Yu, *Chem. Mater.*, 2016, **28**, 1139-1146.
235. J. Liu, J. Li, X. Liu, F. Li and G. Tu, *ACS Appl. Mater. Interfaces*, 2018, **10**, 2649-2657.
236. W. Li, Z. Liu, R. Yang, Q. Guan, W. Jiang, A. Islam, T. Lei, L. Hong, R. Peng and Z. Ge, *ACS Appl. Mater. Interfaces*, 2017, **9**, 27083-27089.
237. W. J. Sun, Y. T. Wang, Y. Zhang, B. Sun, Z. Q. Zhang, M. J. Xiao, X. Y. Li, Y. Huo, J. Xin, Q. Zhu, W. Ma and H. L. Zhang, *Angew. Chem. Int. Ed.*, 2022, **61**, e202208383.
238. R. T. Ross and A. J. Nozik, *J. Appl. Phys.*, 1982, **53**, 3813-3818.
239. Z. Huang and M. C. Beard, *J. Am. Chem. Soc.*, 2022, **144**, 15855-15861.
240. W. Shockley and H. J. Queisser, *J. Appl. Phys.*, 1961, **32**, 510-519.
241. J. P. Mora-Fuentes, I. Papadopoulos, D. Thiel, R. Alvarez-Boto, D. Cortizo-Lacalle, T. Clark, M. Melle-Franco, D. M. Guldi and A. Mateo-Alonso, *Angew. Chem. Int. Ed.*, 2020, **59**, 1113-1117.
242. T. Nokami, T. Matsuo, Y. Inatomi, N. Hojo, T. Tsukagoshi, H. Yoshizawa, A. Shimizu, H. Kuramoto, K. Komae, H. Tsuyama and J. Yoshida, *J. Am. Chem. Soc.*, 2012, **134**, 19694-19700.
243. J. Hu, D. Zhang and F. W. Harris, *J. Org. Chem.*, 2005, **70**, 707-708.
244. Y. Liang, Y. Jing, S. Gheytani, K. Y. Lee, P. Liu, A. Facchetti and Y. Yao, *Nat. Mater.*, 2017, **16**, 841-848.
245. H. Dong, O. Tutusaus, Y. Liang, Y. Zhang, Z. Lebens-Higgins, W. Yang, R. Mohtadi and Y. Yao, *Nature Energy*, 2020, **5**, 1043-1050.
246. H. Cui, P. Hu, Y. Zhang, W. Huang and A. Li, *ChemElectroChem*, 2020, **8**, 352-359.
247. K. Li, S. Xu, D. Han, Z. Si and H. G. Wang, *Chem.Asian J.*, 2021, **16**, 1973-1978.
248. X.-H. Chen, H. Lu, Z. Wu, H. Wang, S. Zhang, S. Mei, G. Long, Q. Zhang and C.-J. Yao, *J. Mater. Chem. A*, 2023, **11**, 77-83.
249. B. T. McAllister, E. Grignon, T. B. Schon, S. Y. An, C.-H. Yim, Y. Abu-Lebdeh and D. S. Seferos, *ACS Appl. Energy Mater.*, 2021, **4**, 6659-6666.